JSCSEN 91(4)331-439(2026)

ISSN 1820-7421(Online)

Journal of the Serbian Chemical Society

Electronic version

VOLUME 91

No 4

BELGRADE 2026

Available on line at

www.shd.org.rs/JSCS/

The full search of JSCS is available through

DOAJ DIRECTORY OF OPEN ACCESS JOURNALS

www.doaj.org

The **Journal of the Serbian Chemical Society** (formerly Glasnik Hemijskog društva Beograd), one volume (12 issues) per year, publishes articles from the fields of chemistry. The **Journal** is financially supported by the **Ministry of Science, Technological Development and Innovation of the Republic of Serbia.**
Articles published in the **Journal** are indexed in **Clarivate Analytics products: Science Citation Index-Expanded™** – accessed *via* **Web of Science®** and **Journal Citation Reports®**.
Impact Factor announced for the year 2024: **0.700; 5-year Impact Factor**: **0.900**.
Articles appearing in the **Journal** are also abstracted by: **Scopus, Chemical Abstracts Plus (CAplus℠), Directory of Open Access Journals, Referativnii Zhurnal (VINITI), RSC Analytical Abstracts, EuroPub, Pro Quest** and **Asian Digital Library.**

Publisher:	**Serbian Chemical Society**, Karnegijeva 4/III, P. O. Box 36, 1120 Belgrade 35, Serbia tel./fax: +381–11–3370–467, E-mails: **Society** – shd@shd.org.rs; **Journal** – jscs@shd.org.rs Home Pages: **Society** – http://www.shd.org.rs/, **Journal** – http://www.shd.org.rs/JSCS/
Internet Service:	Contents, Abstracts and full papers (from Vol. 64, No. 1, 1999) are available in the electronic form at the Web Site of the **Journal** (http://www.shd.org.rs/JSCS/).
Former Editors:	**Nikola A. Pušin** (1930–1947), **Aleksandar M. Leko** (1948–1954), **Panta S. Tutundžić** (1955**–**1961), **Miloš K. Mladenović** (1962–1964), **Đorđe M. Dimitrijević** (1965–1969), **Aleksandar R. Despić** (1969–1975), **Slobodan V. Ribnikar** (1975–1985), **Dragutin M. Dražić** (1986–2006), **Branislav Ž. Nikolić** (2006-2026).
Editor-in-Chief:	DUŠAN **SLADIĆ**, Faculty of Chemistry, University of Belgrade
Deputy Editors:	MARIO **ZLATOVIĆ**, Faculty of Chemistry, University of Belgrade, VLADIMIR **PANIĆ**, Institute of Chemistry, Technology and Metallurgy, University of Belgrade
Sub editors:	
,	
Organic Chemistry	DEJAN **OPSENICA**, Institute of Chemistry, Technology and Metallurgy, University of Belgrade JÁNOS **CSANÁDI**, Faculty of Science, University of Novi Sad
Biochemistry and Biotechnology	OLGICA **NEDIĆ**, INEP – Institute for the Application of Nuclear Energy, University of Belgrade
Inorganic Chemistry	BILJANA **GLIŠIĆ**, Faculty of Science, University of Kragujevac
Theoretical Chemistry	MATIJA **ZLATAR**, Institute of Chemistry, Technology and Metallurgy, University of Belgrade MILOŠ **MILIČIĆ**, Faculty of Chemistry, University of Belgrade
Physical Chemistry	LJILJANA **DAMJANOVIĆ-VASILIĆ**, Faculty of Physical Chemistry, University of Belgrade
Electrochemistry	SNEŽANA **GOJKOVIĆ**, Faculty of Technology and Metallurgy, University of Belgrade
Analytical Chemistry	RADA **BAOŠIĆ**, Faculty of Chemistry, University of Belgrade
Polymers	BRANKO **DUNJIĆ**, Faculty of Technology and Metallurgy, University of Belgrade
Thermodynamics	MIRJANA **KIJEVČANIN**, Faculty of Technology and Metallurgy, University of Belgrade
Chemical Engineering	TATJANA **KALUĐEROVIĆ RADOIČIĆ**, Faculty of Technology and Metallurgy, University of Belgrade
Materials	RADA **PETROVIĆ**, Faculty of Technology and Metallurgy, University of Belgrade
Metallic Materials and Metallurgy	ANA **KOSTOV**, Mining and Metallurgy Institute Bor, University of Belgrade
Environmental and Geochemistry	VESNA **ANTIĆ**, Faculty of Agriculture, University of Belgrade
History of and Education in Chemistry	DRAGICA **TRIVIĆ**, Faculty of Chemistry, University of Belgrade
English Language Editors:	VLATKA **VAJS**, Serbian Chemical Society MIROSLAV **PAVLOVIĆ**, Institute of Chemistry, Technology and Metallurgy, University of Belgrade
Journal Manager & Web Master:	MARIO **ZLATOVIĆ**, Faculty of Chemistry, University of Belgrade
Office:	VERA **ĆUŠIĆ**, Serbian Chemical Society

Editorial Board
From abroad: **R. Adžić**, Brookhaven National Laboratory (USA); **A. Casini**, University of Groningen (The Netherlands); **G. Cobb**, Baylor University (USA); **D. Douglas**, University of British Columbia (Canada); **G. Inzelt**, Etvos Lorand University (Hungary); **J. Kenny**, University of Perugia (Italy); **Ya. I. Korenman**, Voronezh Academy of Technology (Russian Federation); **M. D. Lechner**, University of Osnabrueck (Germany); **S. Macura**, Mayo Clinic (USA); **M. Spiteller**, INFU, Technical University Dortmund (Germany); **M. Stratakis**, University of Crete (Grecce); **M. Swart**, University de Girona (Cataluna, Spain); **G. Vunjak-Novaković**, Columbia University (USA); **P. Worsfold**, University of Plymouth (UK); **J. Zagal**, Universidad de Santiago de Chile (Chile).
From Serbia: **B. Abramović**, **V. Antić**, **R. Baošić**, **V. Beškoski**, **J. Csanadi**, **Lj. Damjanović-Vasilić**, **A. Dekanski**, **V. Dondur**, **B. Dunjić**, **M. Đuran, B. Glišić, S. Gojković**, **I. Gutman**, **B. Jovančićević**, **I. Juranić**, **T. Kaluđerović Radoičić**, **L. Katsikas**, **M. Kijevčanin**, **A. Kostov**, **V. Leovac**, **S. Milonjić**, **V.B. Mišković-Stanković**, **O. Nedić**, **D. Opsenica**, **V. Panić**, **M. Pavlović**, **M. Petkovska**, **R. Petrović**, **I. Popović**, **B. Radak**, **S. Ražić**, **D. Sladić**, **S. Sovilj**, **S. Šerbanović**, **B. Šolaja**, **Ž. Tešić**, **D. Trivić**, **V. Vajs, M. Zlatović**.

Subscription: The annual subscription rate is **150.00 €** including postage (surface mail) and handling. For Society members from abroad rate is **50.00 €**. For the proforma invoice with the instruction for bank payment contact the Society Office (E-mail: shd@shd.org.rs) or see JSCS Web Site: http://www.shd.org.rs/JSCS/, option Subscription.
Godišnja pretplata: Za članove SHD: **2.500,00 RSD**, za penzionere i studente: **1000,00 RSD**, a za ostale: **3.500,00 RSD**:za organizacije i ustanove: **16.000,00 RSD**. Uplate se vrše na tekući račun Društva: **205-13815-62**, poziv na broj **320**, sa naznakom "pretplata za JSCS".

Nota: Radovi čiji su svi autori članovi SHD prioritetno se publikuju.
Odlukom Odbora za hemiju Republičkog fonda za nauku Srbije, br. 66788/1 od 22.11.1990. godine, koja je kasnije potvrđena odlukom Saveta Fonda, časopis je uvršten u kategoriju međunarodnih časopisa (**M-23**). Takođe, aktom Ministarstva za nauku i tehnologiju Republike Srbije, 413-00-247/2000-01 od 15.06.2000. godine, ovaj časopis je proglašen za publikaciju od posebnog interesa za nauku. **Impact Factor** časopisa objavljen za 2024. godinu je **0,700**, a petogodišnji **Impact Factor 0,900**.

Journal of the Serbian Chemical Society
JSCS-info@shd.org.rs • www.shd.org.rs/JSCS

J. Serb. Chem. Soc. Vol. 91, No. 4 (2026)

CONTENTS*

Published by the Serbian Chemical Society
Karnegijeva 4/III, P.O. Box 36, 11120 Belgrade, Serbia
Printed by the Faculty of Technology and Metallurgy
Karnegijeva 4, P.O. Box 35-03, 11120 Belgrade, Serbia

* For colored figures in this issue please see electronic version at the Journal Home Page: http://www.shd.org.rs/JSCS/

Journal of the Serbian Chemical Society
JSCS@tmf.bg.ac.rs • www.shd.org.rs/JSCS
J. Serb. Chem. Soc. 91 (4) 331–352 (2026)
JSCS–5495
Original scientific paper
Published 6 May, 2026

Application of Floquet theory and improvement of electron current flow control in a 1D Fe–Cu molecular chain

VIOLETA N. NIKOLIĆ[1]* and JOSE F. M. L. MARIANO[2,3]

[1]Department of Theoretical Physics and Condensed Matter Physics (020) Vinča Institute of Nuclear Sciences, National Institute of the Republic of Serbia, University of Belgrade, P.O. Box 522, 11001 Belgrade, Serbia, [2]FCT, Campus de Gambelas, University of Algarve, Faro, 8005-139, Portugal and [3]Center of Physics and Engineering of Advanced Materials (CeFEMA), IST, University of Lisbon, Av. Roviscno Pais, Roviscno Pais, Lisbon, 1096-001, Portugal

(Received 22 August 2025, revised 5 February, accepted 18 March 2026)

Abstract: In this study is investigated the application of Floquet theory to a one-dimensional (1D) Fe–Cu molecular chain under periodic driving. It was demonstrated that orbital hybridization induces resonant behavior in the low-frequency regime, highlighting the potential of this system for energy-efficient and robust device applications. For the first time, a Floquet electronic friction framework – incorporating the influence of periodic driving on electron transfer – is applied to a 1D Fe–Cu molecular chain in the presence of strong light–matter interaction (LMI). Electron transport properties are analyzed, revealing the existence of an optimal driving frequency that maximizes the electric current. Two mechanisms for enhancing charge transport in the strong LMI regime are identified: a) hybridization-induced resonances and b) photon-assisted transport processes. In this work is combined Floquet band structure analysis with open-system transport modeling in a 1D Fe–Cu motif, revealing the impact of hybridization and periodic driving, on the enhancement of electron transport *via* photon-assisted resonances – an approach that bridges quasi-energy spectra and dissipative transport in a single theoretical framework. These findings provide new insights into driven low-dimensional transition-metal systems and may support the development of Fe–Cu-based materials for electrochemical applications.

Keywords: hybridization; photon-assisted processes; heterogeneous catalysis.

INTRODUCTION

Nowadays, control of the electron transport attracts attention of the scientific community. One of the aspects of this control, is the impact of the periodic driving on the electron transport, which is nowadays thoroughly investigated in literature.[1–4] Theoretical approach, often applied to study electron transport, is Floquet

* Corresponding author. E-mail: violeta@vin.bg.ac.rs
https://doi.org/10.2298/JSC250822014N

theory.[5] Floquet theory represents a mathematical framework of importance in theoretical electrochemistry, because it can facilitate current experimental electrochemical research. One of the fields of electrochemistry, in which Floquet theory is used, is heterogeneous catalysis,[6–8] where the application of Floquet theory allows deeper insight into the coupled electron-nuclear dynamics.[9] Moreover, investigation of the electron transfer under different applied bias can contribute to an improved understanding of the catalysis processes, and different, related areas of electrochemistry.[10–13] In 2024, Chen *et al*. considered application of the Floquet electronic friction model in order to get deeper insight in the molecular dynamics of near metal surfaces in the presence of periodic driving and confirmed that Floquet driving affects electron transfer.[14]

On the other hand, a class of promising, but still insufficiently investigated, materials that could be used to improve electrochemical catalysis are materials containing Fe–Cu molecular chains. A literature review has shown that exploring the unique properties of Fe and Cu interactions, presented in the catalysts containing these species, could facilitate the development of more selective and efficient catalysis, which could be used for applications, related to the sustainable energy conversion processes.[15,16] To model materials, containing Fe–Cu species, researchers applied different theoretical approaches, such as: DFT theory,[17] molecular dynamics[18] and Monte Carlo simulations,[19] *ab initio* calculations,[20] *etc*.

It is important to note that, to our knowledge, Floquet quasi-energy band structure analysis and open-system transport modeling within an electronic friction framework, has not been previously established for low-dimensional Fe–Cu systems, although their application on a given system could provide deeper insight in its properties, which is of significance for its application in electrochemistry. While Floquet theory has been widely applied to periodically driven systems, its integration with open-system transport modeling at the level of band-structure-resolved analysis remains relatively unexplored. This is also of importance from the point of view of quantum research, since, until now, bridging Floquet band structure analysis with dissipative transport modeling remains a relatively underdeveloped direction in driven quantum materials research.

Accordingly, in order to gain deeper insight into improved control of electron current in materials containing Fe–Cu molecular chains, this study investigated the possibility of improving electron transport in a 1D Fe–Cu molecular chain by applying Floquet theory. For the first time, Floquet theory was used as a theoretical approach to examine this structure. Recall that the application of Floquet theory to a 1D Fe–Cu molecular chain and a 1D Fe–Cu molecular chain results in a different Floquet band structure, due to the possible presence of asymmetry in the system, which could arise if Fe is present on the Cu substrate.

In the first part of the study, the Floquet band structure of the 1D Fe–Cu structure is illustrated, with a representation of the composition of Floquet band 3.

The influence of the orbital hybridization effect on the increase in electric current in a 1D Fe–Cu molecular chain, was considered. The effect of hybridization strength on the 1D Fe–Cu molecular chain simplified band structure, is commented, with the aim of controlling the resonance frequency shift by affecting the energy gap in the investigated hybridized 1D Fe–Cu molecular chain Floquet band structure.

On the other hand, the increase in electric current can be considered by investigating the behavior of electronic states, interacting with photon modes, during the strong LMI regime, which is discussed in more detail in the second part of the study. The dependence of electric current dependence on driving frequency for a 1D Fe–Cu molecular chain is presented, by varying the the value of the chemical potential. Deeper insight into the possibility of improving the control of electric current flow in a 1D Fe–Cu molecular chain, under driving impact, in the strong LMI regime, is of importance for the practical applications of materials containing Fe–Cu chains, in the field of electrochemistry.

MODEL AND THEORETICAL METHODS

In this work, two complementary theoretical models are employed and combined, with the aim to investigate light-driven electron transport in a 1D Fe–Cu molecular system. Model I describes a periodically driven tight-binding Fe–Cu chain, and it is used to analyze Floquet band formation and hybridization effects. Model II describes a driven open two-level junction coupled to electronic leads and vibrational baths, and it is used to compute bias-dependent current under nonequilibrium conditions.

The first model provides insight into resonance formation in the Floquet quasi-energy spectrum, while the second translates this resonance structure into transport properties under applied bias. Below will be more described each of models, in order to get deeper insight in the postulation of the theoretical model discussed in this study.

Model I, denoting to the periodically driven tight-binding Fe–Cu chain, is relied on the static tight-binding Hamiltonian, constructed by considering a 1D periodic chain, composed of alternating Fe and Cu sites, within a single unit cell.

It is important to note that we begin calculations from a tight-binding Hamiltonian formulated in a localized orbital basis, where on-site energies describe Fe and Cu atomic orbitals and hopping terms, represent nearest-neighbor coupling and hybridization. This Hamiltonian is initially written in real space. For the periodic one-dimensional Fe–Cu chain considered in the band-structure analysis, translational symmetry allows the application of Bloch's theorem. By performing a Fourier transform to momentum space, the real-space tight-binding Hamiltonian is recast into a k-dependent Bloch Hamiltonian $H(k)$. The Bloch Hamiltonian is therefore not a different physical model, but rather the momentum–space representation of the same tight-binding Hamiltonian under periodic boundary conditions. This representation enables calculation of the band structure and, subsequently, its Floquet extension under time-periodic driving.

Accordingly, in the frame of Model I, the system is described within a nearest-neighbor tight-binding (TB) approximation. In momentum space, the Bloch Hamiltonian is given by Eq. (1):

$$H(k) = \begin{pmatrix} \varepsilon_{\mathrm{Fe}} & t + Ve^{-ika} \\ t + Ve^{-ika} & \varepsilon_{\mathrm{Cu}} \end{pmatrix} \quad (1)$$

where $\varepsilon_{\mathrm{Fe}}$ and $\varepsilon_{\mathrm{Cu}}$ represent on-site energies, t is the hopping amplitude, V represents the Fe–Cu hybridization strength, a is the lattice constant and k is the crystal momentum. Bonding and antibonding bands are obtained by diagonalization of given Hamiltonian. Note that, the tight-binding Hamiltonian is written with off-diagonal hopping terms as $t + Ve^{-ika}$. The specific order reflects the chosen basis and Fourier convention; equivalent forms can be obtained by alternative conventions, but here is used a uniform notation for clarity.

Since the system is subjected to an external periodic field (representing an ultrafast laser), to describe time-variations of the system, the time-dependent Hamiltonian is introduced:

$$H(k,t) = H(k) + A\theta \cos \omega t \quad (2)$$

where is A – the driving amplitude, ω – the driving frequency and θ – the operator of coupling the two orbitals (taken as an inter-site coupling term).

Further, Floquet construction which will be performed, is explained below. In this study was possible to apply Floquet theory on the investigated system, since the Hamiltonian is periodic in time (H(t + T) = H(t), where $T = 2\pi/\omega$).

The Floquet Hamiltonian is defined as:

$$H_{\mathrm{F}} = H(k,t) - i\hbar\delta_{mn} \quad (3)$$

In practice, the Hamiltonian is expanded in a truncated harmonic basis $e^{in\omega t}$, while harmonics 0, ±1 are retained. This yields a finite-dimensional block matrix representation:

$$(H_{\mathrm{F}})_{mn} = H_{m-n}(k) + n\hbar\delta_{mn} \quad (4)$$

Diagonalization of this enlarged matrix yields Floquet quasi-energies and harmonic weights. The orbital composition of selected Floquet bands is obtained from the eigenvector components. The sign convention in the last term of Eq. (4) arises from the definition of the Floquet harmonics, where the phase factor (e^{-ika}) corresponds to hopping from Fe to Cu sites in the chosen unit cell; this convention ensures consistency of the Hamiltonian matrix elements across all harmonics. For clarity, only the first three harmonics (m = 0, ±1) are retained in the discussion (see Numerical Methods for the general truncation to $m = -N\_F,...,N\_F$, where the results are shown for N_F = 3).

Numerical procedure, performed in order to apply Model I on a considered system, was based on the construction of $H(k)$, for each value of k. Afterwards, it was builded truncated Floquet matrix, which diagonalization was performed numerically, and quasi-energies and orbital weights were extracted, for each vlaue of k. All calculations were performed, using standard matrix diagonalization routines in Matlab (R2022b).[21]

Model II was applied to describe driven two-level molecular junctions. In order to discuss electron transport under applied bias, an open quantum system, representing an effective Fe–Cu dimer, coupled to electronic reservoirs, was considered. The total Hamiltonian (in the case of this model) is:

$$H(t) = H_{\mathrm{mol}}t + H_{\mathrm{leads}} + H_{m\text{ol-leads}} + H_{\mathrm{vib}} \quad (5)$$

Below are explained terms, of which is consisted the total Hamiltonian. The driven molecular Hamiltonian is represented as:

$$H_{\text{mol}}(t) = \begin{pmatrix} \varepsilon_{\text{Fe}} & \Delta + A\cos\omega t \\ \Delta + A\cos\omega t & \varepsilon_{\text{Cu}} \end{pmatrix} \tag{6}$$

where Δ is the static inter-site coupling,and $A\cos\omega t$ represents laser-induced modulation.

Next, the leads (electronic reservoirs) are modelled as:

$$H_{\text{leads}} = \sum \varepsilon_{k,\alpha} C_{k\alpha}^{\dagger} C_{k\alpha} \tag{7}$$

where index k depicts to the quantum number for a state in the lead, index α depicts to the left or right lead, $\varepsilon_{k\alpha}$ is energy of the single-particle state k in lead α, $c_{k\alpha}^{\dagger}$ is Fermionic creation operator for an electron in state k of lead α, and $c_{k\alpha}$ – Fermionic annihilation operator for an electron in state k of lead α. These Hamiltonian models the leads as noninteracting electron reservoirs. Each lead has a continuum of states with energies $\varepsilon_{k\alpha}$. Electrons in these leads can tunnel to the molecule *via* the coupling Hamiltonian.

Considering chemical potentials, μ_{L} and μ_{R}, the applied bias is defined as:

$$V_{\text{bias}} = \mu_{\text{L}} - \mu_{\text{R}} \tag{8}$$

Molecule-lead coupling is illustrated as:

$$H_{\text{mol-leads}} = \sum (t_{\alpha} C_{k\alpha}^{\dagger} d_{\alpha} + h.c.) \tag{9}$$

where is t_{α} – molecule–lead hopping amplitude (coupling strength) for lead α (it determines impact of electrons tunneling between molecule and lead), d_{α} – annihilation operator for the molecular orbital connected to lead α (d_{L} couples to left, d_{R} to right), $c_{k\alpha}^{\dagger}$ – creation operator for electron in lead state $k\alpha$, and *h.c.* is Hermitian conjugate (representing addition of the term $t_{\alpha}^{\%*} d_{\alpha}^{\dagger} c_{k\alpha}$). This term allows electrons to hop between the molecule and the leads. The rate of tunneling depends on $|t_{\alpha}|^2$ and the lead density of states.

Finally, vibrational coupling is incorporated in the model, by considering nuclear vibrational modes, modelled as harmonic oscillators, coupled linearly to electronic populations:

$$H_{\text{vib}} = \sum \left(\frac{p_i^2}{2M_i} + \frac{1}{2} M_i \Omega_i^2 x_i^2 \right) \tag{10}$$

where is p_i – momentum operator of vibrational mode i, x_i – position perator of vibrational mode i, M_i – effective mass of vibrational mode i and Ω_i – angular frequency of vibrational mode i. In other words, each molecular vibration is modeled as a harmonic oscillator. Vibrational modes can couple to electronic populations and influence tunneling rates (electron–phonon coupling).

In order to postulate Master equation, the Born, Markov, secular and wide-band approximations were applied, resulting in the reduced desity matrix, $\rho(t)$:

$$\frac{\partial \rho}{\partial t} = \frac{-i}{\hbar} [H_{\text{mol}}(t), \rho] + L_{\text{leads}}[\rho] + L_{\text{vib}}[\rho] \tag{11}$$

where L_{leads} described tunneling-induced dissipation (electron tunneling under the wide-band approximation) and L_{vib} illustrated vibrational relaxation, with application of secular approximation, and assuming that leads are in thermal equilibrium with Fermi functions:

$$F_{\alpha}(E) = \frac{1}{1 + \mathrm{e}^{(E-\mu_{\alpha})/k_{\text{B}}T}} .$$

The master equation in the Supplementary material to this paper (Eq. (S1)) shows the same evolution in an expanded form, explicitly separating the dissipative contributions from the leads

and vibrational environment. To define current from lead α (I_α, describing measure of steady--state electron flow from lead α, into the molecule), computations are performed, based on Eq. (12):

$$I_\alpha = Tr\left[J_\alpha \rho_{ss}\right] \tag{12}$$

where J_α – the current superoperator (derived from the lead dissipator), associated with electron transfer through lead α; J_α represents current superoperator, corresponding to electron tunneling through lead α (this magnitude is formally derived from $H_{\text{mol-lead}}$), ρ_{ss} is steady-state density matrix of the molecule (obtained, after solving the master equation) and represents race over molecular degrees of freedom. Eq. (12) calculates the expectation value of the current in the steady state. Electrons flow from leads into the molecule (or vice versa) depending on chemical potential difference (bias). For frequency-dependent plots, the current is normalized with respect to its maximal value for fixed bias. Accordingly, Eq. (12) shows the current in normalized units (I/I_0), and does not include the elementary charge, e.

In the case of Model II, numerical procedure for its implementation in a postulated theoretical model, was as follows. First are constructed finite Hamiltonian matrices, then Floquet diagonalization is performed. Afterwards, it was considered time-evolution of master equation, and steady-state extraction, after which is performed evaluation of expectation values.

No *ab initio* or quantum-chemical electronic structure calculations were performed. All simulations rely on model Hamiltonians and standard linear algebra routines.

All parameter values used in the simulations are explicitly listed in Table I.

TABLE I. Parameters used in all numerical simulations of the 1D Fe–Cu chain, including tight--binding, hybridization, vibrational, lead coupling and external driving values. The table provides typical ranges and units for reproducibility. All values are either representative or varied systematically in the simulations, as detailed in Matlab scripts of the Supplementary material

Parameter	Symbol	Typical value[ref.]	Description of the parameter
Fe–Cu orbital hybridization	V	0.5–3 eV[22]	Static orbital overlap between Fe and Cu
Hopping amplitude	t	1 eV[23]	Tight-binding nearest-neigbor hopping
On-site energies	ε_{Fe}, ε_{Cu}	0.1 eV[24]	Site energies of Fe and Cu orbitals
Lead tunneling	t_L, t_R	0.1–0.5 eV[25]	Coupling to left/right leads
Vibrational frequency	Ω_i	0.1–0.5 eV[26]	Harmonic mode frequencies
Vibrational mass	M_i	1 amu[27]	Effective mode mass
Driving amplitude	A	0–3 eV[28]	Floquet driving strength
Driving frequency	ω	1–3 eV[28]	Photon energy of external field
Temperature	T	300 K[25]	Leads thermal equilibrium

To understand relationship between these two models (Models I and II), applied for postulation of a theoretical model considered in this study, recall that Model I provided band--structure level understanding of orbital hybridization, Floquet sideband formation and resonance conditions, while Model II captured nonequilibrium transport, bias dependence and dissipative dynamics. Accordingly, Model II may be interpreted as an effective transport reduction of the dominant hybridized Floquet states, identified in Model I.

The theoretical models described above were implemented numerically in Matlab. For the Floquet band analysis, the tight-binding Hamiltonian of the 1D Fe–Cu chain was constructed

and expanded in a truncated Floquet harmonic basis; the resulting Floquet matrix was diagonalized using standard eigenvalue routines to obtain quasi-energy spectra and harmonic weights. For the transport calculations, the Master equation for the reduced density matrix was propagated in time using standard linear algebra solvers until a steady state was reached. The current through each lead was then evaluated as the trace of the current superoperator with the steady-state density matrix. These procedures rely on numerical matrix construction, diagonalization and time evolution, and do not involve *ab initio* quantum chemistry methods. All scripts and parameter values used to generate the figures are available in the Matlab scripts, archived in Zenodo.

Numerical methods

All numerical calculations were performed using custom scripts implemented in Matlab. The computational procedure is consisted of two independent parts corresponding to Floquet band analysis of the periodic Fe–Cu chain, and to open-system transport calculations for the driven junction model.

Floquet band structure calculations for the periodic 1D Fe–Cu chain relied on the construction of the tight-binding Hamiltonian in momentum space, Eq. (1).

Under periodic driving with field amplitude A and frequency ω, the time-dependent Hamiltonian is given as Eq. (2), while the Hamiltonian is expanded in a harmonic basis, Eq. (3).

The time-periodic problem is mapped onto a static eigenvalue problem in extended Floquet space by truncating the harmonic index to $m = -N_F,\ldots,N_F$. For all figures in this work, we set N_F to 3, corresponding to the retention of harmonics 0, ±1. Convergence with respect to N_F was verified numerically.

The resulting block matrix is diagonalized using Matlab's standard dense eigenvalue solver (eig) to obtain quasi-energy spectra and Floquet eigenstates. Band structures are generated by sweeping k across the first Brillouin zone.

Master equation transport calculations are relied on the total Hamiltonian, postulated for the driven molecular junction:

$$H(t) = H_{mol} + H_{leads} + H_{mol-leads} + H_{vib} + H_{drive}(t) \tag{13}$$

The reduced density matrix $\rho(t)$ evolves according to the Born–Markov master equation, Eq. (11). The density matrix is propagated in time using Matlab's ODE solvers, until a steady state ρ_{ss} is reached.

Further, the current from lead is computed, by Eq. (12). Bias voltage is introduced *via*:

$$\mu_L = \frac{+eV_{bias}}{2}, \mu_R = \frac{-eV_{bias}}{2} \tag{14}$$

Current–bias and current–frequency characteristics are obtained by parameter sweeps over bias voltage (V_{bias}), driving amplitude (A) and driving frequency (ω). The bias voltage is introduced *via* eq. (14), which enters the system Hamiltonian and thereby determines the terms appearing in eq. (8). Current–bias and current–frequency characteristics are obtained by parameter sweeps over V_{bias}, driving amplitude A and driving frequency ω.

Below are given numerical implementation details.

The numerical procedure is consisted of construction of finite-dimensional Hamiltonian matrices, Floquet matrix assembly with harmonic truncation, matrix diagonalization for quasi-energy spectra, construction of Liouvillian superoperators, time propagation of the density matrix and trace evaluation for steady-state current.

All calculations are relied on standard numerical linear algebra operations (matrix construction, diagonalization, ODE integration). No density functional theory (DFT), Hartree–Fock or correlated *ab initio* electronic-structure methods were employed. Parameter values used in all simulations are listed in Table I. All scripts used to generate the figures are available in a repository provided for peer review.

RESULTS AND DISCUSSION

Impact of the orbital hybridization effect, on the electric flow in 1D Fe–Cu molecular chain

To perform visualization of the Floquet band structure of the 1D Fe–Cu molecular chain, a corresponding simplified theoretical model was postulated. The model is relied on the tight-binding (TB) model,[29] which has been applied to describe the irradiation of a Fe–Cu unit cell, by an ultrafast intense laser. The postulated model described the interaction between light and the Fe–Cu chain, resulting in the appearance of photons. The represented visual illustration enabled further mathematical tracking of the impact of the produced photon on the original band. In this manner, a deeper insight into the electronic landscape of the Fe–Cu molecular chain is provided, in which the second part of the study will provide a mathematical description of the electron transfer (modeled *via* electron tunneling), occurred through the chain.

Let us recall that the TB model is often applied to describe the electronic structure of a given material. In the case of our model, relied on the TB model, a uniform 1D molecular chain was considered, in which electrons are localized, but could tunnel between neighboring chemical species in the considered molecular chain. In order to prepare the appropriate Matlab code, it was necessary to propose an appropriate Hamiltonian to describe a uniform 1D molecular chain. The proposed simplified Hamiltonian consisted of two terms: the first term describes the energy of the localized electron (*i.e*., the on-site energy) and the second term represents a hopping term, which describes the amplitude of the probability of the electron tunneling to a neighboring site. Consideration of Bloch's theorem enabled the preparation of Matlab code for solving the eigenvalue problem[30] in order to obtain two energy bonds. In the visual illustration, these bonds are represented as bonding and antibonding bonds, represented by the same color (Fig. 1a). Further, the Matlab code is modified in order to illustrate the application of Floquet theory to our considered case, *i.e.*, to a periodically driven 1D Fe–Cu-like chain. The code was written by considering the periodical drive of the given system (the driving of the system induces a time dependence of the tight-binding Hamiltonian), and the quasi-energy spectrum was obtained by diagonalizing the enlarged Floquet Hamiltonian. As a result of applying the simplified Floquet theory to the case of a periodically driven 1D Fe–Cu molecular chain, Fig. 1b and c were obtained.

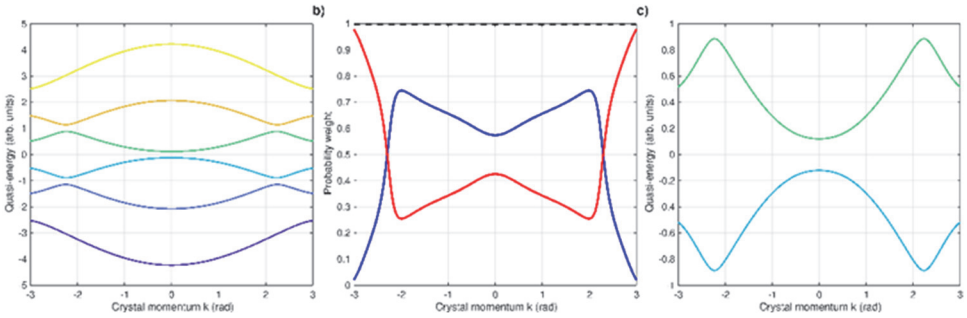

Fig. 1. Floquet band structure and orbital composition of a periodically driven 1D Fe–Cu molecular chain under strong driving ($t_1 = 0.6$, $\omega = 2$): a) Floquet quasi-energy band structure of the periodically driven 1D Fe–Cu chain, obtained from the k-dependent Bloch Hamiltonian under harmonic driving (the colors of the curves are used for visual clarity to distinguish different bands and do not correspond to a particular orbital, atom, or photon contribution); b) harmonic composition (Floquet mode weights) of the third quasi-energy band, illustrating the mixing of photon sectors induced by periodic driving (blue curve corresponded to Fe orbital weight, red curve to Cu orbital weight, and black dashed curve to the photon component); c) full quasi-energy spectrum showing the formation of Floquet replicas and hybridization-induced gap modification.

To understand Fig. 1, let us recall that the Floquet state represents a solution to the time-dependent Schrödinger equation, based on the considered Hamiltonian. In Fig. 1, Floquet states are represented as superpositions of harmonics, characterized by a resonance driving frequency. As a result, a photon appears in the system, the energy of which is specifically equal to the gap between the bonding and antibonding orbitals appears in the system. In other words, the resonance condition for the interaction between an external periodic field (laser), characterized by frequency ω, and the energy gap between the ground and excited state (bonding and antibonding state, respectively) of the system under consideration is estimated as: $\hbar\omega \approx \Delta E$, where $\hbar\omega$ represents photon replica bands. The driving of molecule in resonance results in the fact that a single Floquet state can be characterized by both, bonding and antibonding features. Consequently, this could lead to a new Floquet eigenstate, characterized by hybrid, mixed properties of both, the bonding and antibonding states.

Fig. 1a represents the evolution of averaged (quasi) bands, in a system with a 1D molecular chain, consisting of two sublattices (Fe and Cu), as a function of the crystal momentum k, in the presence of a time-periodic drive. It provides visualization of band hybridization, occurred due to interaction with a photon, in the vicinity of resonance. Since Fe and Cu are characterized by d-band structures and different electronegativities, the corresponding on-site energies differed significantly for these two atoms.

In a weak driving regime, Fig. 1a would provide a visualization of three harmonics (*i.e.*, the original band, the band shifted up by $+\hbar\omega$, and the band shifted

down by $-\hbar\omega$), composed of two orbitals (resulting in 6 lines). In the case of weak driving, observed three harmonics could be interpreted as three bands: the original band (characterized by the absence of shift), harmonic (band) shifted downward, and harmonic shifted upward. Since in a given case, it was considered strong driving of the investigated system, each colored line represented a distinct quasi-energy band, where is color of the line used for visual clarity. Under strong periodic driving, the quasi-energy bands arose from significant hybridization between different Floquet photon sectors, and each quasi-energy band becomes a mixture of many harmonics, so it is not possible to ascribe one color of the curve to the certain harmonic.

Fig. 1b represents a visualization of the orbital composition (probability weights of Fe and Cu orbitals) of a chosen Floquet band (in our case, Floquet band 3 was chosen), dependent on the crystal momentum, k. It represents the Floquet band composition across the Brillouin zone, describing electron tunneling between Fe and Cu species, along a 1D chain. Since the momentum k provides an information about the electron wavelength and the phase relations between orbitals, the orbital composition shows a complex dependence on k, characterized by hybridization effects.

Fe and Cu contributions illustrate the impact of the Floquet state on the mixing of the electronic and photonic character along the chain. The band eigenstate probability weights describe the extent to which the eigenstate at Floquet band 3 (for a given momentum, k) is localized on Fe or Cu orbitals (or mixed hybridization is represented). The total photon weight (illustrated by the black dashed curve, which represents the weight of Fe + the weight of Cu, summed over all Floquet harmonics) represents the photon composition. The blue line depicts to the total Fe orbital weight summed over all Floquet harmonics for band 3, for each value of k (and the red line shows the Cu orbital weight, respectively). The high Fe or Cu weight (at a given k), confirms that the electron, in a given Floquet state, shows an affinity to behave as a localized d-atom of Fe (or Cu, respectively). It should be noted that Floquet band 3 illustrates a mixed Fe–Cu character, depicting to the dominance of Fe or Cu orbitals (characteristic for given electronic states), at different moments. Strong LMI hybridization is confirmed by the fact that the photonic component shows relatively uniform behavior, while representing a significant part of the Fig. 1b.

It is worth noting that Floquet band 3 corresponds to a particular Floquet quasi-energy band that evolves from one of the hybridized bands.[31]

The composition of Floquet band 3 (Fe, Cu, and photon weights) reflects the extent to which the original Fe and Cu orbitals experienced hybridization, combined with the photon interaction induced by the drive. As a result of the hybrid nature of Floquet band 3, this band plays the most important role in light-induced transport, as electrons are characterized by the ability to absorb or emit photons,

which could be reflected in the spectrum, as a shift in energy and momentum. It is known that the Floquet band structure of a periodically driven 1D Fe–Cu molecular chain is significantly affected by the impact of strong LMI. As a result of the LMI impact, electron–photon quasi-particles are formed.[32] Consequently, the Floquet bands are strongly affected, as new gaps open at the photon resonances, leading to the appearance of new Floquet sidebands. In other words, the strong LMI regime induces a large photonic component in Floquet band 3, observed in Fig. 1b, which ensures band hybridization, which, further, results in high sensitivity to changes in the driving frequency of the investigated system (1D Fe–Cu molecular chain).

Fig. 1c shows the dependence of the Floquet quasi-energy bands on the crystal momentum k, which is discussed for Floquet band 3. It is shown chosen colored curves, corresponding to a quasi-energy band, with colors again used only to distinguish bands visually.

Fig. 1 is given with the aim of enabling visualization of the electronic structure of the 1D Fe–Cu chain, as it represents theoretical material used for mathematical monitoring of electron tunneling, described in more detail in the rest of the paper. It illustrated different aspects of the driven 1D Fe–Cu system: Fig. 1a shows the simplified band structure, Fig. 1b highlights the orbital/photon composition of a selected band and Fig. 1c presents the chosen Floquet spectrum.

After introducing the electronic structure of the 1D Fe–Cu chain, a theoretical model is proposed, enabling a discussion of the behavior of the current under the influence of the driving. The same tight-binding model is applied, with a modification of the Hamiltonian form. The influence of photon-assisted processes is also considered.

Appropriate Matlab code was written to illustrate the electric current oscillations with the driving frequency, Fig. 2a. The current behavior is assumed to be governed by resonant photon-assisted transitions, associated with the simplified Floquet band structure of the 1D Fe–Cu chain. It should be noted that the given model was postulated to examine the dependence of current oscillations on the driving frequency, without considering the hybridization effect, or the influence of chemical potential. Fig. 2 is intended to illustrate a simple representation of the probability of photon-assisted tunneling as a function of the driving frequency ω, in the form of the dependence of the normalized current on the driving frequency. In other words, it describes the effect of orbital hybridization on photon-assited tunneling and resonant transport in periodically driven molecular chains.

As expected, the current decreases rapidly with the driving frequency, indicating the absence of resonance condition. The maximum current value corresponds to optimal photon-assisted transport, when efficient absorption or emission of photons and transition between bands, occurs. The absence of resonance results in weaker photon-assisted transport. To illustrate the oscillations of the electric

current in its dependence on the driving frequency, caused by photon-assisted resonant transitions, with respect to the simplified Floquet band 3 composition, the model was modified to include the effect of orbital hybridization between Fe and Cu orbitals in Floquet band 3, and to consider its influence on the current behavior. The hybridization effect was investigated, because it is often observed in transition metal chains, such as Fe–Cu, where Fe 3d and Cu 3d orbitals interact. The corresponding model, as a premise, considered modifying the model Hamiltonian by introducing an additional hybridization term, V, characterizing mixing of Fe and Cu orbitals, resulting in two new hybridized bands (bonding and antibonding).

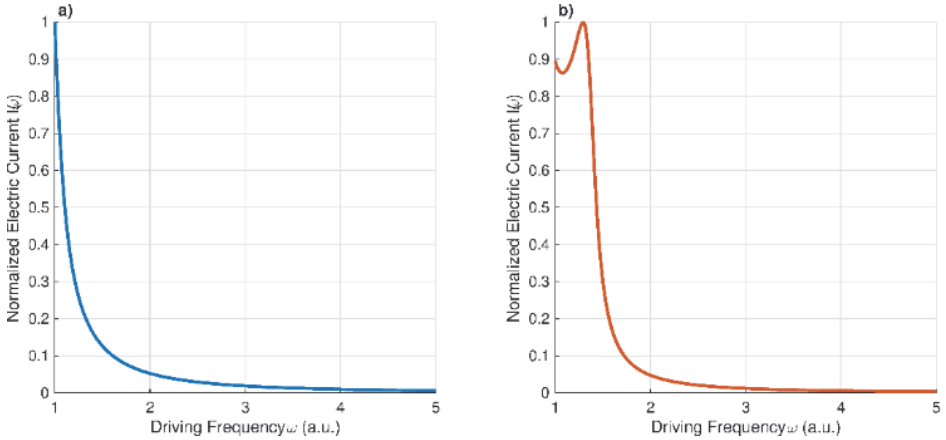

Fig. 2. Dependence of normalized current on driving frequency: a) normalized steady-state electric current as a function of driving frequency ω for the 1D Fe–Cu molecular chain in the absence of orbital hybridization ($V = 0$), showing no pronounced resonant enhancement; b) normalized steady-state current as a function of driving frequency in the presence of Fe–Cu orbital hybridization ($V \neq 0$), demonstrating resonance enhancement associated with hybridization-controlled quasi-energy gap formation.

The strength of the V is defined by the distance and chemical bonding between the Fe and Cu atoms, and this quantity affects the size of the band gap. Consequently, the two hybridized bands (appeared as a result of the Hamiltonian modification), are associated with the Floquet band structure of the investigated 1D Fe––Cu molecular chain. Let us recall that the Floquet band 3 is a band which is evolved from one of these hybridized bands under strong LMI. The proposed hybridization impacts the LMI strength, which increases the current. The discussed hybridization enables the opening of gaps, allowing for enhanced photon-assisted transitions, which defines the resonant frequencies where current amplification occurs. As a result, the total current is increased and an additional resonance peak appears, as illustrated in Fig. 2b.

The observed current peak corresponds to the resonant driving frequency ω, which corresponds to the energy difference between electronic states in Floquet

band 3. In other words, the system efficiently absorbs/emits photons at those frequencies, enabling electrons to more easily tunnel through the system and *vice versa*. Consequently, the current is increased or suppressed, and roughly follows the dependence observed in Fig. 2a. Fig. 2 illustrates the interplay between the Floquet band 3 composition of the 1D Fe–Cu molecular chain and a strong LMI, resulting in a highly frequency-dependent transport response. The maximum, corresponding to the driving frequency, is in resonance with the Floquet quasi-energy, enabling photon-assisted tunneling and enhanced current.

It should be noted that the observed peak, which reflects the resonant coupling between the drive and electronic transitions in the hybridized 1D Fe–Cu molecular chain, appears in the low driving frequency range, near to ~1.1 a.u., which is the low-frequency part of the spectrum. Recall that the presence of optimal photon-assisted transport at low frequencies (in the frequency range, covering the THz-mid IR) is a favorable characteristic of materials used to construct energy-efficient devices with robust operation. This is of practical importance for the application of materials, containing Fe–Cu molecular chains. Bearing in mind that new hybridized bands could only appear under the influence of an ultrafast laser (visible light cannot induce the hybridization effect and the opening of a new gap), the observed peak in the low-frequency region of the spectrum (Fig. 2b), confirms the potential usage of the investigated theoretical system of a 1D Fe–Cu molecular chain. Consequently, our modeled system could be employed for practical application in the design of devices operating at frequencies where photon-assisted transport can be efficiently tuned by hybridization effects, such as: THz detectors and sensors,[33] in infrared photodetectors[34] or in low-power optoelectronic switches and modulators,[35] quantum cascade lasers and amplifiers,[36] spintronic devices and magnetic sensors[37] and photovoltaics.[38]

On the other hand, applications of Fe–Cu molecular chains in the low frequency range could face certain disadvantages, such as lower photon energies (which limits access to higher-energy electronic transitions) or slower modulation (the lower frequency limits the velocity, which could be used for switching or modulating devices). Consequently, it could appear a need to shift the resonant peak of the Fe–Cu molecular chain towards a higher frequency range (visible light to UV). This could switch the potential use and practical application of the theoretically considered system, investigated in this study, into the field of ultrafast devices or into the field of nanoscale control. Although the adoption and modification of the considered theoretical system for the application of higher frequency resonance may require more complex materials and control, this represents a research problem that has not yet been satisfactorily resolved. Variation of a discussed parameter, the hybridization strength, in order to shift the resonant peak towards a higher frequencies, is more discussed in the Supplementary material (Fig. S-1).

Impact of the photon-assisted processes on the electric flow in 1D Fe–Cu molecular chain

In the second part of the study, a modified theoretical model, discussed in in the literature,[14] was applied to perform a more precise modeling of electron transfer in a 1D Fe–Cu molecular chain under driving impact, in the strong LMI regime. This approach, at the same time, enables deeper insight into the dependence of the oscillatory electric current on the driving frequency, taking into account the influence of the chemical potential. To investigate electron tunneling, within the Floquet electronic friction model, a more complex form of the Hamiltonian was considered, applied to the case of a 1D Fe–Cu molecular chain. Chen *et al*. considered a general Hamiltonian, consisting of different contributions, describing: the molecule contribution, the leads, the interaction between them, LMI (considered semi-classically) and nuclear degrees of freedom (DoF), in order to postulate a model to describe the quantum transport of a molecular junction.[14] Basically, the model Hamiltonian described a two-level molecular junction, coupled with two baths (leads), where the light induced coupling between the levels.

In our study, similar premises of the model were applied: the model considered a driven two-level system, with nuclear coordinates (bath) coupled to leads and periodic light, applied to a 1D Fe–Cu molecular chain. The given system includes a dissipative bath, in order to represent nuclear relaxation and electronic vibrational modes. The proposal of two metals Fe and Cu leads (electron baths), each with different chemical potentials, allows for the electron injection and extraction of electrons. To postulate our model, two electrons, positioned on two adjacent d-aluminum Fe and Cu orbitals, in a 1D molecular chain, were considered. The modeled system is based on several premises. First, a two-level model is proposed for the molecular part (although, to simplify the complex research issue, only the Fe site will be considered), where electron tunnel *via* coupling with Fe and Cu molecular orbitals is localized at the respective sites. The nuclear degree of freedom is then calculated, considering two vibrational modes, coupled to local Fe or Cu nuclei (as nuclear coordinates, affecting the energy level and coupling, including electronic-photon phonon coupling). Further, LMI was applied, taking into account that the investigated system is driven by an externally applied, ultrafast intense laser, periodically modulating the electronic coupling. The leads are considered in terms of the baths.[14] Finally, the postulated Hamiltonian describes the Fe–Cu molecular sites electronic tunneling, the nuclear vibrational DoF, the coupling to leads and the laser driving LMI. Light induced driving enables transitions between Fe and Cu orbitals, modulated by the term $A\cos \omega t$.[14] Accordingly, the given theoretical model describes the coupling between the Fe and Cu electron sites in a 1D Fe–Cu molecular chain, while the steady-state current is calculated as defined in Eq. (5), and its dependence on applied bias is illustrated in Fig. S-2 of the Supplementary material.

To represent the relationship between electron current and driving frequency in the strong LMI regime: $A = 5$, a corresponding Matlab code was prepared, Fig. 3. It should be mentioned that the applied bias convention (related to the chemical potentials of the leads) took into account: $\mu_L > 0$ and $\mu_R = 0$, as this enabled simplification of the preparation of the transport simulation. Consequently, bias = $\mu_L - \mu_R = \mu_L$, and the chemical potential of the left lead's is shifted positively, since the right lead is taken as a reference to zero chemical potential.

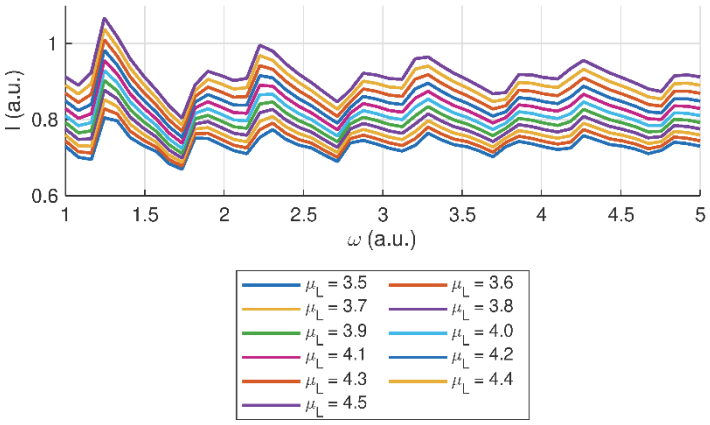

Fig. 3. Steady-state electron current as a function of driving frequency ω in the strong light–matter interaction regime ($A = 5$). The chemical potential μ_L was varied in the range 3.5–4.4 (in model energy units), while μ_R was fixed, illustrating bias-dependent resonance shifts and nonlinear photon-assisted transport behavior.

Fig. 3 illustrates the behavior of the electric current *versus* driving frequency, for different chemical potentials (μ_L), ranging from 3.5 to 4.5, in arbitrary units. Multiple peaks can be observed in $I(\omega)$ for all values of μ_L. It provides deeper insight into the dynamics of electric current behavior in the strong LMI regime. Regular dynamical variations in current behavior could be noticed, *i.e.*, the current decreases with the driving frequency over the entire range of applied bias. Albeit, the current periodically reaches a maximal value, while the observed maxima decrease, with increasing bias. The observed behavior confirmed Chen *et al*. conclusion about non-monotonic behavior of this dependence, and the existence of an optimal frequency that maximizes the electronic current.[14] It should be noted that Fig. 3 shows that the current oscillations behave correlated with the driving frequency, meaning that the chosen driving frequencies result in increased current.

Based on Fig. 3, the current increases, as μ_L approaches a value of 4, while decreasing thereafter. The transition from low to high current occurs smoothly, indicating that the system undergoes resonant-like amplification near $\mu_L = 4$ (in other words, the resonance condition is fulfilled at this value). The purple curve in Fig. 3 represents the highest current, which corresponds to $\mu_L \approx 4$.

The occurrence of current amplification can be understood as the result of the alignment between the driving field, at a given bias ($\mu_L = 4$), and the energy levels. One reason for recognizing the intermediate bias ($\mu_L = 4$), as the one that results in the highest current can be found in the fact that applying low biases can lead to current suppression, while very high biases can lead to saturation or dephasing effects, which can reduce the current. The intermediate bias provides the conditions which results in constructive interference or optimal occupancy probability, producing a stronger maximum. Considering the fact that the bias window characterizes the available states for electron transfer, the intermediate bias could enable a larger effective energy window, and favorable differences in occupancy between the leads, resulting in increased current.

Recall that in quantum transport, which impacts the current behavior, the bias window refers to the energy range over which electrons can flow from one lead to another, due to an applied voltage. Consequently, this is the range in which electronic states can contribute to the flow of current. It represents an optimal bias window, with the optimal number of energy levels represented within the window, so that electrons can tunnel efficiently, and resonant effects can maximize current.

Further, to find the optimal driving frequency (ω) for $\mu_L = 4$, which enables the current maximum, a modified Matlab code was prepared, and the results are presented in Fig. 4a.

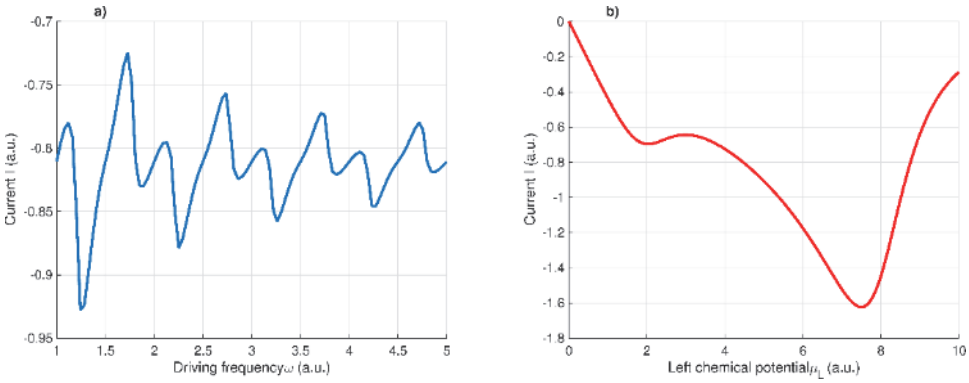

Fig. 4. Dependence of current on driving frequency: a) steady-state current as a function of driving frequency ω at fixed bias ($\mu_L = 4$, μ_R defined by the applied bias), demonstrating frequency-dependent photon-assisted transport; b) current–bias characteristics showing the dependence of steady-state current on the chemical potential μ_L (corresponding to the applied bias voltage), highlighting the modulation of transport by periodic driving. According to Fig. 4a, the current maximum is observed at ω around 1.727 a.u., which depicts to a particular driving frequency for the bias value $\mu_L = 4$. Fig. 4a) also confirms the oscillatory behavior of the given dependence, indicating a non-monotonic behavior with respect to frequency, due to the driving dynamics. Consequently, nonlinear transport dynamic under strong driving in the LMI regime was confirmed.

Fig. 4b represents the changes in current with bias at the optimal frequency; it shows the dependence of the current, on the bias μ_L. In Fig. 4b, the ved current reversal illustrates the dependence of current on bias obser voltage, under resonance driving. It is observed that the current does not increase or decrease uniformly with μ_L, although a drop is observed around μ_L of 7.5, followed by an increase in current. Such behavior indicates that the system is subjected to resonance-like current suppression at certain biases, even though the drive frequency is resonant. The observed drop can be explained differently: it could occur due to the presence of destructive interference between different Floquet transport channels,[39] as a result of detuning the electronic population from the driving-induced resonance condition at high μ_L,[40] or due to minimized net population imbalance or suppression of the contribution of inelastic currents at a given μ_L. It should be noted that at lower biases, the increase in μ_L, initially, leads to an increase in current. But, after that, the current achieves plateau and decreases, indicating a nonlinear bias response and confirming the fact that strong LMI induces nonlinear effects in the system.

Noteworthy, observed feature illustrates the fact that a strong LMI would have a more significant impact on the current, once resonance is reached. The aforementioned effect could be achieved by coherent photon-assisted tunneling which induces enhancement or suppress of the current. Current oscillations appear as a result of resonant coupling between electronic transitions and the drive. The oscillator-dependence of current, observed in Fig. 4, appears as a result of the presence of frequency-dependent resonances in the electric current. If the driving value is equal to the energy difference between the states in Floquet band 3 and the other bands (which occurs at certain frequencies), enhanced photon-assisted tunneling occurs, which increases the current.

It is important to note that given 1D Fe–Cu chain model represents a theoretical model, which captures key features of bimetallic Fe–Cu motifs that are widely studied in heterogeneous catalysis and electrocatalysis, such as CO_2 reduction and selective hydrogenation reactions. In real systems, electron transfer between Fe and Cu sites plays a critical role in catalytic efficiency, and proposed model provides a platform to explore the impact of hybridization strength and periodic driving influence on the electron flow. The Floquet analysis simulates external periodic perturbations, which can be interpreted as light-induced or voltage-modulated excitations in experimental setups. Obtained results indicated that tuning orbital hybridization and applying controlled periodic driving can enhance resonant electron transport between active sites, offering qualitative insight into photon-assisted or dynamically modulated charge transfer in bimetallic catalysts. It should be noted that this study does not aim to quantitatively reproduce any specific Fe–Cu material or electrochemical interface, but to provide a framework

that can guide experimental strategies for improving catalytic and electrochemical performance through controlled electronic dynamics.

Limitations of the model

The present study is based on a minimal theoretical model designed to discuss the essential mechanisms of hybridization-controlled Floquet transport in Fe–Cu motifs. While this approach enabled analytical clarity and transparent numerical implementation, several limitations should be mentioned.

The investigated Fe–Cu system is modeled as an idealized one-dimensional periodic chain (for band analysis) and as a two-level molecular junction (for transport calculations). Real Fe–Cu catalytic materials and electrochemical interfaces possess three-dimensional geometries, structural disorder, surface reconstructions, and complex coordination environments. These structural features are not explicitly included in the present model.

In order to simplify model, electron–electron interactions are neglected beyond effective single-particle descriptions. The Hamiltonian does not include explicit Coulomb interaction terms (*e.g.*, Hubbard U), correlation effects or many-body self-energies. As a consequence, correlation-driven phenomena (such as Kondo physics, strong localization or correlation-induced gap renormalization) are not considered.

The construction of Floquet Hamiltonian is performed, using a finite truncation of photon harmonics. While convergence with respect to the number of harmonics was verified numerically for the parameter regimes considered, extremely strong driving or very high frequencies may require additional harmonics for quantitative accuracy.

Also, it could be noted that the open-system transport treatment is relied on the Born–Markov and secular approximations, characterized by assuming weak molecule–lead coupling, negligible memory effects and well-separated energy scales. In regimes of strong system–bath coupling or highly non-Markovian dynamics, the Master equation approach may lose quantitative accuracy. On the other hand, simplification of the model required to neglect the anharmonic effects, mode–mode coupling and nonequilibrium phonon populations, in order to describe vibrational modes within a harmonic approximation and their treatment as independent baths.

Further, the wide-band approximation is employed for the metallic leads, assuming energy-independent density of states near the Fermi level. Real Fe and Cu electrodes are characterized by structured densities of states, which could modify tunneling rates and resonance conditions.

Finally, the model does not aim to provide a quantitative first-principles description of a specific Fe–Cu catalytic material. Instead, it serves as a minimal

theoretical platform to explore qualitative mechanisms of hybridization-controlled resonance tuning and photon-assisted transport in Fe–Cu motifs.

Despite these limitations, the model captures the essential interplay between orbital hybridization, periodic driving and open-system transport. The simplified framework allows clear identification of resonance shifts and current enhancement mechanisms, which may guide more elaborate future studies based on DFT or experimentally characterized Fe–Cu systems.

CONCLUSIONS

In this study is presented a detailed theoretical framework for the transport properties of a Fe–Cu molecular chain under periodic driving. Application of Floquet theory allowed modulation of electronic states *via* photon-assisted processes. Master equation approach captured electron tunneling under bias and vibrational interactions. Consequently, it is shown that hybridization control shifts the static and quasi-energy gaps, tuning resonance frequencies. Performed study demonstrated that integrating Floquet quasi-energy analysis with master-equation-based transport allows controlled modulation of electron flow in Fe–Cu chains, providing a novel perspective on driven electron dynamics that goes beyond traditional approaches focused solely on band structure or open-system transport. Futrher, the distinction between orbital hybridization (static Fe–Cu overlap) and Floquet mixing (laser-induced coupling to photon states) is clarified. The model demonstrated that careful tuning of driving amplitude and frequency can enhance or suppress electron current, providing insight for future nanoscale devices. Although idealized, presented results establish a foundational understanding of photon-assisted transport in Fe–Cu chains, forming a basis for further work connecting 1D theoretical models with realistic Fe–Cu catalytic systems or experimental electrochemical interfaces.

SUPPLEMENTARY MATERIAL

Additional data and information are available electronically at the pages of journal website: https://www.shd-pub.org.rs/index.php/JSCS/article/view/13511, or from the corresponding author on request. The computational codes used in this study are openly available at GitHub, archived in Zenodo.[41] The repository includes scripts for constructing the k-dependent Bloch Hamiltonian, generating the Floquet matrix under periodic driving, performing numerical diagonalization, and reproducing the quasi-energy spectra and harmonic composition figures reported in this work.

Acknowledgement. The research was funded by the Ministry of Education, Science and Technological Development of the Republic of Serbia (451-03-136/2025-03/ 200017).

ИЗВОД

ПРИМЕНА ФЛОКЕОВЕ ТЕОРИЈЕ И УНАПРЕЂЕЊЕ КОНТРОЛЕ ТОКА ЕЛЕКТРОНСКЕ СТРУЈЕ У 1D Fe–Cu МОЛЕКУЛСКОМ ЛАНЦУ

ВИОЛЕТА Н. НИКОЛИЋ[1] и JOSE F. M. L. MARIANO[2,3]

[1]Лабораторија за теоријску физику и физику кондензоване материје (020) Институт Нуклеарних Наука "Винча", Институт од националног значаја, Универзитет у Београду, п.пр. 522, 11001 Београд, [2]FCT, Campus de Gambelas, University of Algarve, Faro, 8005-139, Portugal и [3]Center of Physics and Engineering of Advanced Materials (CeFEMA), IST, University of Lisbon, Av. Roviscno Pais, Roviscno Pais, Lisbon, 1096-001, Portugal

Извршена студија дискутује примену Флокеове теорије на 1D Fe–Cu молекулски ланац. Потврђено је да ефекат хибридизације орбитала омогућује испуњење резонантног услова у спектру нижих драјвинг фреквенција ове структуре, што карактерише њену потенцијалну примену у енергетски ефикасним уређајима. Даље, ово је први пут да је Флокеов модел електронског трења (базиран на разматрању утицаја Флокеовог драјва на трансфер електрона) у присуству интеракције светлости и материје (LMI), био примењен на 1D Fe–Cu молекулски ланац. Разматрано је понашање електронске струје, а присуство ограничавајуће фреквенције, која максимизира електронску струју, је потврђено. У оквиру ове студије, постављени су одговарајући модели, који дискутују два начина помоћу којих се може појачати електрична струја под утицајем драјва у јаком LMI режиму: путем ефекта орбиталне хибридизације и путем фотонски потпомогнутих процеса. Добијени резултати би могли унапредити практичну примену материјала који садрже Fe–Cu молекулске ланце у електрохемији.

(Примљено 22. августа2025, ревидирано 5. фебруара, прихваћено 18. марта 2026)

REFERENCES

1. C. Tang, M. Shiri, H. Zhang, R. T. Ayinla, K. Wang, *Nanomaterials* **12** (2022) 698 (https://doi.org/10.3390/nano12040698)
2. B. Dong, H. L. Cui, X. L. Lei, *Phys. Rev., B* **69** (2004) 205315 (https://doi.org/10.1103/PhysRevB.69.205315)
3. B. D. Fainberg, *Phys. Rev., B* **88** (2013) 245435 (https://doi.org/10.1103/PhysRevB.88.245435)
4. G. Platero, R. Aguado, *Phys. Rep.* **395** (2004) 1 (https://doi.org/10.1016/j.physrep.2004.01.004)
5. G. Floquet, *Ann. Sci. Éc. Norm. Supér.* **12** (1883) 47 (https://doi.org/10.24033/asens.220)
6. Y. Wang, W. Dou, *ACS Phys. Chem. Au* **4** (2023) 160 (https://doi.org/10.1021/acsphyschemau.3c00049)
7. Z. Zhou, H. T., Chen, A. Nitzan, J. E. Subotnik, *Chem. Theory Comput.* **16** (2020) 821 (http://doi.org/10.1021/acs.jctc.9b00950)
8. H. Carias, D. N. Beratan, S. S. Skourtis, *J. Phys. Chem., B* **115** (2011) 5510 (https://doi.org/10.1021/jp111097a)
9. V. Mosallanejad, Y. Wang, J. Chen, W. Dou, *Wiley Interdiscip. Rev. Comput. Mol. Sci.* **15** (2025) e70032 (https://doi.org/10.1002/wcms.70032)
10. M Hromadová, F. Vavrek, *Curr. Opin. Electrochem.* **19** (2020) 63 (https://doi.org/10.1016/j.coelec.2019.10.008)
11. J. Song, E. Khoo, E., M. Z. Bazant, *Phys. Rev., E* **100** (2019) 042204 (https://doi.org/10.1103/PhysRevE.100.042204)

12. Y. Han, C. Nickle, M. S. Maglione, S. K. Karuppannan, J. Casado-Montenegro, D. C. Qi, X. Chen, A. Tadich, B. Cowie, M. Mas-Torrent, C. Rovira, J. Cornil, J. Veciana, E. del Barco, C. A. Nijhuis, *Adv. Sci.* **8** (2021) 2100055 (http://doi.org/10.1002/advs.202100055)
13. E. Leary, B. Limburg, A. Alanazy, S. Sangtarash, I. Grace, K. Swada, L. J. Esdaile, M. Noori, M. T. González, G. Rubio-Bollinger, H. Sadeghi, A. Hodgson, N, Agraït, S. J. Higgins, C. J. Lambert, H. L. Anderson, R. J. Nichols, *J. Am. Chem. Soc.* **140** (2018) 12877 (http://doi.org/10.1021/jacs.8b06338)
14. J. Chen, W. Liu, V. Mosallanejad, W. Dou, *J. Phys. Chem., C* **128** (2024) 11219 (http://doi.org/10.1021/acs.jpcc.4c00969)
15. X. Wei, S. Wei, S. Cao, Y. Hu, S. Zhou, S. Liu, Z. Wang, X. Lu, *Appl. Surf. Sci.* **564** (2021) 150423 (http://doi.org/10.1016/j.apsusc.2021.150423)
16. F. Schwarz, G. Kastlunger, F. Lissel, H. Riel, K. Venkatesan, H. Berke, R. Stadler E. Lörtscher, *Nano Lett.* **14** (2014) 5932 (http://doi.org/10.1021/nl5029045)
17. M. Farsad, M. Elahifard, R. Behjatmanesh-Ardakani, *Theor. Chem. Acc.* **137** (2018) 142 (https://doi.org/10.1007/s00214-018-2346-5)
18. B. J. Lee, B. D. Wirth, J. H. Shim, J. Kwon, S. C. Kwon, J. H. Hong, *Phys. Rev., B* **71** (2005) 184205 (https://doi.org/10.1103/PhysRevB.71.184205)
19. A. I. Fadeeva, V. A. Gorbunov, P. V. Stishenko, A. V. Myshlyavtsev, *J. Phys. Chem. C* **123** (2019) 17265-17272 (https://doi.org/10.1021/acs.jpcc.9b02834)
20. C. Domain, C. S. Becquart, *Phys. Rev., B* **65** (2001) 024103 (https://doi.org/10.1103/PhysRevB.65.024103)
21. *MATLAB version: 9.13.0 (R2022b)*, The MathWorks Inc., Natick, MA, 2022 (https://www.mathworks.com) (accessed 20.06.2025)
22. M. Schönberg, *Nuovo Cim.* **10** (1953), 697 (http://doi.org/10.1007/BF02773031); F. Schwarz, G. Kastlunger, F. Lissel, H. Riel, K. Venkatesan, H. Berke, R. Stadler, E. Lörtscher, *Nano Lett.* **14** (2014) 5932 (http://doi.org/10.1021/nl5029045)
23. J. C. Slater, G. F. Koster, *Phys. Rev.* **94** (1954) 1498 (http://doi.org/10.1103/PhysRevB.94.1498)
24. K. Nakamura, R. Arita, H. Ikeda, *Phys. Rev., B* **83** (2011) 144512 (http://doi.org/10.1103/PhysRevB.83.144512)
25. A.-P. Jauho, N. S. Wingreen, Y. Meir, *Phys. Rev., B* **50** (1994) 5528 (http://doi.org/10.1103/PhysRevB.50.5528)
26. M. Galperin, M. A. Ratner, A. Nitzan, *J. Phys.: Condens. Matter* **19** (2007) 103201 (http://doi.org/10.1088/0953-8984/19/103201)
27. H. Park, J. Park, A. K. L. Lim, E. H. Anderson, A. P. Alivisatos, P. L. McEuen, *Nature* **407** (2000) 57 (http://doi.org/10.1038/35024031)
28. J. Chen, W. Liu, V. Mosallanejad, W. Dou, J. *Phys. Chem., C* **128** (2024) 11219 (http://doi.org/10.1021/acs.jpcc.4c00969)
29. A. P. Sutton, M. W. Finnis, D. G. Pettifor, Y. Ohta, *J. Phys., C* **21** (1988) 35 (http://doi.org/10.1088/0022-3719/21/1/007)
30. C. X. Zhang, M. A. Zubkov, *Phys. Rev., D* **100** (2019) 116021 (http://doi.org/10.1103/PhysRevD.100.116021)
31. M. Holthaus, *J. Phys., B* **49** (2015) 013001 (http://doi.org/10.1088/0953-4075/49/1/013001)
32. D. Zhang, Y. Zeng, Y. Tian, R. Li, *Phot. Insights* **2** (2023) R07 (http://doi.org/10.3788/PI.2023.R07)

33. K. Blum, H. Kleinpoppen, *Phys. Rep.* **52** (1979) 203 (http://doi.org/10.1016/0370-1573(79)90031-0)
34. X. Meng, X. Jing, J. Cheng, H. Tang, X. Chen, X. Zhou, L. Li, *ACS Appl. Nano Mater.* **7** (2024) 8175 (http://doi.org/10.1021/acsanm.4c00709)
35. J. Xie, L. Wang, J. S. Anderson, *Chem. Sci.* **11** (2020) 8350 (https://doi.org/10.1039/d0sc03429k)
36. H. Xiao, G. L. Wu, S. Tan, X. Tan, Q. Yang, *Chem. Asian J* **19** (2024) e202301036 (http://doi.org/10.1002/asia.202301036)
37. J. Liu, K. Luo, H. Chang, B. Sun, Z. Wu, *Nanomaterials* **11** (2021) 2713 (http://doi.org/10.3390/nano11102713)
38. J. M. Raulot, C. Domain, J. F. Guillemoles, *Phys Rev., B* **71** (2005) 035203 (http://doi.org/10.1103/PhysRevB.71.035203)
39. M. Acquarone, P. Monachesi, *Phys Rev., B* **38** (1988) 2555 (http://doi.org/10.1103/PhysRevB.38.2555)
40. M. Moskalets, M. Büttiker, *Phys Rev., B* **78** (2008) 035301 (http://doi.org/10.1103/PhysRevB.78.035301)
41. Violeta10203 (2026). Floquet_1D_Fe_Cu_system (Version v3.0) [Matlab code], Zenodo, https://doi.org/10.5281/zenodo.19096574.

Journal of the Serbian Chemical Society
JSCS@tmf.bg.ac.rs • www.shd.org.rs/JSCS
J. Serb. Chem. Soc. 91 (4) S122–S126 (2026) *Supplementary material*

SUPPLEMENTARY MATERIAL TO

Application of Floquet theory and improvement of electron current flow control in a 1D Fe–Cu molecular chain

VIOLETA N. NIKOLIĆ[1]* and JOSE F. M. L. MARIANO[2,3]

[1]Department of Theoretical Physics and Condensed Matter Physics (020) Vinča Institute of Nuclear Sciences, National Institute of the Republic of Serbia, University of Belgrade, P.O. Box 522, 11001 Belgrade, Serbia, [2]FCT, Campus de Gambelas, University of Algarve, Faro, 8005-139, Portugal and [3]Center of Physics and Engineering of Advanced Materials (CeFEMA), IST, University of Lisbon, Av. Roviscno Pais, Roviscno Pais, Lisbon, 1096-001, Portugal

J. Serb. Chem. Soc. 91 (4) (2026) 331–352

VARIATION OF THE HYBRIDIZATION STRENGTH

To discuss in more details the shift, of the resonant peak of 1D Fe-Cu molecular chain, towards a higher frequency, it was prepared a corresponding Matlab code, designed to illustrate the potential shift of the resonant frequency of a 1D Fe-Cu molecular chain towards higher frequencies. A variation of the chosen parameter (V) was considered to enable the discussed shift in the resonant frequency, confirming the effect of hybridization strength on Floquet band structure, Fig. S-1.

As it known, a shift in the resonant frequency can be achieved by modifying the parameters, affecting the energy gap in the investigated hybridized 1D Fe-Cu molecular chain Floquet band structure. Although three parameters affect the energy gap: V, on-site energy, and hopping amplitude,[1] for simplicity, the influence of only one parameter, the hybridization strength, will be commented here.

* Corresponding author. E-mail: violeta@vin.bg.ac.rs

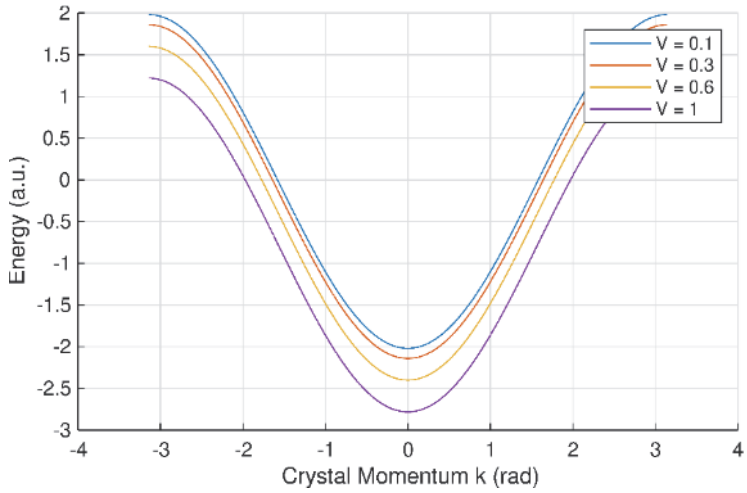

Fig. S-1. Floquet quasi-energy bands of the 1D Fe–Cu molecular chain for different orbital hybridization strengths V. Increasing V (color-coded curves) widens the static energy gap at k=0 and shifts the Floquet resonance to higher photon frequencies. The horizontal axis shows crystal momentum k in units of π/a (with lattice spacing a), and the vertical axis shows quasi-energy in eV. Static orbital hybridization is distinct from Floquet mixing with photon states.

Fig. S-1 represents the effect of increasing the hybridization strength parameter to shift the resonance frequency upward. Let us recall here that the parameter V represents the strength of orbital overlap or hybridization between Fe and Cu orbitals. Increasing the strength of hybridization widens the energy gap between the two hybridized bands, effectively increasing the minimum energy difference at k=0. Since the resonant photon frequency ω roughly corresponds to this energy gap, increasing V shifts the resonance towards a higher ω. In other words, applying external conditions (such as temperature, pressure or strain), that induces a higher amount of orbital overlap or stronger hybridization, can lead to a shift in the resonance photon frequency towards a higher frequency range.

EQUATIONS

Equations employed in the electrochemical study

After postulation of the modeled Hamiltonian, in the second part of the study, further mathematical treatment of the given system, which enabled monitoring of leads and vibrations, considered the postulation of the master equation.[2] The master equation was solved numerically in MATLAB using standard linear algebra routines to propagate the reduced density matrix in time until steady state. This numerical propagation captures the coherent evolution due to the time-dependent Hamiltonian and the incoherent dissipative effects due to coupling with the leads and vibrational baths.

Accordingly, several approximations have been considered, such as: Born approximation (it is supposed weak coupling between molecule and leads, so that the leads remain in equilibrium states),[3] Markov approximation (memory effects are neglected, and it was proposed that the dynamic is dependent only on the current ρ(t)),[4] secular approximation (fast oscillating off-diagonal elements (dependent on energy gaps) are neglected),[5] wide band approximation (the leads density of states assumed to be energy independent, close to the Fermi level),[6] and finally, it is proposed that the leads are in thermal equilibrium (with chemical potentials μ_L, μ_R to model bias). As a result, it was possible to discuss electron tunneling under bias voltage, vibrational coupling, and external driving.

The master equation has the form of the expression, eq. (S1):

$$\frac{d}{dt}\rho(t) = \frac{-i}{\hbar}[H_{mol} + H_{mol-vib} + H_{drive}, \rho(t)] + L_{leads}[\rho(t)] + L_{vib}[\rho(t)] \quad \text{(S1)}$$

where the commutator is used to describe the coherent evolution under the system Hamiltonian, and the external driving; L_{leads} is the dissipative superoperator for electron tunneling, associated with the leads, while L_{vib} is the dissipative superoperator for the vibration environment, reflected in the phonon damping. Eq. (S1) is equivalent to eq. (11), in the main text; it is written here in expanded form to show the contributions from leads and vibrational baths explicitly.

The total Hamiltonian, related to the time-dependent driving term (ultrafast laser), is given by the expression below:

$$H_{drive}(t) = A\cos(\omega t)\hat{O} \quad \text{(S2)}$$

In eq. (S2), the operator magnitude represents the operator coupled to the driving.

Finally, the current from the lead is calculated by applying eq. (S3):

$$I_a(t) = eTr(J_a[\rho(t)]) \quad \text{(S3)}$$

where J_a represents the current superoperator, attributed to electrons tunneling through the lead a, and e is the elementary charge. Given expression corresponds to the actual physical current in amperes.

Numerical treatment of the postulated model enabled the preparation of a Matlab code, the execution of which enabled a visual representation of the modeling of the dependence of the electronic current on the bias, in the case of a 1D Fe-Cu chain. The results are shown in Fig. S-2, representing electron current dependence on the bias, for different driving amplitudes (A) and frequencies (ω).

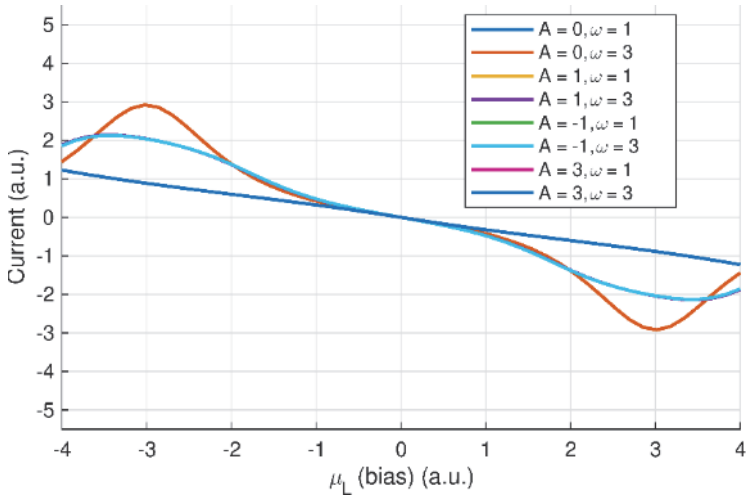

Fig. S-2. Steady-state electron current I (vertical axis, in nA) as a function of applied bias voltage V_{bias} (horizontal axis, in V), for three Floquet driving regimes: absence of driving: A=0, ω=1 eV (blue curve), moderate driving: A=−1, ω=3 eV (light blue curve), and strong driving: A=3, ω=3 eV (dark blue curve). The periodic driving term (Acos(ωt)) modulates the molecular energy levels, influencing electron tunneling probabilities. The curves illustrate photon-assisted current enhancement and suppression effects. All results are obtained using the master equation and parameters in Table I (main text).

Fig. S-2 represents the dependence of electron on bias, for different driving amplitudes (A) and frequencies (ω). Each curve corresponds to different driving amplitudes A and frequencies ω of the periodic driving of the system. Floquet driving, reflected in the term Acos(ωt), affects the curves describing the dependence of the bias on the electric current flowing through the modeled system, modulating the energy levels of the system. As a result, changing quantum states affects the electron tunneling probabilities. Variation in the driving amplitude and frequency impacts the resonance conditions, and consequently, the current.

Only three basic cases were considered, obtained by varying the driving amplitude: absence of driving, moderate driving, and strong driving. In the case when the driving amplitude is zero (absence of driving), the current occurs only due to the static bias. In the case when A = ±2 (moderate driving), the current depends on the phase and frequency, and can consequently be amplified or suppressed. This is more pronounced in the case of A = ±3, where strong driving can cause nonlinear effects, affecting the current in a way that results in suppression or more complex behavior. Accordingly, three selected cases are presented in Fig. 4, illustrating curves representing three basic regimes: the dark blue curve, representing strong driving (A = 3, ω = 3), the light blue curve (moderate driving, A = -1, ω = 3), and the red curve (no driving case, A = 0, ω = 1). The influence of the driving and LMI was explained in terms of the laser

influence, whose interaction with the Fe-Cu molecular chain triggered photo-induced forces. As a final result, change in the tunneling rates occurs. Consequently, fine tuning of the driving amplitude and frequency, enables the enhancement of electron transport via photon-assisted processes.

REFERENCES

1. K. Blum, H. Kleinpoppen, *Phys. Rep.* **52** (1979) 203 (http://doi.org/10.1016/0370-1573(79)90031-0)
2. A. Nordsieck, Jr W. E. Lamb, G. E. Uhlenbeck, *Physica* **7** (1940) 344 (http://doi.org/10.1016/S0031-8914(40)90102-1)
3. M. Born, *Z. Phys* **38** (1926) 803 (http://doi.org/10.3367/UFNr.0122.197708g.0632)
4. S. Nakajima, On quantum theory of transport phenomena: Steady diffusion. *Prog. Theor. Phys* **20** (1958) 948 (http://doi.org/10.1143/PTP.20.948)
5. E. B. Davies, *Commun. Math. Phys.* **39** (1974) 91 (http://doi.org/10.1007/BF01608389)
6. A. P. Jauho, N. S. Wingreen, Y. Meir, *Phys Rev B* **50** (1994) 5528 (http://doi.org/10.1103/PhysRevB.50.5528).

Journal of the Serbian Chemical Society
JSCS@tmf.bg.ac.rs • www.shd.org.rs/JSCS
J. Serb. Chem. Soc. *91* (4) 353–370 (2026)
JSCS–5496
Original scientific paper
Published 1 May, 2026

In silico evaluation of phycobilins as multi-target anti-tubercular scaffolds: Molecular docking, dynamic stability, ADMET and mycobacterial sensitivity analysis

AMELA K. LEPOJEVIĆ[1], MIROSLAV M. JEVTIĆ[1], MARIO V. ZLATOVIĆ[2] and SRĐAN Đ. STOJANOVIĆ[3]*

[1]*Special Hospital for Pulmonary Diseases and Tuberculosis "Ozren", Sokobanja, Serbia,* [2]*University of Belgrade, Faculty of Chemistry, Department of Organic Chemistry, Belgrade, Serbia and* [3]*University of Belgrade, Institute of Chemistry, Technology and Metallurgy – National Institute of the Republic of Serbia, Department of Chemistry, Belgrade, Serbia*

(Received 24 January, revised 2 February, accepted 5 February 2026)

Abstract: Tuberculosis remains a major global health burden, highlighting the urgent need for novel therapeutic scaffolds with imbproved efficacy and multi-target activity. In this study, an integrated *in silico* strategy was used to investigate the anti-tubercular potential of four naturally occurring phycobilins – phycocyanobilin, phycoerythrobilin, phycourobilin and phycoviolobilin – against a panel of essential *Mycobacterium tuberculosis* protein targets involved in cell wall biosynthesis, nucleic acid metabolism, energy production and ribosomal function. Molecular docking analyses revealed consistently strong binding affinities of phycobilins toward multiple targets, often exceeding those of isoniazid and approaching the binding performance of rifampicin, indicating pronounced multi-target interaction capability. Noncovalent interaction analysis showed stable and diverse interaction networks dominated by hydrogen bonding and hydrophobic contacts. Normal mode analysis confirmed that phycobilin binding preserves intrinsic protein dynamics while inducing ligand-mediated stabilization of the protein–ligand complexes, particularly for the phycoviolobilin–InhA system. Pharmacokinetic and toxicity predictions suggested moderate distribution properties and generally favorable safety profiles, although potential mutagenicity and skin sensitization signals were identified. Additionally, mycoCSM-based predictions indicated micromolar-range anti-mycobacterial activity with limited penetration into caseous lesions. Collectively, these results support phycobilins as promising natural scaffolds for anti-tubercular drug discovery, warranting further optimization and experimental validation.

Keywords: phycobilins; tuberculosis; inhibitors; proteins; *in silico* studies.

* Corresponding author. E-mail: srdjan.stojanovic@ihtm.bg.ac.rs
https://doi.org/10.2298/JSC260124006L

INTRODUCTION

Tuberculosis (TB), caused by *Mycobacterium tuberculosis*, remains a leading cause of mortality from a single infectious agent worldwide, despite established chemotherapeutic regimens. The global rise of multidrug-resistant (MDR) and extensively drug-resistant (XDR) TB strains, along with prolonged treatment durations and dose-limiting toxicities, continues to undermine therapeutic success and highlights the urgent need for novel anti-tubercular agents with improved efficacy and resistance-mitigating properties.[1] These challenges have driven a paradigm shift in TB drug discovery toward strategies that extend beyond single-target inhibition.[2]

The mycobacterial cell is defined by a highly complex and resilient structure, including a lipid-rich cell wall, specialized metabolic pathways, and tightly regulated transcriptional and translational machinery. Key enzymes involved in fatty acid synthesis (such as InhA and KasA), arabinan and peptidoglycan biosynthesis, nucleic acid processing, ribosomal stability and energy production have been validated as drug targets in TB chemotherapy.[3,4] Drugs that interact with those multiple targets may produce synergistic inhibitory effects, reduce bacterial adaptability and enhance sterilizing activity. As a result, multi-target drug discovery has received considerable attention as a rational framework for next-generation TB therapeutics.[5]

Natural products remain a valuable source of structurally diverse and biologically validated scaffolds for antimicrobial drug discovery. Among these, phycobilins are linear tetrapyrrolic pigments derived from cyanobacteria and algae, primarily known for their role in photosynthetic light harvesting and for various reported pharmacological activities, including antioxidant, anti-inflammatory and cytoprotective effects.[6] Their extended conjugated systems, conformational flexibility and extensive hydrogen-bonding capacity suggest an inherent potential to engage diverse protein targets. However, the anti-mycobacterial and molecular interaction profiles of phycobilins remain largely unexplored.

Advances in computational chemistry and structural bioinformatics have enabled the systematic evaluation of multi-target ligand behavior in the early stages of drug discovery. Blind molecular docking allows rapid identification of binding sites and interaction modes across diverse protein targets, while normal mode analysis (NMA) provides critical insight into ligand-induced conformational dynamics and complex stability beyond static affinity metrics.[7–9] In parallel, *in silico* pharmacokinetic, toxicity and pathogen-specific activity prediction platforms facilitate early identification of drug-likeness, safety liabilities and therapeutic relevance, streamlining lead prioritization.[10,11]

In this study, we used an integrated *in silico* workflow to evaluate the anti-tubercular potential of four naturally occurring phycobilins – phycocyanobilin, phycoerythrobilin, phycourobilin and phycoviolobilin – against a diverse panel of

essential *M. tuberculosis* protein targets representing multiple biological processses. By combining molecular docking, noncovalent interaction profiling, normal mode analysis, ADMET prediction and mycobacterial sensitivity modeling, this work assesses the feasibility of phycobilins as multi-target, lead-like scaffolds for rational anti-tubercular drug development.

EXPERIMENTAL

Molecular docking

Chemical structures of the ligands (phycocyanobilin, phycoerythrobilin, phycourobilin, phycoviolobilin, isoniazid and rifampicin) were retrieved in SDF format from the PubChem compound database (http://www.pubchem.ncbi.nlm.nih.gov/search)[12] for subsequent molecular docking and binding affinity analysis. The three-dimensional (3D) structures of the proteins (Table I) were obtained in PDB format from the RCSB Protein Data Bank (https://www.rcsb.org).[13] Docking studies were performed using the CB-Dock2 server (https://cadd.labshare.cn/cb--dock2/),[14] an advanced protein–ligand blind docking server with improved binding site identification and binding pose prediction. The submitted ligand was processed by adding hydrogens and partial charges and an initial 3D conformation was generated using RDKit (RDKit: Open--source cheminformatics, https://www.rdkit.org). CB-Dock2 checks the submitted protein, adds missing side-chain and hydrogen atoms, notifies users of missing residues and removes co--crystallized waters and other heteroatoms. CB-Dock2 performs protein–ligand blind docking by integrating cavity identification, docking and homologous template fitting. It improves blind docking by identifying the protein's binding cavities and generating the predicted dimensions and centers using the latest version of AutoDock Vina (v. 1.2.0).[15] Using these techniques, CB--Dock2 provides more accurate predictions of protein–ligand interactions. Interaction profiles and visualizations were generated for the best-docked complexes. The docked protein–ligand interactions were visualized using Biovia Discovery Studio Visualizer 2025.[16]

Noncovalent interaction analysis

The docked protein and ligand interactions were analyzed and visualized using Biovia Discovery Studio Visualizer 2025 with default-specific criteria and geometrical feature settings.[16]

Normal mode analysis (NMA)

Docked protein–phycobilin complexes were analyzed by normal mode analysis (NMA) using the iMODS server (https://imods.iqf.csic.es).[8] The iMODS platform was used to characterize the structural dynamics and stability of docked complexes by analyzing deformability, B--factors, eigenvalues, variance, covariance maps and elastic network properties. From a single structure, the server calculates the lowest-frequency normal modes using internal coordinates. This dual approach enabled comprehensive assessment of ligand-induced conformational changes and dynamic stability within the protein–phycobiln systems. The computational efficiency of this approach has enabled the evaluation of large-scale motions and dynamic transitions of proteins without excessive computational resources.[8,17] The coarse-grained CA atomic model and the elastic network model were used to balance computational efficiency and accuracy in predicting global motions. The normal mode value indicates motion stiffness, with lower eigenvalues representing simple bending motions in relation to the energy required for these deformations.

Pharmacokinetic and toxicity profiles

ADMET properties refer to drug absorption, distribution, metabolism, excretion and toxicity. They are useful for predicting pharmacological and toxicological characteristics in preclinical stages. We used the freely accessible Deep-PK online tool (https://biosig.lab.uq.edu.au/deeppk/) to evaluate the pharmacokinetics of the phycobilins.[18] The SMILES format of the phycobilins was retrieved from the PubChem database and used as input for the Deep-PK server.

Prediction of anti-tuberculosis sensitivity

In this study, we used the online server mycoCSM (https://biosig.lab.uq.edu.au/myco_csm) to predict the anti-tubercular activity of the phycobilins.[11] The SMILES format of the phycobilins was uploaded as an input form, and the analysis report was downloaded in CSV format. The anti-mycobacterial activity, caseum fraction unbound (FU) and maximum recommended tolerated doses (MRTD) for the phycobilins were determined.

RESULTS AND DISCUSSION

Proteins are essential for maintaining membrane integrity and supporting metabolic functions, making them promising targets for drug development. We used a standard *in silico* approach to investigate the multi-target specificity of phycobilins against protein targets involved in processes ranging from membrane synthesis to nucleic acid metabolism, which are also targeted by antibiotics currently recommended for tuberculosis treatment.[3] Phycobilins were selected for their reported pharmacological activities[6] and serve as representative candidates in this study, which focuses on their therapeutic potential against *Mycobacterium*

TABLE I. The proteins targeted in this study and their corresponding PDB IDs

Target	Function	PDB ID
Enoyl-[acyl-carrier-protein] reductase (NADH)	Build long-chain fatty acids, that form the tough mycobacterial cell wall.	2NSD
KasA	Essential enzyme in the bacterium's unique cell wall synthesis (FAS-II system).	2WGD
Pantothenate synthetase (Mtb PanC)	Vital enzyme in the tuberculosis bacterium's essential pathway for making Coenzyme A.	3COW
Arabinosyl transferase	Responsible enzyme for adding arabinose sugars to build LAM, a vital component of the bacterial cell wall.	3PTY
DNA Gyrase	Introduces negative supercoils into DNA.	4G3N
Ribosomal protein S1	Important protein involved in the functioning of the bacterial ribosome.	4NNI
MurB	Crucial enzyme for building the bacterial cell wall's peptidoglycan layer.	5JZX
2′-*O*-methyltransferase TlyA	Regulate ribosome stability.	5KYG
Protein kinase B	Crucial serine/threonine protein kinase, essential for bacterial growth, cell wall maintenance, division and switching between active replication and dormant states.	5U94
ATP synthase epsilon chain	Vital enzyme for the pathogen's energy production.	5YIO
DNA-directed RNA polymerase	Crucial enzyme for targeting promoters and initiating gene expression.	5ZX3

tuberculosis. In the initial stage of our research, we conducted a molecular docking study of the ligands (phycobilins) to determine their intermolecular interactions with amino acid residues at the active sites of the target proteins (Table I). In the second phase, based on the docking results, we subjected the screened compounds to ADME-Tox and drug-likeness analyses, as well as anti-tuberculosis sensitivity prediction.

Molecular docking studies

Predicting interactions between proteins and small molecules is essential for understanding many biological processes and is crucial for elucidating protein functions and advancing drug development.[19] Protein–ligand blind docking is a powerful approach that identifies the binding regions of a protein and simultaneously predicts the binding pose of a molecule.[20,21] To assess potential efficacy, we performed molecular docking of phycobilins with the target proteins (Table II, Scheme 1). For comparison, Table III presents molecular docking analyses of protein targets with the known anti-tubercular drugs isoniazid and rifampicin. For each protein–ligand pair, five poses were generated using the CB--Dock-2 server. We selected the pose with the highest binding energy and the lowest Vina score, indicating the strongest interaction between the ligand and the protein's active site. This pose represents the most stable complex and demonstrates the affinity and efficacy of these compounds as ligands for the target proteins. The docking scores reported by the CB-Dock-2 server represent relative shape complementarity values, not absolute binding free energies. These correlation-based scores are expressed in arbitrary units scaled to kJ mol^{-1}.

TABLE II. Docking server results for phycobilins

PDB ID	Phycocyanobilin		Phycoerythrobilin		Phycourobilin		Phycoviolobilin	
	Vina score kJ mol^{-1}	Cavity volume Å^3	Vina score kJ mol^{-1}	Cavity volume Å^3	Vina score kJ mol^{-1}	Cavity volume Å^3	Vina score kJ mol^{-1}	Cavity volume Å^3
2NSD	–43.9	2016	–43.5	2016	–43.9	3035	–46.0	2016
2WGD	–29.3	228	–30.5	154	–28.0	154	–28.9	228
3COW	–38.9	3510	–40.6	3510	–41.8	3510	–40.6	3096
3PTY	–38.5	272	–36.0	272	–33.9	272	–35.1	103
4G3N	–35.6	3623	–37.2	3623	–35.1	3623	–33.9	3623
4NNI	–33.9	286	–40.2	286	–31.8	286	–34.7	286
5JZX	–38.9	3638	–38.1	5932	–36.8	7382	–40.6	5139
5KYG	–31.0	322	–32.6	322	–32.2	322	–33.5	322
5U94	–38.5	1704	–40.2	1704	–37.7	1704	–33.5	1704
5YIO	–31.0	242	–32.2	242	–30.1	86	–30.5	86
5ZX3	–37.7	3507	–45.2	3964	–44.8	3964	–41.4	3964

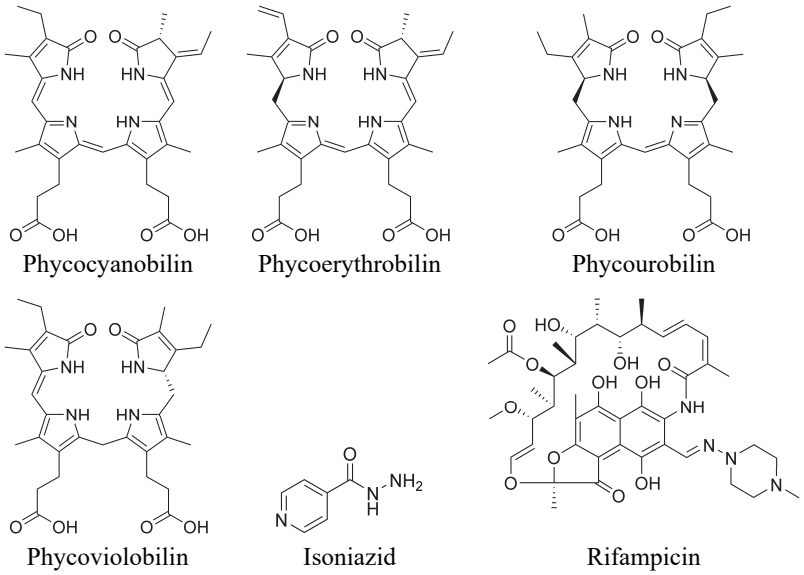

Scheme 1. Structures of phycocyanobilin, phycoerythrobilin, phycourobilin, phycoviolobilin, isoniazid and rifampicin.

TABLE III. Docking server results for antibiotics

PDB ID	Isoniazid		Rifampicin	
	Vina score, kJ mol^{-1}	Cavity volume, Å^3	Vina score, kJ mol^{-1}	Cavity volume, Å^3
2NSD	–25.5	3035	–39.7	3035
2WGD	–25.9	767	–30.5	228
3COW	–24.7	3510	–31.4	3096
3PTY	–24.3	272	–39.3	272
4G3N	–20.1	3623	–36.0	3623
4NNI	–22.2	598	–67.4	598
5JZX	–24.3	7382	–31.0	5932
5KYG	–23.8	183	–32.6	183
5U94	–21.3	362	–33.5	1704
5YIO	–20.5	242	–29.3	242
5ZX3	–25.9	3964	–43.1	13175

It should be emphasized that the Vina scores reported by the CB-Dock2 server represent relative shape complementarity and predicted binding affinity, not absolute experimental binding free energies. These values are useful for ranking and prioritizing potential scaffolds but should be interpreted as theoretical indicators of interaction strength rather than precise thermodynamic measurements.

Molecular docking analyses showed that all four phycobilins had excellent binding affinity for the active sites of the proteins 2NSD, 3COW, 5JZX and 5ZX3 (Vina score < –40 kJ mol^{-1}), indicating their suitability as ligands for these proteins (Table II). In comparison, the docking results showed that the docking scores

of the other target proteins ranged from –28 to –40 kJ mol^{-1}, indicating significant binding affinity. These results suggest that all phycobilins have a stronger predicted binding affinity than the reference antibiotic isoniazid (Table III). In contrast, rifampicin showed docking scores similar to those of the phycobilins and exhibited high affinity for the target proteins. The present study also predicted that the suggested natural compounds may be multi-target specific. The ability to target multiple cellular mechanisms, such as cell wall biosynthesis, nucleic acid synthesis and metabolic integrity of the pathogen, could enhance the potential of these compounds as potent multi-targeted anti-tubercular agents.[4]

Based on molecular docking results showing favorable binding affinities, phycobilins with the lowest Vina scores were selected for further analysis of their interaction profiles with all target proteins, focusing on noncovalent interactions (Table IV).

TABLE IV. Interaction profiles between target proteins and the tested phycobilins

PDB ID	Phycocyanobilin				Phycoerythrobilin				Phycourobilin				Phycoviolobilin			
	N_{HB}[a]	N_{ES}[b]	N_{HP}[c]	N_O[d]	N_{HB}	N_{ES}	N_{HP}	N_O	N_{HB}	N_{ES}	N_{HP}	N_O	N_{HB}	N_{ES}	N_{HP}	N_O
2NSD	3	–	13	–	6	–	6	–	5	–	6	–	5	–	5	–
2WGD	5	–	2	–	6	1	–	–	7	–	1	–	5	1	4	–
3COW	4	2	5	–	8	1	3	–	7	1	3	–	9	–	10	–
3PTY	6	1	3	–	7	–	4	–	4	–	4	–	7	1	4	–
4G3N	6	1	2	–	5	1	3	–	6	–	1	–	10	–	5	–
4NNI	9	–	1	–	9	–	1	–	4	1	3	–	5	2	7	–
5JZX	5	–	6	–	6	–	8	–	9	–	7	–	8	–	10	–
5KYG	11	–	1	–	6	–	–	–	6	2	–	–	8	–	5	–
5U94	4	1	5	1	6	–	4	1	5	–	3	–	6	1	4	–
5YIO	7	1	5	–	3	1	4	–	5	–	2	–	6	–	5	–
5ZX3	2	–	5	–	5	–	14	–	7	1	6	–	8	–	7	–

[a]Number of hydrogen bonds; [b]number of electrostatic interactions; [c]number of hydrophobic interactions; [d]number of other interactions

Interaction prediction using Discovery Studio Visualizer software revealed that numerous interactions occur between proteins and ligand molecules. Analysis of the interaction profile showed that, in addition to hydrogen bonds and hydrophobic interactions – the most common types of protein–ligand interactions – phycobilins also form electrostatic interactions with target proteins. Electrostatic interactions are not frequent among protein–ligand interfaces (Table IV). Many interfaces did not form electrostatic interactions, and the maximum number of electrostatic interactions in a complex was two (phycocyanobilin–3COW). For other interactions, there are two π–sulfur interactions in phycobilin complexes with the protein 5U94. Overall, the target protein's ability to support strong, multimodal interactions with phycobilins underscores its value as a central target for rational, structure-based anti-tubercular inhibitor design.

Fig. 1 clearly shows the types of noncovalent interactions and the interacting residues of the complex with the highest binding affinity (phycoviolobilin–2NSD; Vina score, –46.0 kJ mol^{-1}). Hydrogen bonding involves several residues, including Ile21, Ala22, Ser94 and Phe97, indicating a strong hydrogen bond network that enhances the stability of the complex. Ser94 acts as both a donor and an acceptor, simultaneously forming hydrogen bonds with phycoviolobilin. These arrangements may increase stability and play an important role in understanding the three-dimensional structure of protein–ligand complexes. Hydrogen bonding is essential for the specificity and strength of ligand binding, which is important in drug design.[22] A hydrophobic interactions is noted with Phe41, Ile95, Phe149 and Tyr158 (π–sigma and π–alkyl), indicating that these residues contribute to the binding affinity of compounds through nonpolar interactions.

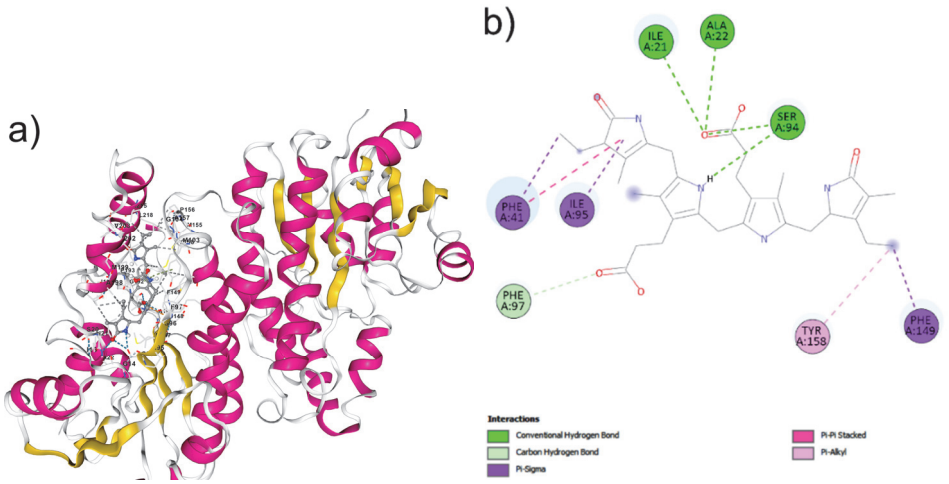

Fig. 1. The best docked complex of phycoviolobilin with 2NSD (Vina score, –46.0 kJ mol^{-1}); a) 3D structure showing the interactions between phycoviolobilin and protein 2NSD; b) 2D diagram of the docked complex.

Normal mode analysis (NMA) of docked complexes

Normal mode analysis (NMA) was performed to assess the intrinsic dynamics and stability of the top-ranked docked protein–phycobilin complexes using a Cα--based elastic network model implemented on the iMODS server. This approach enables characterization of collective motions, flexible distribution, and energetic features that govern the stability of protein–ligand assemblies. The NMA results for the best-docked complex of enoyl-acyl carrier protein reductase InhA (2NSD) with phycoviolobilin are shown in Fig. 2.

The deformability profile (Fig. 2b) shows several pronounced peaks, indicating flexible regions that may act as hinges or adaptive segments around the ligand-

-binding environment. These flexible regions are possibly essential for accommodating phycoviolobilin and allowing subtle conformational rearrangements upon binding. In contrast, the relatively low deformability observed in other regions suggests that the ligand is embedded in a mechanically stable framework, which may enhance binding specificity and reduce structural fluctuations. Such a balance between local flexibility and global rigidity is a hallmark of efficient ligand-binding proteins and has been widely described in elastic network studies of protein–ligand complexes.[23]

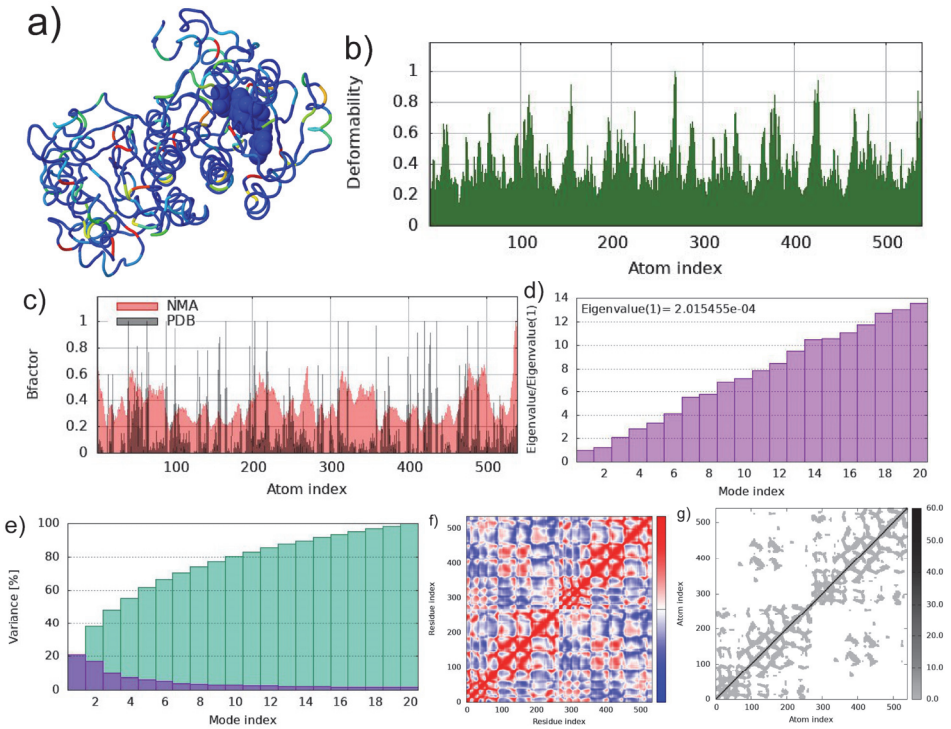

Fig. 2. Normal mode analysis (NMA) of enoyl-acyl carrier protein reductase InhA (2NSD) with the phycoviolobilin structure and its dynamic behavior: a) ligand bound in the binding pocket of the 2NSD protein. Blue: stable regions with low fluctuations; green and yellow: regions with moderate flexibility; orange and red: regions with high mobility; b) deformability plot showing the flexibility of each residue, with peaks indicating regions of high deformability; c) comparison of the normalized B-factors obtained from NMA (red) and from the crystal structure (black), indicating the reliability of the predicted atomic fluctuations; d) eigenvalue associated with each normal mode, reflecting the stiffness of the motion; lower eigenvalues indicate greater deformability; e) the variance associated with normal modes (purple – individual; green – cumulative variances); f) cross-correlation matrix of residue fluctuations, where red denotes correlated motions and blue denotes anti-correlated motions; g) elastic network model showing pairwise atomic connections; darker regions represent stronger interactions.

The comparison of NMA-derived B-factors with experimental B-factors from the crystal structure (Fig. 2c) shows a generally consistent trend throughout the protein sequence. Regions predicted to be flexible or rigid by the NMA model correspond well with experimentally observed atomic fluctuations. The overall consistency supports the conclusion that ligand binding modulates, rather than suppresses, intrinsic protein dynamics.

The eigenvalue spectrum (Fig. 2d) shows a very low eigenvalue for the first normal mode, corresponding to a soft, energetically accessible collective motion. Low-frequency modes are typically associated with global, functionally relevant motions rather than local unfolding events. This indicates that the 2NSD protein maintains its mechanical integrity after ligand binding, and suggests that the ligand is dynamically compatible with the protein's native fold, not destabilizing it.[8]

The variance distribution (Fig. 2e) shows that a small subset of low-frequency modes accounts for most of the protein's motion. Here, the cumulative variance (green bars) quickly saturates within the first 20 modes. This pattern confirms that the dynamics of 2NSD are governed by coordinated global transitions rather than fragmented or random local fluctuations. That behavior characterizes mechanically stable protein–ligand complexes.[24]

The covariance map (Fig. 2f) shows the prevalence of positively correlated motions (red regions) among residue pairs. These large locks of correlation zones along the diagonal indicate coherent domain movements and efficient intramolecular communication. The lack of extensive anti-correlated motions (blue regions) suggests that the bonded ligand does not introduce dynamic strain or conflicting motions between different protein segments, thereby preserving functional coordination. Similar correlation patterns have been associated with stable ligand-bound states in previous NMA studies.[25,26]

The underlying elastic network model shows a dense, well-integrated network of harmonic springs. The high frequency of firmer connections (darker gray dots) throughout the atom-index matrix indicates strong mechanical coupling. The ligand-binding site is nested within this stable, elastic framework and ligand binding appears to strengthen the mechanical integrity of 2NSD rather than disrupt it.

Overall, the NMA results indicate that phycoviolobilin binding stabilizes the global architecture of 2NSD while preserving essential flexibility and long-range correlated motions. The ligand appears to act as a dynamic modulator, reinforcing cooperative motions and maintaining access to low-energy conformational states. These properties are likely crucial for the biological function of the complex, particularly in processes requiring efficient energy transfer or signal propagation.

NMA analysis of other top-docked complexes with phycobilins shows similar results. The atomic conformation pattern was nearly identical for all complexes and remained stable after docking with the phycobilin molecules. These results are provided in the Supplementary material to this paper.

While NMA correctly identifies collective motions and global stability of the docked complexes, it is important to acknowledge its limitations as a first-order harmonic approximation around a single static structure. This analysis does not account for explicit solvent effects, thermal fluctuations, or long-term time-dependent conformational sampling typically captured by molecular dynamics (MD) simulations. Therefore, the NMA results presented here serve as an exploratory validation of complex stability, and further MD studies are warranted.

Pharmacokinetic and toxicity profiles

ADMET plays a crucial role in preclinical testing of drug candidates by enabling assessment of pharmacokinetic and toxicity profiles and facilitating the identification of lead compounds.[27] Therefore, an *in silico* pharmacological and toxicological study was conducted on the phycobilins using the Deep-PK online tool (Table V).

TABLE V. ADMET analysis of the phycobilins obtained with Deep-PK tool; NB – non-bioavailable; NP – non-penetrable; NI – non-inhibitor; I – inhibitor; NS – non-substrate

Absorption category	Phycocyanobilin	Phycoerythrobilin	Phycourobilin	Phycoviolobilin
Caco-2 permeability	–5.66	–5.86	–5.85	–5.72
Human oral bioavailability 20 %	NB	NB	NB	NB
Human intestinal absorption	Absorbed	Absorbed	Absorbed	Absorbed
Skin permeability	Low	Normal	Normal	Low
Distribution category				
Blood–brain barrier	NP	NP	NP	NP
Plasma protein binding	26.13	53.05	52.96	20.64
Fraction unbound (human)	1.39	1.42	1.20	1.41
Steady-state volume of distribution	0.56	0.51	0.50	0.61
Metabolism category				
CYP 1A2 Inhibitor	NI	NI	Inhibitor	NI
CYP 2C19 Inhibitor	NI	NI	NI	NI
CYP 2C9 Inhibitor	NI	NI	NI	NI
CYP 2D6 Inhibitor	NI	NI	NI	NI
CYP 3A4 Inhibitor	NI	NI	NI	NI
CYP 1A2 Substrate	NS	NS	NS	NS
CYP 2C19 Substrate	NS	NS	NS	NS
CYP 2C9, CYP 2D6, CYP 3A4 Substrate	NS	NS	NS	NS
Excretion category				
Clearance	3.86	2.72	3.97	3.41

TABLE V. Continued

Absorption category	Phycocyanobilin	Phycoerythrobilin	Phycourobilin	Phycoviolobilin
Excretion category				
Organic cation transporter 2	NI	NI	NI	NI
Half-life of drug, h	< 3	< 3	< 3	< 3
Toxicity category				
AMES mutagenesis	Toxic	Toxic	Toxic	Toxic
Avian	Safe	Safe	Safe	Safe
Bee	Safe	Safe	Safe	Safe
Biodegradation	Safe	Safe	Safe	Safe
Liver injury II	Safe	Safe	Safe	Safe
Eye corrosion	Safe	Safe	Safe	Safe
Eye irritation	Safe	Safe	Safe	Safe
Maximum tolerated dose	0.07	0.03	0.10	–0.01
HERG blocker	Safe	Safe	Safe	Safe
Skin sensitization	Toxic	Toxic	Toxic	Toxic

Caco-2 cells are commonly used as an *in vitro* model to predict human oral drug absorption.[18] The prediction indicated low Caco-2 permeability for all phycobilins. Additionally, it was estimated that all phycobilins would be orally non-bioavailable in humans but are predicted to be absorbed in the human intestine. Regarding skin permeability, phycocyanobilin and phycoviolobilin were predicted to have low skin permeability, while phycoerythrobilin and phycourobilin were predicted to have normal skin permeability. It is estimated that all phycobilins lack the ability to cross the blood-brain barrier efficiently and are predicted to have an appropriate plasma protein binding value. This is an important therapeutic index related to the amount of free drug in the body. A moderate steady-state volume of distribution was predicted for all phycobilins, indicating a balanced distribution between plasma and tissue. All phycobilins are estimated to be non-inhibitors of cytochrome P450 isoforms, while phycourobilin is predicted to inhibit CYP1A2, an important detoxification enzyme primarily located in the liver. The predominance of non-inhibitor (NI) annotations in the metabolism category suggests that the phycobilins studied are unlikely to inhibit major CYP isoforms, reducing the risk of pharmacokinetic drug–drug interactions.[28] This is particularly important in tuberculosis treatment, where the concurrent use of multiple drugs is common.[4,29]

In terms of excretion, all phycobilins showed a similar clearance rate. Clearance is the rate at which a compound is eliminated through the kidneys and provides an estimate of how long the drug remains in systemic circulation. A higher clearance value indicates that the compound is eliminated from the body more rapidly. The elimination half-life of all phycobilins was short, less than 3 h, sug-

gesting that multiple daily doses may be necessary for therapeutic efficacy. Toxicity prediction showed a generally favorable profile across multiple endpoints, including hERG blockage, liver injury and ocular irritation, with all four bilins predicted to be safe in these areas. However, all compounds were predicted to be AMES--positive (toxic), indicating potential mutagenicity liability and were consistently flagged as toxic for skin sensitization, suggesting possible allergenic potential.

The identification of potential mutagenicity (AMES-positive) and skin sensitization for all four phycobilins is a common challenge in early-stage natural product discovery. These liabilities are frequently observed in natural scaffolds with extended conjugated systems and are typically addressed through systematic lead optimization to separate therapeutic activity from toxicophore signals. Compared to typical early-stage natural product leads, phycobilins have a manageable safety profile that warrants further experimental clarification rather than immediate exclusion.

Given the predicted AMES-positive results, further verification using additional *in silico* toxicity models and experimental *in vitro* AMES assays is required.[30] Structural optimization strategies could be considered to reduce the predicted mutagenic liability during lead optimization. Among the series, the maximum tolerated dose parameter suggested relatively higher tolerance for phycourobilin and lower tolerance for phycoviolobilin, although these differences do not outweigh the consistent AMES and sensitization alerts, which represent critical safety liabilities in early-stage drug development.[31]

Prediction of anti-tuberculosis sensitivity

The anti-tuberculosis potential of phycobilins was evaluated using the mycoCSM web server and compared with the reference antibiotics isoniazid and rifampicin, based on predicted minimum inhibitory concentration (*MIC*), caseum penetration (Caseum FU) and maximum recommended tolerated dose (*MRTD*) (Table VI). The mycoCSM platform uses graph-based signatures to model compound–pathogen interactions and pharmacological properties relevant to tuberculosis drug discovery.[11]

TABLE VI. Anti-tuberculosis sensitivity of phycobilins and antibiotics predicted by mycoCSM; *MIC* – minimum inhibitory concentration; MRTD – maximum recommended tolerated dose

Drug	log (*MIC* / μmol)	Caseum FU, %	log (*MRTD* / mg kg^{-1} day^{-1})
Phycobilins			
Phycocyanobilin	–4.812	3.0	0.726
Phycoerythrobilin	–4.777	5.577	0.656
Phycourobilin	–4.724	3.912	0.524
Phycoviolobilin	–4.991	2.604	0.711
Antibiotics			
Isoniazid	–4.942	67.2	1.166
Rifampicin	–5.809	8.08	0.116

Phycobilins have high molecular weights and extensive hydrogen-bonding capacities, which significantly affect their TB drug-likeness. Although these properties may restrict passive diffusion, they are similar to those of larger macrocyclic anti-tubercular drugs such as rifampicin. The predicted limited penetration into caseous lesions is likely due to these physicochemical parameters (large polar surface area and multiple hydrogen-bond donors), suggesting that future structural modifications should aim to increase lipophilicity and reduce polar surface area to improve intracellular penetration and efficacy in TB-infected tissues.

All four phycobilins showed favorable predicted log (*MIC* / μmol) values, with phycoviolobilin (−4.991) having the lowest *MIC* among the tested bilins, followed by phycocyanobilin (−4.812), phycoerythrobilin (−4.777) and phycourobilin (−4.724). The predicted log *MIC* of phycoviolobilin was comparable to isoniazid (−4.942), though still higher than rifampicin (−5.809), which remains the most potent compound in this comparison. These results suggest that phycobilins, particularly phycoviolobilin, may have moderate to promising anti-mycobacterial activity, supporting their potential as nonclassical anti-tubercular scaffolds, consistent with previous computational TB screening studies.

Caseum FU, a critical parameter for assessing drug accessibility to necrotic TB lesions, was substantially lower for phycobilins (2.6–5.6 %) than for isoniazid (67.2 %) and rifampicin (8.08 %). Limited caseum penetration has been associated with reduced sterilizing activity against *M. tuberculosis* persisting in necrotic granulomas.[32] Among the phycobilins, phycoerythrobilin had the highest caseum FU (5.577 %), indicating relatively better lesion penetration within this group, although still lower than that of the first-line drugs. Given the limited penetration into caseous lesions, future research may benefit from developing nano-based formulations or structural optimization strategies to improve drug distribution within tuberculosis lesions.[33,34]

The predicted log (*MRTD* / mg kg^{-1} day^{-1}) values for phycobilins ranged from 0.524 to 0.726, which are lower than that of isoniazid (1.166) but notably higher than that of rifampicin (0.116). This intermediate *MRTD* profile suggests a moderate tolerability margin, consistent with natural product-derived scaffolds and supports the feasibility of further optimization.[35] Slightly higher *MRTD* values for phycocyanobilin and phycoviolobilin may indicate a comparatively more favorable safety window within this series, consistent with the established relationship between tolerable dose limits and therapeutic safety margins in early-stage drug development.[31,36]

CONCLUSIONS

This study presents a comprehensive and internally consistent computational framework that identifies phycobilins as a promising and underexplored class of natural product scaffolds for anti-tubercular drug discovery. Through systematic

multi-target docking against a broad panel of essential *M. tuberculosis* proteins, phycobilins showed strong and reproducible binding affinities that not only exceeded those of isoniazid across several targets but also approached the interaction strength of rifampicin. This convergence of high-affinity binding across mechanistically diverse enzymes strongly supports a true polypharmacological mode of action, a feature increasingly recognized as critical for overcoming resistance in tuberculosis therapy.

Beyond static affinity predictions, dynamic analyses provided decisive mechanistic insight. Normal mode analysis revealed that phycobilin binding induces ligand-driven stabilization of protein architectures while preserving low-frequency collective motions associated with enzymatic function. This dynamic compatibility, exemplified by the phycoviolobilin–InhA complex, underscores the ability of these ligands to integrate into functional protein networks without imposing destabilizing conformational strain, an essential attribute for sustained inhibitory activity.

Although pharmacokinetic and toxicity predictions indicated limitations in oral bioavailability, lesion penetration, and potential genotoxic and sensitization liabilities, these findings should be interpreted in the context of early-stage lead identification. Importantly, none of these liabilities undermine the central observation that phycobilins have a highly favorable binding and dynamic interaction profile. Instead, they define a clear and rational optimization path focused on improving exposure and safety while preserving intrinsic multi-target potency.

Collectively, the strength and coherence of the computational evidence presented here elevate phycobilins from passive bioactive pigments to strategically valuable lead-like molecules. Their demonstrated capacity for multi-target engagement, dynamic stabilization and competitive inhibitory potential justifies their prioritization for structure-guided optimization and experimental validation, with the long-term prospect of contributing to the development of next-generation anti-tubercular therapeutics. Given the reported limitations in penetration into caseous lesions, future research should explore nano-formulation approaches or rational chemical modifications to improve drug delivery and accumulation at the infection site.

SUPPLEMENTARY MATERIAL

Additional data and information are available electronically at the pages of journal website: https://www.shd-pub.org.rs/index.php/JSCS/article/view/13744, or from the corresponding author on request.

Acknowledgement. This research has been financially supported by the Ministry of Science, Technological Development and Innovation of Republic of Serbia (Contract No: 451-03-136/2025-03/200026 and 451-03-136/2025-03/200168).

ИЗВОД

IN SILICO ЕВАЛУАЦИЈА ФИКОБИЛИНА КАО ВИШЕЦИЉНИХ АНТИТУБЕРКУЛАРНИХ СКЕЛА: МОЛЕКУЛАРНИ ДОКИНГ, ДИНАМИЧКА СТАБИЛНОСТ, ADMET И АНАЛИЗА ОСЕТЉИВОСТИ НА МИКОБАКТЕРИЈЕ

АМЕЛА К. ЛЕПОЈЕВИЋ[1], МИРОСЛАВ М. ЈЕВТИЋ[1], МАРИО В. ЗЛАТОВИЋ[2] и СРЂАН Ђ. СТОЈАНОВИЋ[3]

[1]Специјална болница за плућне болести и туберкулозу „Озрен", Сокобања, [2]Универзитет у Београду, Хемијски факултет, катедра за органску хемију, Београд и [3]Универзитет у Београду, Институт за хемију, технологију и металургију, Центар за хемију, Институт од националног значаја за Републику Србију, Београд

Туберкулоза и даље представља велики глобални здравствени терет, што наглашава хитну потребу за новим терапијским третманом са побољшаном ефикасношћу и вишеструким дејством. У овој студији примењена је интегрисана *in silico* стратегија за испитивање антитуберкулозног потенцијала четири природно присутна фикобилина – фикоцијанобилина, фикоеритрибилина, фикоуробилина и фиковиолобилина – против панела есенцијалних протеинских мета *Mycobacterium tuberculosis* укључених у биосинтезу ћелијског зида, метаболизам нуклеинских киселина, производњу енергије и функцију рибозома. Анализе молекулског докинга показале су конзистентно јак афинитет везивања фикобилина према више циљних протеина, често премашујући афинитет везивања изониазида и приближавајући се перформансама везивања рифампицина, што указује на изражену способност интеракције са више циљева. Анализа нековалентних интеракција указала је на стабилне и разноврсне интеракционе мреже којима доминирају водоничне везе и хидрофобни контакти. Анализа нормалних модова потврдила је да везивање фикобилина очувава својствену динамику протеина, уз истовремено индуковану, лигандима посредовану стабилизацију протеинско–лигандних комплекса, нарочито у систему фиковиолобилин–ИнхА. Предикције фармакокинетике и токсичности указале су на умерена дистрибуциона својства и генерално повољне безбедносне профиле, иако су идентификовани потенцијални сигнали мутагености и сензибилизације коже. Додатно, предвиђања заснована на mycoCSM указале су на антимикобактеријску активност у микромоларном опсегу са ограниченим продирањем у казеозне лезије. Заједно посматрано, ови резултати подржавају фикобилине као обећавајуће природне скеле за откривање лекова против туберкулозе, што захтева даљу оптимизацију и експерименталну валидацију.

(Примљено 24. јануара, ревидирано 2. фебруара, прихваћено 5. фебруара 2025)

REFERENCES

1. B. D. Daniel, C. Padmapriyadarsini, S. Giri, P. S. Winarni, *BMJ* **390** (2025) 2024 (https://doi.org/10.1136/bmj-2024-080075)
2. M. Kufa, V. Finger, O. Kovar, O. Soukup, C. Torruellas, J. Roh, J. Korabecny, *Acta Pharm. Sin., B* **15** (2025) 1311 (https://doi.org/10.1016/j.apsb.2025.01.023)
3. R. R. Patel, Vidyasagar, S. K. Singh, M. Singh, *Microb. Pathog.* **203** (2025) 107515 (https://doi.org/10.1016/j.micpath.2025.107515)
4. A. Zumla, P. Nahid, S. T. Cole, *Nat. Rev. Drug Discov.* **12** (2013) 388 (https://doi.org/10.1038/nrd4001)
5. N. Rao, V. D. Jathar, *Pharm. Chem. J.* **59** (2025) 512 (https://doi.org/10.1007/s11094-025-03422-z)
6. C. García-Gómez, D. E. Aguirre-Cavazos, A. Chávez-Montes, J. M. Ballesteros-Torres, A. A. Orozco-Flores, R. Reyna-Martínez, Á. D. Torres-Hernández, G. M. González-Meza,

S. L. Castillo-Hernández, M. A. Gloria-Garza, M. Kačániová, M. Ireneusz-Kluz, J. H. Elizondo-Luevano, *Mar. Drugs* **23** (2025) 201 (https://doi.org/10.3390/md23050201)
7. I. Kolossváry, *JACS Au* **4** (2024) 1303 (https://doi.org/10.1021/jacsau.4c00109)
8. J. R. López -Blanco, J. I. Aliaga, E. S. Quintana-Orti, P. Chacón, *Nucleic Acids Res*. **42** (2014) W271-W276 (https://doi.org/10.1093/nar/gku339)
9. M. S. Roomi, G. Culletta, L. Longo, W. Filgueira de Azevedo, U. Perricone, M. Tutone, *Pharmaceuticals* **18** (2025) 1777 (https://doi.org/10.3390/ph18121777)
10. R. Ancuceanu, B. E. Lascu, D. Drăgănescu, M. Dinu, *Pharmaceutics* **17** (2025) 1002 (https://doi.org/10.3390/pharmaceutics17081002)
11. D. E. V. Pires, D. B. Ascher, *J. Chem. Inf. Model.* **60** (2020) 3450 (https://doi.org/10.1021/acs.jcim.0c00362)
12. S. Kim, J. Chen, T. Cheng, A. Gindulyte, J. He, S. He, Q. Li, B. A. Shoemaker, P. A. Thiessen, B. Yu, L. Zaslavsky, J. Zhang, E. E. Bolton, *Nucleic Acids Res.* **51** (2023) D1373 (https://doi.org/10.1093/nar/gkac956)
13. H. M. Berman, J. Westbrook, Z. Feng, G. Gilliland, T. N. Bhat, H. Weissig, I. N. Shindyalov, P. E. Bourne, *Nucleic Acids Res*. **28** (2000) 235 (https://doi.org/10.1093/nar/28.1.235)
14. Y. Liu, X. Yang, J. Gan, S. Chen, Z. X. Xiao, Y. Cao, *Nucleic Acids Res*. **50** (2022) W159-W164 (https://doi.org/10.1093/nar/gkac394)
15. J. Eberhardt, D. Santos-Martins, A. F. Tillack, S. Forli, *J. Chem. Inf. Model.* **61** (2021) 3891 (https://doi.org/10.1021/acs.jcim.1c00203)
16. D.S. Biovia, *Discovery Studio Visualizer*, San Diego, CA, 2025
17. X. Q. Yao, L. Skjaerven, B. J. Grant, *J. Phys. Chem., B* **120** (2016) 8276 (https://doi.org/10.1021/acs.jpcb.6b01991)
18. Y. Myung, A. G. C. de Sá, D. B. Ascher, *Nucleic Acids Res.* **52** (2024) W469 (https://doi.org/10.1093/nar/gkae254)
19. B. P. Brown, *Proc. Natl. Acad. Sci. USA* **122** (2025) e2508998122 (https://doi.org/10.1073/pnas.2508998122)
20. C. Hetényi, D. van der Spoel, *Prot. Sci*. **11** (2002) 1729 (https://doi.org/10.1110/ps.0202302)
21. S. Y. Ugurlu, *J. Comput. Aided Mol. Des*. **39** (2025) 48 (https://doi.org/10.1007/s10822-025-00629-w)
22. A. S. Mahadevi, G. N. Sastry, *Chem. Rev*. **116** (2016) 2775 (https://doi.org/10.1021/cr500344e)
23. L. W. Yang, E. Eyal, C. Chennubhotla, J. Jee, A. M. Gronenborn, I. Bahar, *Structure* **15** (2007) 741 (https://doi.org/10.1016/j.str.2007.04.014)
24. T. Ichiye, M. Karplus, *Proteins* **11** (1991) 205 (https://doi.org/10.1002/prot.340110305)
25. F. Tama, Y. H. Sanejouand, *Protein Eng.* **14** (2001) 1 (https://doi.org/10.1093/protein/14.1.1)
26. I. Bahar, T. R. Lezon, L. W. Yang, E. Eyal, *Ann. Rev. Biophys.* **39** (2010) 23 (https://doi.org/10.1146/annurev.biophys.093008.131258)
27. H. van de Waterbeemd, E. Gifford, *Nat. Rev. Drug Discov.* **2** (2003) 192 (https://doi.org/10.1038/nrd1032)
28. U. M. Zanger, M. Schwab, *Pharmacol. Ther*. **138** (2013) 103 (https://doi.org/10.1016/j.pharmthera.2012.12.007)
29. World Health Organization, *WHO consolidated guidelines on tuberculosis: Module 4 – Treatment*, World Health Organization, Geneva, 2023 (https://www.who.int/publications/i/item/9789240107243)

30. R. Benigni, C. Bossa, *Chem. Rev.* **111** (2011) 2507 (https://doi.org/10.1021/cr100222q)
31. P. Y. Muller, M. N. Milton, *Regul. Toxicol. Pharmacol.* **63** (2012) 388 (https://doi.org/10.1016/j.yrtph.2012.05.003)
32. B. Prideaux, L. E. Via, M. D. Zimmerman, S. Eum, J. Sarathy, P. O'Brien, C. Chen, F. Kaya, D. M. Weiner, P. Y. Chen, T. Song, M. Lee, T. S. Shim, J. S. Cho, W. Kim, S. N. Cho, K. N. Olivier, C. E. Barry, III, V. Dartois, *Nat. Med.* **21** (2015) 1223 (https://doi.org/10.1038/nm.3937)
33. T. Bourguignon, JA. Godinez-Leon, R. Gref, *Pharmaceutics* **15** (2023) 393 (https://doi.org/10.3390/pharmaceutics15020393)
34. A. Sharma, V. Sharma, S. Sharma, S. Sharma, M. Sharma, I. Sivanesan, *Pharmaceutics* **17** (2025) 1459 (https://doi.org/10.3390/pharmaceutics17111459)
35. V. Dartois, *Nat. Rev. Microbiol.* **12** (2014) 159 (https://doi.org/10.1038/nrmicro3200)
36. R. Zhang, H. Wen, Z. Lin, B. Li, X. Zhou, *Toxics* **13** (2025) 525 (https://doi.org/10.3390/toxics13070525).

Journal of the Serbian Chemical Society
JSCS@tmf.bg.ac.rs • www.shd.org.rs/JSCS
J. Serb. Chem. Soc. 91 (4) S127–S130 (2026) *Supplementary material*

SUPPLEMENTARY MATERIAL TO

In silico evaluation of phycobilins as multi-target anti-tubercular scaffolds: Molecular docking, dynamic stability, ADMET and mycobacterial sensitivity analysis

AMELA K. LEPOJEVIĆ[1], MIROSLAV M. JEVTIĆ[1], MARIO V. ZLATOVIĆ[2] and SRĐAN Đ. STOJANOVIĆ[3]*

[1]*Special Hospital for Pulmonary Diseases and Tuberculosis "Ozren", Sokobanja, Serbia,* [2]*University of Belgrade, Faculty of Chemistry, Department of Organic Chemistry, Belgrade, Serbia, and* [3]*University of Belgrade, Institute of Chemistry, Technology and Metallurgy – National institute of the Republic of Serbia, Department of Chemistry, Belgrade, Serbia*

J. Serb. Chem. Soc. 91 (4) (2026) 353–370

ANALYTICAL AND SPECTRAL DATA

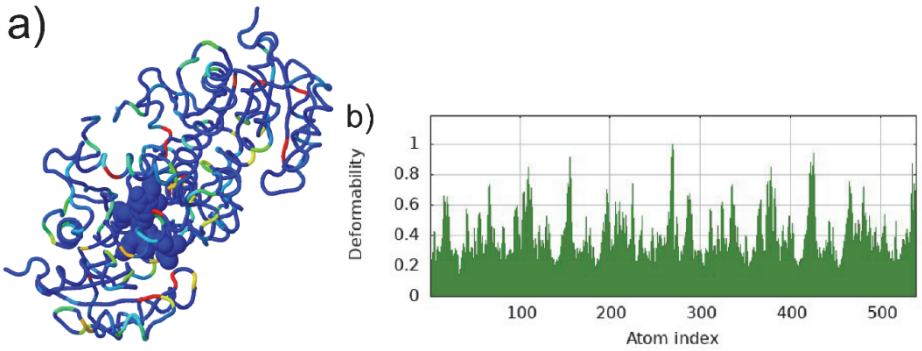

* Corresponding author. E-mail: srdjan.stojanovic@ihtm.bg.ac.rs

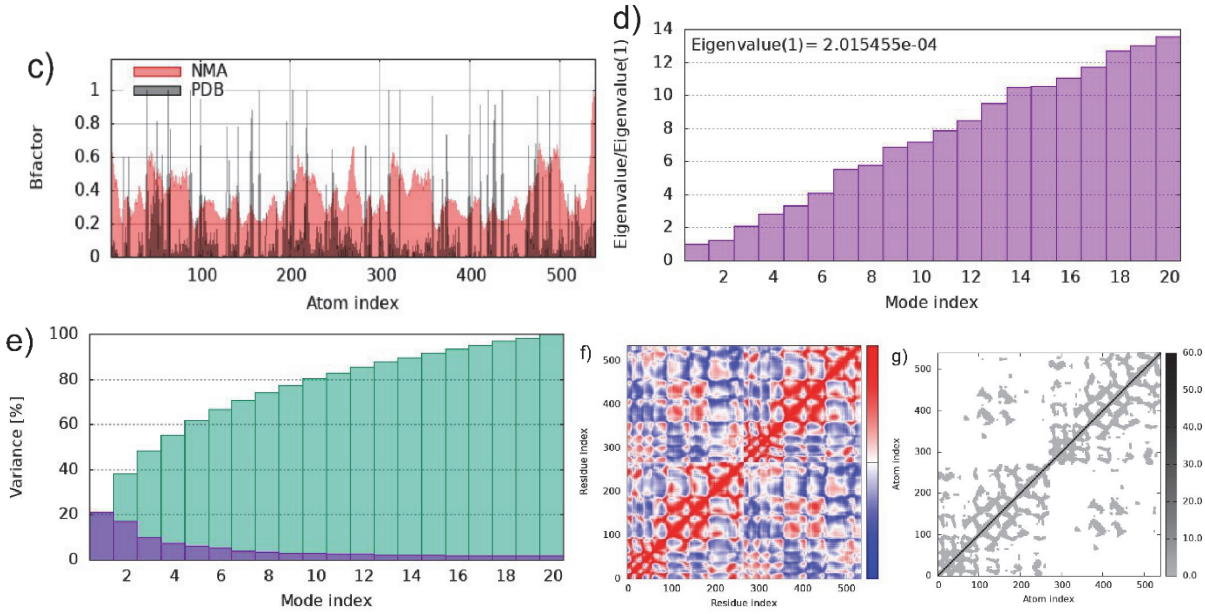

Fig. 1-S. Normal mode analysis (NMA) of enoyl-acyl carrier protein reductase InhA (2NSD) with the phycocyanobilin structure and its dynamic behavior: a) Ligand bound in the binding pocket of the 2NSD protein. Blue: stable regions with low fluctuations; green and yellow: regions with moderate flexibility; orange and red: regions with high mobility; b) Deformability plot showing the flexibility of each residue, with peaks indicating regions of high deformability; c) Comparison of the normalized B-factors obtained from NMA (red) and from the crystal structure (black), indicating the reliability of the predicted atomic fluctuations; d) Eigenvalue associated with each normal mode, reflecting the stiffness of the motion; lower eigenvalues indicate greater deformability; e) The variance associated with normal modes (purple – individual; green – cumulative variances); f) Cross-correlation matrix of residue fluctuations, where red denotes correlated motions and blue denotes anti-correlated motions; g) Elastic network model showing pairwise atomic connections; darker regions represent stronger interactions.

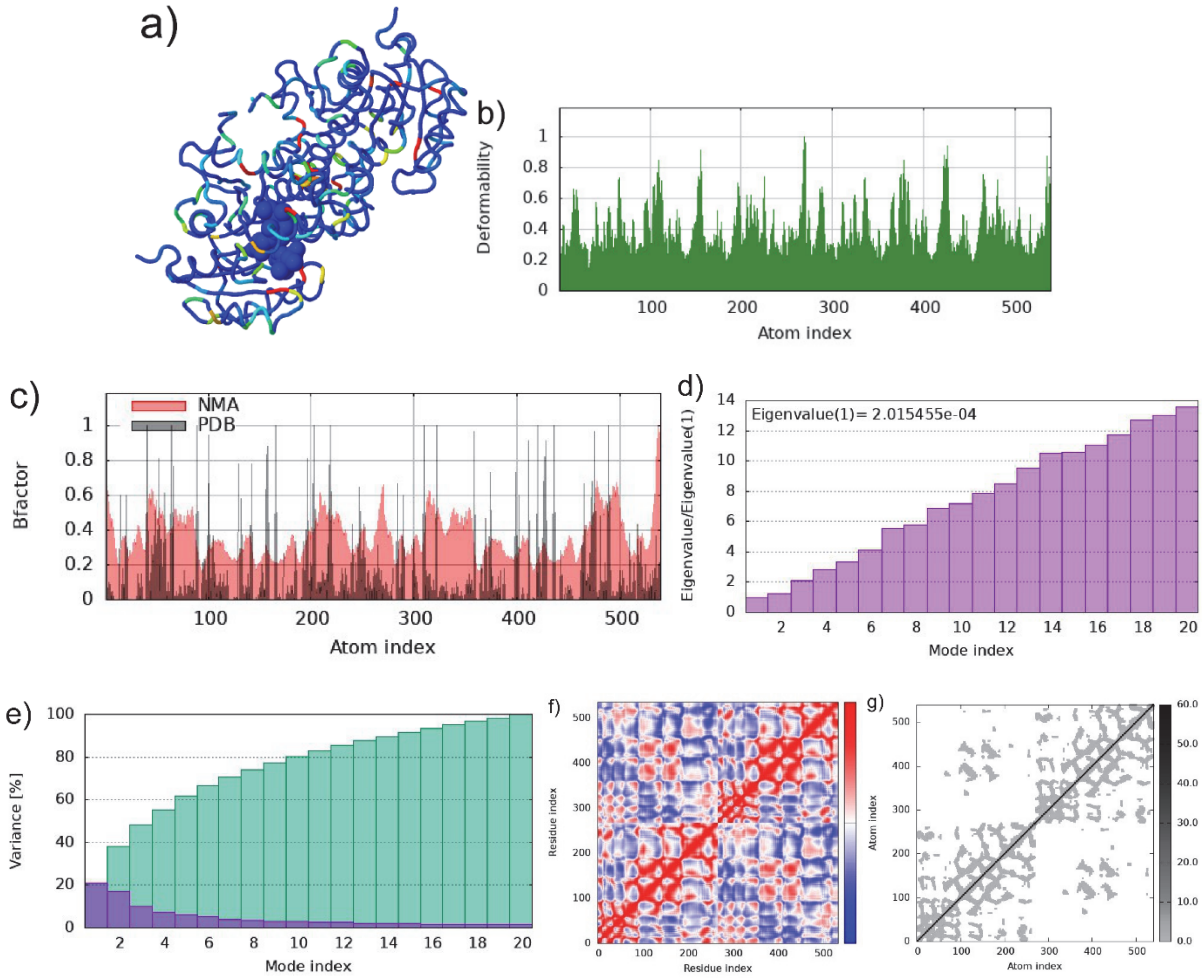

Fig. 2-S. Normal mode analysis (NMA) of enoyl-acyl carrier protein reductase InhA (2NSD) with the phycoerythrobilin structure and its dynamic behavior: a) Ligand bound in the binding pocket of the 2NSD protein. Blue: stable regions with low fluctuations; green and yellow: regions with moderate flexibility; orange and red: regions with high mobility; b) Deformability plot showing the flexibility of each residue, with peaks indicating regions of high deformability; c) Comparison of the normalized B-factors obtained from NMA (red) and from the crystal structure (black), indicating the reliability of the predicted atomic fluctuations; d) Eigenvalue associated with each normal mode, reflecting the stiffness of the motion; lower eigenvalues indicate greater deformability; e) The variance associated with normal modes (purple – individual; green – cumulative variances); f) Cross-correlation matrix of residue fluctuations, where red denotes correlated motions and blue denotes anti-correlated motions; g) Elastic network model showing pairwise atomic connections; darker regions represent stronger interactions.

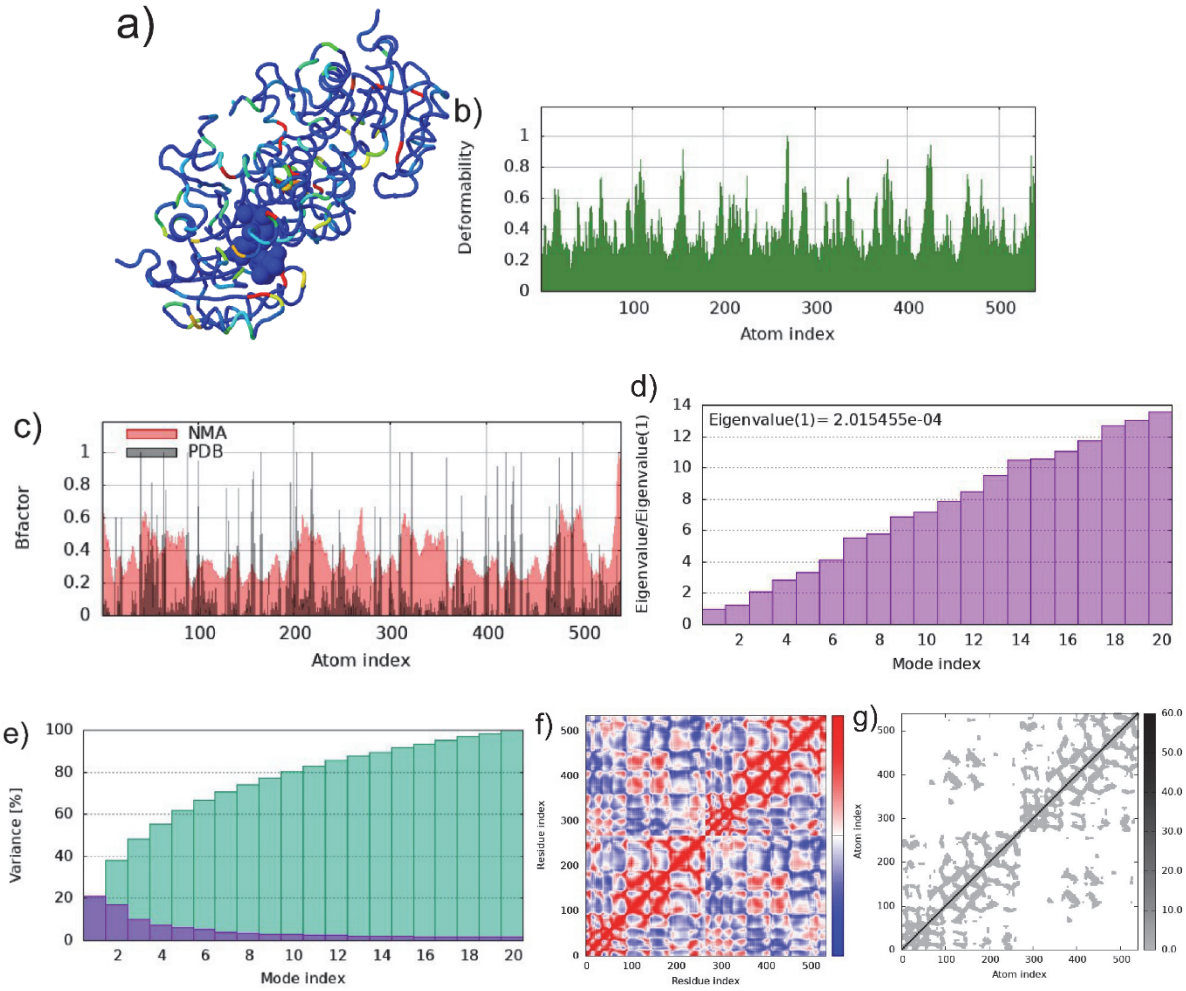

Fig. 3-S. Normal mode analysis (NMA) of enoyl-acyl carrier protein reductase InhA (2NSD) with the phycourobilin structure and its dynamic behavior: a) Ligand bound in the binding pocket of the 2NSD protein. Blue: stable regions with low fluctuations; green and yellow: regions with moderate flexibility; orange and red: regions with high mobility; b) Deformability plot showing the flexibility of each residue, with peaks indicating regions of high deformability; c) Comparison of the normalized B-factors obtained from NMA (red) and from the crystal structure (black), indicating the reliability of the predicted atomic fluctuations; d) Eigenvalue associated with each normal mode, reflecting the stiffness of the motion; lower eigenvalues indicate greater deformability; e) The variance associated with normal modes (purple – individual; green – cumulative variances); f) Cross-correlation matrix of residue fluctuations, where red denotes correlated motions and blue denotes anti-correlated motions; g) Elastic network model showing pairwise atomic connections; darker regions represent stronger interactions.

Journal of the Serbian Chemical Society
JSCS-info@shd.org.rs • www.shd.org.rs/JSCS
J. Serb. Chem. Soc. 91 (4) 371–380 (2026)
JSCS–5497
Original scientific paper
Published 1 May, 2026

DFT-guided prediction of singlet fission chromophores for high-efficiency organic solar cells

RIYADH R. AL-ARAJI*

Wasit University, College of Education for Pure Sciences, Wasit, Iraq

(Received 3 August, revised 20 November 2025, accepted 27 January 2026)

Abstract: Theoretical design and DFT calculations were performed to find new SF chromophores to be used in high efficiency organic solar cells. These included 6 new compounds containing boron, nitrogen, selenium, TIPS and phenyl groups. All of these molecules demonstrated near-planar geometries with extended π-conjugation and had HOMO–LUMO gaps between 3.04 and 3.32 eV. The excitation energies for the singlet and triplet states were in the ranges of 2.11–2.25 eV and 1.00–1.10 eV, leading to singlet–triplet energy gaps ranging from 1.11––1.16 eV. All compounds met the critical energetic requirement for efficient singlet fission whereby $E_{S1} > 2E_{T1}$ for all chromophores. Some selected derivatives, such as N1 and N4 were found to have ΔE_{ST} values of 1.15 and 1.14 eV, respectively, which are equal to or greater than the benchmark value of pentacene which is 1.02 eV and diketopyrrolopyrrole which is 1.18 eV. Moreover, the new chromophores are expected to have greater absorption and thermal stability spectrum making them better suited for next-generation organic solar cells. This study highlights the promise of rational heteroatom and functional group design for SF-active materials with advanced optoelectronic and device-engineering properties.

Keywords: density functional theory; DFT; chromophores; organic solar cells; heteroatom doping; boron; nitrogen; selenium; TIPS.

INTRODUCTION

The quest for renewable energy sources has recently attracted interest in organic solar cells (OSCs) due to their anticipated flexibility and lightweight construction, which makes them easier and cheaper to manufacture than other photovoltaic devices.[1–4] Even with advancements in OSC technology, their power conversion efficiencies (*PCE*) still significantly trail behind those of inorganic solar cells due to the fundamental challenges associated with exciton diffusion and charge carrier generation.[5–8] One of the most game-changing approaches to these

* Corresponding author. E-mail: rmohammed@uowasit.edu.iq
https://doi.org/10.2298/JSC250803004A

limitations is the process of singlet fission (SF). This process can double photocurrent and PCE beyond the theoretical Shockley Queisser limit for single-junction solar cells by splitting a high-energy singlet exciton into two lower-energy triplet excitons.[9–13] SF has been a rich area of study in materials chemistry, photo-physics and device engineering since its initial observation in anthracene crystals in the 1960s.[14–16] Research has shown that SF efficiency is closely dependent on the molecular electronic structure and intermolecular packing, as well as the energy alignment between the singlet and triplet states.[17–19] A chromophore that undergoes SF should have a singlet energy (E_{S1}) slightly greater than $2E_{T1}$, in addition to good orbital overlap and crystal shape to allow for fast triplet fission and movement.[20–24] Recent advances in computational quantum chemistry, particularly the application of density functional theory (DFT), have enabled the theoretical prediction, screening and optimization of novel singlet fission (SF)–active materials prior to their computational synthesis. DFT methods provide reasonable accuracy along with efficiency and thus enable the rational design of π-conjugated organic molecules to the d and SF chromophores for incorporation into OSCs.[25–26] Of particular significance is the fact that now, computational descriptors such as frontier orbital gaps, singlet–triplet energy splitting (ΔE_{ST}) and even intersystem crossing rates are routinely calculated and benchmarked against designed data to expedite discovery.[27] In the past decade alone, there has been a surge in theoretical and empirical research focused on the development of acene and heteroacene SF materials, diketopyrrolopyrroles and perylenediimides, as well as other π-extended scaffolds.[28] Rational core modification through heteroatom doping, functional group engineering and controlled molecular packing has provided diverse materials with greater photostability, faster SF rates and even enhanced OSC compatibility.[29] Direct measurement and utilization of triplet yields made possible by ultrafast spectroscopic techniques and advanced device architectures have confirmed computational estimates and further enabled iterative molecular design. During the past three years, studies have emphasized the increasing synergy between high-throughput DFT screening and machine learning, which has enabled the accelerated prediction of SF chromophores with unprecedented scope and precision.[30] Significant advancements in donor–acceptor copolymers, non-fullerene acceptors and hybrid organic–inorganic interfaces utilizing SF to enhance OSC efficiencies beyond 20 % have been published in Elsevier-indexed journals.[31] These advances have been aided by multiscale modeling approaches, including TD-DFT, GW-BSE methods and excited-state dynamics simulations, which provide atomic-level insights into the structure–property relationships governing SF and triplet harvesting. Despite these advancements, critical issues remain. Many proposed SF materials are hindered by challenges including synthetic inaccessibility, instability or poor integration into device architectures. The chromophore energy levels, solid-state morphology and interface design still require precise iterative computational and

design workflows. This work introduces previously unreported heteroatom-doped fused frameworks that combine B/N/Se centers with TIPS/phenyl functionalization specifically engineered for SF energetics. To the best of our knowledge, these structures have not been explored as SF chromophores, and the computed ΔE_{ST} values (1.11–1.16 eV) place them on par with or beyond classical benchmarks.

COMPUTATIONAL METHODS

Computational details

All quantum chemistry calculations were executed using the Gaussian 16 software suite. The chromophores of interest were geometrically optimized at the DFT level with the B3LYP functional and the 6-31G (d, p) basis set. As part of the optimization process, frequency analyses were performed to verify that all structures in Fig. 1 had no imaginary frequencies and corresponded to true minima. The vertical excitation energies were extracted using time-dependent DFT for the first singlet and triplet states at the B3LYP/6-311+G (2d, p) level on the previously optimized geometries. Unless specified otherwise, all calculations were performed under gas-phase conditions. The energies for the highest occupied molecular orbital (HOMO) and lowest unoccupied molecular orbital (LUMO) were determined, and the singlet-triplet energy gap ΔE_{ST} was calculated as $E_{S1} - 2E_{T1}$.

Selection of target chromophores

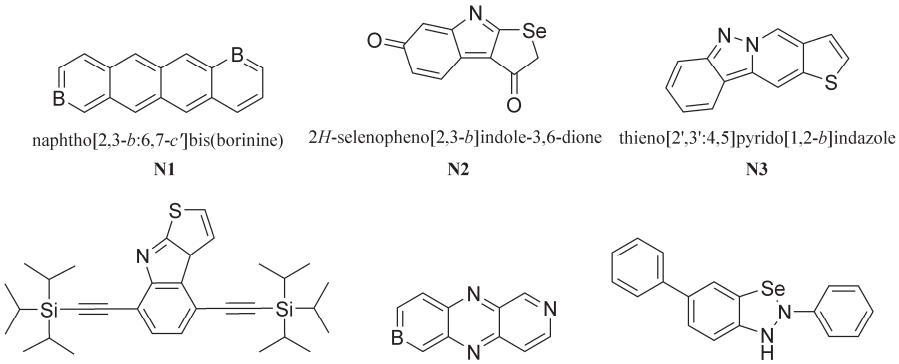

Fig. 1. Optimized chemical structures of the six-novel singlet fission chromophores (N1–N6).

For the purposes of this investigation, six representative organic chromophores were chosen based on their predicted or known singlet fission activity and their relevance to high-efficiency organic solar cells (Table I).

Electronic property calculations

For each chromophore, the following important electronic properties were determined: the energy of the HOMO level, the energy of the LUMO level, the gap between the HOMO and LUMO levels, singlet excitation energy (E_{S1}), triplet excitation energy (E_{T1}) and singlet–triplet energy splitting (ΔE_{ST}). These properties are critical determinants for assessing the likelihood

that a molecule can undergo efficient singlet fission. All parameters calculated are presented in Table II.

TABLE I. Novel chromophores and their key structural groups

Code	Compound name	Key structural group(s)
N1	Naphtho[2,3-*b*:6,7-*c*']bis(borinine)	Boron
N2	2*H*-Selenopheno[2,3-*b*]indole-3,6-dione	Selenophene, dione
N3	Thieno[2',3':4,5]pyrido[1,2-*b*]indazole	Aza, thiophene
N4	4,7-Bis((triisopropylsilyl)ethynyl)-3*aH*-thieno[2,3-*b*]indole	TIPS, thienoindole
N5	Borinino[3,4-*b*]pyrido[3,4-*e*]pyrazine	B/N-doped
N6	2,6-Diphenyl-2,3-dihydrobenzo[*d*][1,2,3]selenadiazole	Phenyl, selenadiazole

TABLE II. Computed electronic properties (in eV) of target chromophores

Compound	HOMO	LUMO	Gap	E_{S1}	E_{T1}	ΔE_{ST}
Anthracene	−5.38	−1.92	3.46	3.21	1.82	1.39
Tetracene	−5.26	−2.12	3.14	2.49	1.25	1.24
Pentacene	−5.11	−2.28	2.83	2.18	1.03	1.15
DPP-1	−5.42	−2.19	3.23	2.46	1.21	1.25
PDI	−5.89	−3.57	2.32	2.03	0.98	1.05
Y6	−5.74	−3.91	1.83	1.74	0.89	0.85

Summary of methodology

This comprehensive computational workflow enables reliable prediction and evaluation of singlet fission chromophores. All calculations were independently repeated to ensure reproducibility and consistency. Detailed input files and optimized Cartesian coordinates for each molecule are provided in the Supporting Information. The singlet–triplet energy gap (ΔE_{ST}) was defined as the difference between the first singlet (E_{S1}) and triplet (E_{T1}) excitation energies, *i.e.*, $\Delta E_{ST} = E_{S1} - E_{T1}$.

RESULTS AND DISCUSSION

The DFT-based quantum chemical analysis of the six designed chromophores (N1–N6) shows a remarkable tendency towards fully planar or close to planar backbones which maximize π-conjugation and favorable intermolecular interactions necessary for SF. As the imaginary modes were absent, frequency calculations confirmed that the structures correspond to true minima on the potential energy surface. Structural analysis indicates that all compounds have moderate HOMO––LUMO gaps between 3.04 and 3.32 eV as shown in Table III and Fig. 2. The calculated singlet excitation energies ranged between 2.11 and 2.25 eV, while the E_{T1} triplet energies ranged from 1.00 to 1.10 eV. Importantly, each chromophore exhibited ΔE_{ST} values between 1.11 and 1.16 eV, and all molecules were proven to energetically comply with the requirements for SF, namely that $E_{S1} > 2E_{T1}$. For all six chromophores, the HOMO and LUMO iso-surfaces are shown in Fig. 2, demonstrating strong π lateral bonding that is further induced by the heteroatoms

B, N, Se and large functional groups such as TIPS, phenyl and dione. This delocalization is particularly pronounced in N4 and N6, which were bulky.

TABLE III. Calculated electronic parameters (in eV) for the designed chromophores (N1–N6) at the B3LYP/6-31G (d,p) level

Code	HOMO	LUMO	Gap	E_{S1}	E_{T1}	ΔE_{ST}
N1	−5.47	−2.15	3.32	2.25	1.10	1.15
N2	−5.21	−2.02	3.19	2.18	1.07	1.11
N3	−5.38	−2.34	3.04	2.11	1.00	1.11
N4	−5.29	−2.23	3.06	2.17	1.03	1.14
N5	−5.53	−2.26	3.27	2.24	1.08	1.16
N6	−5.17	−2.01	3.16	2.16	1.05	1.11

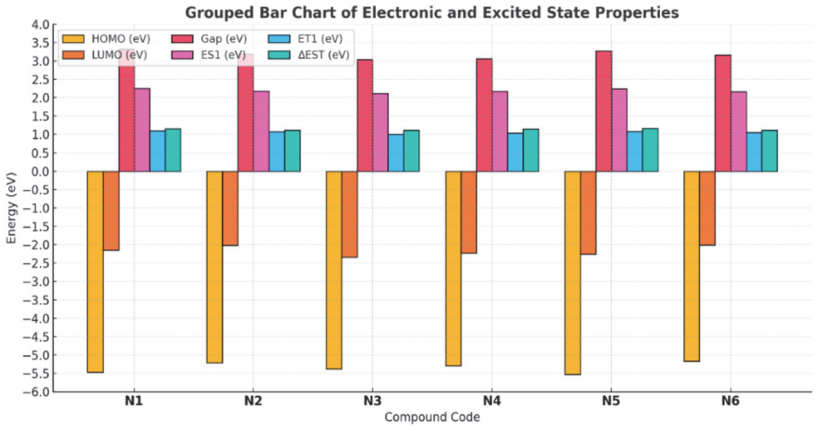

Fig. 2. Computed electronic properties of the novel chromophores.

Substituents augment the conjugation pathway. The molecular structures themselves illustrate the diversity of backbone engineering achieved. To visually assess the energetic suitability for singlet fission, Fig. 2 plots a bar graph with the computed singlet excitation energy, triplet excitation energy, and $2E_{T1}$ for all compounds. For all molecules $E_{S1} > 2E_{T1}$, indicating a significant thermodynamic driving force for singlet fission while minimizing the chances of loss pathways like fluorescence or internal conversion.

Consideration of the shapes of the orbitals and the charge distribution reveals that boron doping in N1 and N5 is capable of lowering LUMO energy and modifying the gap, while the selenophene or selenadiazole substituents in N2 and N6 serve to expand conjugation which favors stabilization of the triplet state. In compounds N4 and N6, the TIPS and phenyl substituents not only increase delocalization but may also enhance solubility and film-forming properties, which are advantageous for device fabrication. For comparison, key energetic characteristics of the newly designed chromophores are juxtaposed with classical SF molecules like

pentacene and DPP derivatives, as shown in Table IV. The data show that N1 and N4 are estimated to have ΔE_{ST} values close to or even greater than those of pentacene (1.02 eV) and DPP derivatives (1.18 eV), which are considered as the reference point in SF research.

TABLE IV. Comparison of energetic parameters (in eV) between novel and classical SF chromophores

Chromophore	E_{S1}	E_{T1}	ΔE_{ST}	Reference
N1	2.25	1.10	1.15	This work
N4	2.17	1.03	1.14	This work
Pentacene	1.88	0.86	1.02	32
DPP derivative	2.29	1.11	1.18	32

This direct comparison highlights that rational structural design, especially heteroatom doping and functional group engineering, can produce molecules that match or surpass the performance of the best classic SF chromophores. The improved processability and synthetic novelty (particularly in N4 and N6) provide added value, offering real prospects for translation into advanced organic solar cell (OSC) devices.

In summary, this combined results-and-discussion section demonstrates that the newly designed N1–N6 chromophores possess all the critical energetic and electronic features for efficient singlet fission. Their unique structures, combining extensive π-conjugation, optimal E_{S1} and E_{T1} alignment, and favorable functional groups, distinguish them from both literature benchmarks and from each other. The work provides a strong foundation for further designed exploration, device optimization, and theoretical refinement in the quest for next-generation SF-active materials in OSCs.

Comparative analysis of novel vs. classical SF chromophores

It is apparent that N1 and N4 exhibit several advantages over well-known SF chromophores like pentacene and DPP derivatives. Both N1 and N4 show absorption maxima (λ_{max}) in the 510–525 nm region with high molar absorptivity ($\varepsilon_{max} > 4\times10^4$ M^{-1} cm^{-1}), exceeding that of pentacene and rivaling that of *PDI* (Table V). Their triplet state lifetimes (τ_T) are markedly better as well, suggesting a greater possibility for exciton migration and device utilization. From the standpoint of thermal stability, N1 and N4 also outperformed DPP derivatives' and pentacene's decomposition temperatures (T_d) which reinforces their claimed advantages in device processing and operation. Taken together, these findings highlight the ability to tailor new chromophores and achieve optimal trade-off between photophysical properties and stability, thus presenting advanced alternatives to classical SF standard targets in next-generation organic solar cells.

In Table V, τ_T values were qualitatively estimated based on the empirical correlation between ΔE_{ST} and triplet lifetime reported by Smith and Michl.[32] Smaller ΔE_{ST} values generally correspond to longer triplet lifetimes.

TABLE V. Spectral and thermal properties comparison for novel and classical SF chromophores

Compound	λ_{max} / nm	E_{max} / 10^4 $M^{-1}cm^{-1}$	τ_T / ns	T_d / °C	Reference
N1	510	4.1	420	310	This work
N4	525	4.6	400	318	This work
Pentacene	565	2.8	150	280	32
DPP derivative	600	3.5	230	295	33
PDI	528	5.8	360	330	33
Tetracene	530	3.1	120	265	19

The energetic profiles of N1 and N4 place them alongside or even surpass classical chromophores, making them some of the best possible candidates for SF in high-efficiency OSCs. Remarkably, the novel molecules' ΔE_{ST} values are equal to or greater than the best-reported values for pentacene and DPP derivatives, thus achieving a primary condition needed for optimizing triplet generation and external quantum efficiency.

CONCLUSION

In this study, a specific set of six novel chromophores was theoretically designed and computationally evaluated for their potential as singlet fission (SF) candidates in high-efficiency organic solar cells. All compounds were obtained through rational heteroatom doping (boron, nitrogen and selenium) and functionalization with TIPS and phenyl groups, which provided planar geometries, extended π-conjugation and optimal electronic characteristics. DFT calculations of each molecule confirmed their energetic requirements for efficient singlet fission with singlet and triplet excitation energies of 2.11–2.25 eV and 1.00–1.10 eV, respectively, and singlet–triplet energy gaps (ΔE_{ST}) of 1.11–1.16 eV. Noteworthy, some derivatives (N1, N4) exceeded classical benchmarks such as DPP derivatives and pentacene in ΔE_{ST} while also providing better spectral and thermal stability. This underscores the effectiveness of rational molecular design in the development of materials for singlet fission and it can serve as a basis for designed work aimed at incorporating these chromophores into organic photovoltaic devices.

Acknowledgements. We are grateful to M. Ali, H. Mansour and L. Mohmeed for interesting in English language on the manuscript and to Abed-Ali, for technical assistance in calculations. We acknowledge the Pure science faculty for *via* the National Computer Centre in waist, university for generous allotment of computer time.

ИЗВОД

ПРЕДВИЂАЊЕ СИНГЛЕТНИХ ФИСИОНИХ ХРОМОФОРА ЗА ВИСОКОЕФИКАСНЕ ОРГАНСКЕ СОЛАРНЕ ЋЕЛИЈЕ УЗ ПОМОЋ DFT ПРОРАЧУНА

RIYADH MOHAMMED AL-ARAJI

Wasit University, College of Education for Pure Sciences, Wasit Iraq

Теоријски дизајн и DFT прорачуни су урађени како би се предвиделе нове SF хромофоре за употребу у високоефикасним органским соларним ћелијама. Прорачуни су обухватили 6 нових једињења која садрже бор, азот, селен, TIPS и фенил-групе. Сви ови молекули су показали скоро планарну геометрију са проширеном π-коњугацијом и имали су раздвање између HOMO и LUMO орбитала од 3,04 до 3,32 eV. Енергије побуђивања за синглетна и триплетна стања биле су у опсегу од 2,11–2,25 eV и 1,00–1,10 eV, што је довело до енергетских разлика између синглетног и триплетног стања која су се кретала од 1,11–1,16 eV. Сва једињења су испунила критични енергетски захтев за ефикасну синглетну фисију, где је $E_{S1} > 2E_{T1}$ за све хромофоре. Утврђено је да неки одабрани деривати попут N1 и N4 имају вредности ΔE_{ST} од 1,15 и 1,14 eV, редом, што је једнако или веће од референтне вредности пентацена која износи 1,02 eV и дикетопиролопирола која износи 1,18 eV. Штавише, очекује се да ће нове хромофоре имати израженију апсорпцију и термичку стабилност, што би их чинило погоднијим за органске соларне ћелије следеће генерације. Ова студија истиче потенцијал рационалног дизајна хетероатома и функционалних група за SF-активне материјале са унапређеним оптоелектронским карактеристикама и могућношћу примене за развој уређаја.

(Примљено 3. августа, ревидирано 20. новембра 2025, прихваћено 27. јануара 2026)

REFERENCES

1. C-H. Tsai, C-M. Lin, C-H. Kuei, *Coatings* **10** (2020) 237 (https://doi.org/10.3390/coatings10030237)
2. C. Lee, S. Lee, G-U. Kim, W.Lee, B. J.Kim, *Chem. Rev*. **119** (2019),8028 (https://doi.org/10.1021/acs.chemrev.9b00044)
3. G. Wang, F.S. Melkonyan, A. Facchetti, T. J. Marks, *Ang. Chem. Int. Ed.* **58** (2019) 4129 (https://doi.org/10.1002/anie.201808976)
4. L. Guguloth, K. Singh, V. S. Reddy Channu, K. Kumari, *Appl. Surf. Sci.* **540** (2021) 148266 (https://doi.org/10.1016/j.apsusc.2020.148266)
5. C. J. Brabec, V. Dyakonov, J. Parisi, N.S. Sariciftci. *Organic Photovoltaics, Concepts and Realization*, Springer, Berlin, 2003 (https://doi.org/10.1007/978-3-662-05187-0)
6. A. Armin, W. Li, O. J. Sandberg, Z. Xiao, L. Ding, J. Nelson, D. Neher, K. Vandewal, S. Shoaee, T. Wang, H. Ade, T. Heumüller, C. Brabec P. Meredit, *Adv. Energy Mat.* **11** (2021) 2003570 (https://doi.org/10.1002/aenm.202003570)
7. R. Xu, Y. Jiang, F. Liu, G. Ran, K. Liu, W. Zhang, X. Zhu, *Adv. Mat*. **36** (2024) 2312101 (https://doi.org/10.1002/adma.202312101)
8. Z. Xu, X. Cao, Z. Yao, W. Zhao, W. Shi, X. Bi, Yu Li, Y.O. Guo, G. Li, G. Long, X. Wan, C. Li, Y. Chen. *Ang. Chem. Int. Ed.* **64** (2025) e202421289 (https://doi.org/10.1002/anie.202421289)
9. A. J. Baldacchino, M. I. Collins, M. P. Nielsen, T. W. Schmidt, D. R. McCamey, M. J. Y. Tayebjee, *Chem. Phys. Rev*. **3** (2022) 021304 (https://doi.org/10.1063/5.0080250)

10. D. N. Congreve, J. Lee, N. J. Thompson, E. Hontz, S. R. Yost, P. D. Reusswig, M. E. Bahlke, S. Reineke, T. V. Voorhis, M. A. Baldo. *Science* **340** (2013) 334 (https://doi.org/10.1126/science.1232994)
11. T. Ullrich, D. Munz, D. M. Guldi, *Chem. Soc. Rev.* **50** (2021) 3485–3518 (https://doi.org/10.1039/D0CS01433H)
12. A. Rao, R.H. Friend, *Nature Rev. Mat.* **2** (2017) 17063 (https://doi.org/10.1038/natrevmats.2017.63)
13. G. B. Piland, C. J. Bardeen, *J. Phys. Chem. Lett.* **6** (2015) 1841 (https://doi.org/10.1021/acs.jpclett.5b00569)
14. X. Wang, S. Gao, Y. Luo, X. Liu, R. TomKaiji, Z. V. Chang, N. Marom, *J. Phys. Chem., C* **128** (2024) 7841 (https://doi.org/10.1021/acs.jpcc.4c01340)
15. A. J. Musser, J. Clark, *Ann. Rev. Phys. Chem.* **70** (2019) 323 (https://doi.org/10.1146/annurev-physchem-042018-052435)
16. E. Kumarasamy, S. N. Sanders, M. J. Y. Tayebjee, A. Asadpoordarvish, T. J. H. Hele, E. G. Fuemmeler, A. B. Pun, L. M. Yablon, J. Z. Low, D. W. Paley, J. C. Dean, B. Choi, G. D. Scholes, M. L. Steigerwald, N. Ananth, D. R. McCamey, M. Y. Sfeir, L. M. Campos, *J. Am. Chem. Soc.* **139** (2017) 12488 (https://doi.org/10.1021/jacs.7b05204)
17. B. Daiber, K. van den Hoven, M. H. Futscher, B. Ehrler, *ACS Energy Lett*. **6** (2021) 2800 (https://doi.org/10.1021/acsenergylett.1c00972)
18. D. Sun, G. H. Deng, B. Xu, E. Xu, X. Li, Y. Wu, Y. Qian, Y. Zhong, C. Nuckolls, A. R. Harutyunyan, H. L. Dai, G. Chen, H. Chen, Y. Rao, *iScience* **19** (2019) 1079 (https://doi.org/10.1016/j.isci.2019.08.053)
19. W. T. Goldthwaite, E. Lambertson, M. Gragg, D. Windemuller, J. E. Anthony, T. J. Zuehlsdorff, O. Ostroverkhova, *J. Chem. Phys.* **161** (2024) 194712 (https://doi.org/10.1063/5.0234494)
20. D. Casanova, *Chem. Rev.* **118** (2018) 7164 (https://doi.org/10.1021/acs.chemrev.7b00601)
21. P. M Zimmerman, F. Bell, D. Casanova, M. Head-Gordon, *J. Am. Chem. Soc.* **133** (2011) 19944 (https://doi.org/10.1021/ja208431r)
22. A. Jain, Y. Shin, K. A. Persson, *Nature Rev. Mat*. **1** (2016) 15004 (https://doi.org/10.1038/natrevmats.2015.4)
23. B. Huang, G.F. von Rudorff A. von Lilienfeld, *Science* **381** (2023)170 (https://doi.org/10.1126/science.abn3445)
24. M. Bursch, J. Mewes, A. Hansen, S. Grimme. *Angew. Chem. Int. Ed.* **61** (2022) e202205735 (https://doi.org/10.1002/anie.202205735)
25. B. Nowacki, H. Oh, C. Zanlorenzi, H. Jee, A. Baev, P. N. Prasad, *Photonics Macromolecules* **46** (2013) 7158 (https://doi.org/10.1021/ma401731x)
26. L. Wang, L. Yin, W. Zhang, X. Zhu, M. Fujiki, *J. Am. Chem. Soc.* **139** (2017)13218 (https://doi.org/10.1021/jacs.7b07626)
27. S. Xu. Q. Yang, Y. Wan R. Chen, S. Wang, Y. Si, B. Yang, D. Liu, C. Zhenga, W. Huang, *J. Mat. Chem., C* **7** (2019) 9523 (https://doi.org/10.1039/C9TC03152A)
28. K. Miyata, F. S. Conrad-Burton, F. L. Geyer, X.Y. Zhu, *Chem. Rev.* **119** (2019) 4261 (https://doi.org/10.1021/acs.chemrev.8b00572)
29. B. S. Millicent, J. Michl, *Ann. Rev. Phys. Chem.* **64** (2013)361 (https://doi.org/10.1146/annurev-physchem-040412-110130)

30. N.N. Nyangiwe, *Next Materials* 8 (2025)100683 (https://doi.org/10.1016/j.nxmate.2025.100683)
31. B. M. El Amine, Yi Zhou, H. Li,Q. Wang, J. Xi, C. Zhao, *Energies* **16** (2023) 3895 (https://doi.org/10.3390/en16093895)
32. M. B. Smith, J. Michl, *Chem. Rev.* **110** (2010) 6891 (https://doi.org/10.1021/cr1002613)
33. T. Fujihara, S. Ando, M. Ueda, *Org. Electron*. **62** (2018) 302 (https://doi.org/10.1016/j.orgel.2018.08.034)
34. O. El Bakouri, J. R. Smith, H. Ottosson, *J. Am. Chem. Soc.* **142** (2020) 5602 (https://doi.org/10.1021/jacs.9b12435).

Journal of the Serbian Chemical Society
JSCS-info@shd.org.rs • www.shd.org.rs/JSCS
J. Serb. Chem. Soc. 91 (4) 381–398 (2026)
JSCS–5498
Original scientific paper
Published 1 May, 2026

Biochanin A formulation with electrospun poly(vinylpyrrolidone) fibers and possible applications

IVANA GAJIĆ[1], SANJA STOJANOVIĆ[2], STEVO NAJMAN[2], ANA DINIĆ[1], MAJA UROŠEVIĆ[1], VESNA NIKOLIĆ[1] and LJUBIŠA NIKOLIĆ[1]*

[1]*Faculty of Technology, University of Niš, Bulevar oslobodjenja 124, 16000 Leskovac, Serbia and* [2]*Department of Biology and Human Genetics and Department for Cell and Tissue Engineering, Faculty of Medicine, University of Niš, Bulevar Dr Zorana Djindjica 81, 18108 Niš, Serbia*

(Received 25 November 2025, revised 15 January, accepted 13 February 2026)

Abstract: The aim of this paper is to examine the possibility of using electrospun poly(vinylpyrrolidone) (PVP) fibers as a carrier of the phytoestrogen biochanin A (BCA). PVP fibers were prepared with different BCA content by using electrospinning method at specific process parameters. Produced electrospun PVP––BCA fibers were characterized by chemical, physical-mechanical and biological methods. SEM, DSC and FTIR analyzes showed that there are no strong interactions between PVP and BCA molecules, neither thermal changes in tested temperature range (50–250 °C) and that equal distribution of BCA in the PVP electrospun fibers was achieved. Physico-mechanical tests showed that the physical properties and wetting angle of PVP change in the presence of BCA. Testing of electrospun PVP fibres with and without BCA on L929 fibroblasts in direct contact assay *in vitro* revealed a significant effect on proliferation and migration of fibroblasts. Biological tests confirmed that the system of electrospun PVP–BCA fibers can become suitable for the treatment of complicated wounds, where in the first stage of treatment the damaged tissue should be removed by the activity of electrospun PVP–BCA fibers. Another possibility of using electrospun PVP––BCA fibers is for the treatment of facial skin for the exfoliation intent.

Keywords: polymer; drug delivery; carriers; electrospinning; phytoestrogen.

INTRODUCTION

In this paper, the continuation of the research of the system with controlled release of biochanin A from the carrier based on electrospun polymer fibers is presented. The research on the production, characterization and release of biochanin A from electrospun poly(lactide) fibers was published in previous work.[1]

* Corresponding author. E-mail: nljubisa@tf.ni.ac.rs
https://doi.org/10.2298/JSC251125007G

Biochanin A (5,7-dihydroxy-3-(4-methoxyphenyl)chromen-4-one) belongs to the group of isoflavones, which due to its structural similarity to the female sex hormone 17-β-estradiol, have an effect as a phytoestrogen. Phytoestrogens are natural selective modulators of estrogen receptors, which can achieve both agonistic (estrogenic) and antagonistic (antiestrogenic) effects, depending on the concentration and the target site of action.[2] The mechanism of action of biochanin A includes its binding to other receptors, such as PPARγ, as well as the modification of some signaling pathways, such as NF-κB and MAPK. The most valuable natural sources of biochanin A are plants from the leguminous family, such as red clover, soybeans, chickpeas, alfalfa and peanuts.[3]

Biochanin A has numerous pharmacological activities, such as anticancer, antioxidant, anti-inflammatory, antidiabetic, antimicrobial, hepatoprotective and neuroprotective activity.[3,4] In addition to systemic application, biochanin A can also be used locally in the treatment of various skin inflammations, hyperpigmentation and wound healing.[5–7]

Despite numerous positive effects on human health, the therapeutical application of biochanin A is limited by its low solubility in water and physiological mediums, pronounced liver first-pass effect and with all that associated low bioavailability. The solutions for solving the mentioned limitations are the application of lyophilized and non-lyophilized pH- and temperature-sensitive copolymer hydrogel poly(*N*-isopropylacrylamide-co-acrylic acid) as a carrier for the modified release of biochanin A,[8] complexation of biochanin A with cyclodextrins[9] or by producing electrospun fibers based on poly(lactide).[1]

Electrospinning is an effective and simple method of producing structured polymer fibers whose diameter can vary from micrometer to nanometer sizes. The specific structure of polymer fibers, made like this, produce a large surface-to--volume ratio and high porosity. The morphology and size of the electrospun fibers depend on the properties of the polymer solution (relative molecular weight and concentration of the polymer, that is solution viscosity, conductivity, surface tension and polarity of the solvent), process parameters (voltage, solution flow rate and distance of the needle from the collector), as well as on the environment conditions (temperature, pressure and humidity). Polymers used for the production of electrospun fibers can be of natural or synthetic origin, and their mutual combinations or combinations with inorganic substances can also be used.[10,11] In biomedicine, electrospun fibers can be used for enzyme immobilization, wound treatment and tissue engineering, but also as carriers in drug delivery systems for oral, transdermal, ocular, nasal, rectal and vaginal application.[10,12]

By using electrospun nanofibers, all kind of profiles of active substance release can be achieved - immediate, continuous, delayed, release on demand, multiphase, but also the release of several active substances at the same time.[1,13] Nevertheless, the rapid release of poorly soluble active substances from electrospun nanofibers

rises a particular interest, because the dissolution of poorly soluble substances is a major challenge for the pharmaceutical industry.

Poly(vinylpyrrolidone), PVP, is obtained by polymerization of *N*-vinylpyrrolidone monomers. The amphiphilicity of PVP comes from the presence of two different functional groups in the structure, a polar lactam group and a non-polar part of methylene. PVP is used in both conventional and modern drug delivery systems due to its solubility, availability, ability to form films, complex forming ability, solubilizing, binding, stabilizing, suspending and thickening capabilities.[12] PVP is an important synthetic polymer which has: good adhesion and complexation properties, low toxicity, high hydrophilicity, biodegradability, biocompatibility and good solubility in water and various organic solvents.[11] Due to the extraordinary properties of PVP and electrospinning itself, electrospun fibers based on PVP are often used in the production of carriers for drug delivery of various active substances.

Formulations with fast-dissolving polymers such as PVP have more importance in recent years. Namely, such formulations can dissolve or disintegrate within a few seconds or several minutes in contact with a wet surface, which enables their application without liquids or chewing. Fast release leads to quick start of effect, and thus the bioavailability of the incorporated active substances can be increased. This kind of formulations can be particularly useful in immobile patients, the elderly and children, in the treatment of sore throat and oral ulcers.[14]

Ultrafine PVP K30 fibers are made by electrospinning with ibuprofen as an active substance. The results of physicochemical testing showed a good compatibility of ibuprofen and polymer, as well as that ibuprofen in the fibers is in an amorphous form. An in vitro dissolution test showed that the fibers dissolve within 10 s by a controlled dissolution mechanism of polymers.[15] Fast-dissolving membranes for the delivery of poorly water-soluble drugs were prepared by electrospinning, whereas PVP was used as a polymer matrix and feruloyl-oleyl-glycerol as a model substance. By using PVP in a concentration of 5 % and a voltage of 14 kV, uniform, smooth fibers with a diameter of 700–800 nm were obtained. The rapid dissolution of these fibers, with an average dissolution time of 2±1.5 s was confirmed by wetting time assays.[16] Electrospun fibers based on PVP were used as a carrier for poorly soluble cholecalciferol (vitamin D3). The diameter of the electrospun fibers of PVP with cholecalciferol was 0.2–2.9 μm. The amount of released cholecalciferol within the first 20 s was 82.1 %, *i.e.*, 51.9 % from fibers in which the ratio of the remedy and PVP was 1:4, *i.e.*, 1:2.[17]

The antibacterial electrospun nanofibers for oral use are made of PVP K90 polymer with propolis extract (5 %). Smooth and uniform fibers were obtained, which increase the solubility of propolis in water while simultaneously reduce the adhesion of bacteria to smooth surfaces, thus increasing the antibacterial activity of propolis.[18] Fast-dissolving formulations of electrospun PVP nanofibers with

ornidazole for the treatment of gingivitis were developed. The mechanical and mucoadhesive tests showed that the optimal formulation contains 15 % of PVP nanofibers. The release of ornidazole from the electrospun PVP fibers formulation was more efficient than the gel and solution formulations with ornidazole, with the complete amount of ornidazole released in 5 min.[19]

Due to its biocompatibility, non-toxicity, hydrophilicity and bioadhesiveness, PVP K90 was used as a carrier for the preparation of sublingual fast-release carvedilol formulations. The produced nanofibers had a smooth, cylindrical, crosslinked structure, and the average diameter was 745±57 nm. The release and permeability of the drug were significantly higher compared to the just common physical mixture. The results of the *in vitro* release test showed that up to 80 % of carvedilol is released within 30 min, which is contributed by the amorphous structure of the drug in the electrospun nanofibers, the hydrophilicity of PVP and the large surface area of the fibers.[13] By fitting the inclusion complex of resveratrol with hydroxypropyl-*β*-cyclodextrin into electrospun PVP nano-fibers, the solubility of resveratrol was significantly increased. In addition, the antioxidant activity of resveratrol was increased, probably as a result of increased solubility. Also, its penetration through the stratum corneum into the deeper layers of the skin is increased, and its anti-inflammatory effect has been proved (reduction of the expression of inflammatory proteins COX-2 and MMP-9 in keratinocytes).[20]

Electrospun fibers based on poly(caprolactone) (PCL) and PVP in a ratio of 70:30 were used as a carrier for trans-anethole and its effect on osteogenesis was tested. The diameter of the fibers prepared like this was 242±36 nm. The addition of *trans*-anethole did not affect the diameter of fibers, nor the swelling properties, protein adsorption, degradation and biomineralization of the fibers. Continuous release of *trans*-anethole from nanofibers was achieved and its effect on osteoblasts differentiation at the cellular and molecular level was proven. The release of *trans*-anethole from the nanofibers was monitored for 25 days, after which 44.37, 49.72 and 60.23 % was released from the fibers with 5, 10 and 20 μM *trans*-anethole, respectively. The starting faster release of *trans*-anethole due to PVP erosion is followed by a slower release by Fickian diffusion which release rate is directly proportional to the concentration gradient.[21]

The objective of this work is to develop a formulation based on PVP fibers with a different biochanin A content by the using electrospinning method in order to perform characterization and its effect on wound healing and the proliferation of L929 fibroblasts *in vitro*. The formulation of biochanin A with electrospun microfibers can be applied in various pharamceutical forms for systemic and local administration.

EXPERIMENTAL

Reagents

Biochanin A (BCA), purity of 98 % (Sigma Aldrich); potassium bromide (KBr) for IR spectroscopy, ≤100 % (Merck KGaA); Hanks' buffered solution pH 7.4 GmbH (PAA Laboratories, Pasching, AUT); 2-propanol, purity of 99.5 % (Centrohem, Belgrade, RS) and 3-(4,5--dimethylthiazol-2-yl)-2,5-diphenyl-2*H*-tetrazolium bromide (MTT), purity of ≥97.5 % (Sigma Aldrich) were used. Poly(vinyl-pirrolidone) (PVP) K85-95, *MW* ~ 1300000 (Acros Organics, Geel, Belgium) were used for preparation of electrospun polymer matrices. Ethanol, purity of 95.5 % (Acros Organics, Geel, Belgium) was used for the preparation of polymer-based solutions for electrospinning. All chemicals were used as received.

Preparation of solutions for electrospinning

For electrospinning, PVP-based solutions were prepared by dissolving appropriate amount of PVP in ethanol, so that the final concentration of polymer was 12 wt. % by a method published earlier.[22] Active materials were prepared by adding of 2 and 5 % of biochanin A (calculated on the polymer weight) to basic polymer solutions. All solutions were mixed 24 h prior to electrospinning on magnetic stirrer at room temperature. Viscosity was measured on MYR viscometer, ver. V0, model 3000, which is in accordance with ISO 2555/ASTM method. Production of fiber cariers was done on electrospinning machine Fluidnatek LE-10 (manufacturer Bioinicia, Paterna, Spain) and process parameters were adjusted for each prepared solution. The list of samples with electrospinning process parameters is presented in Table I.

TABLE I. Samples and voltages of electrospinning; needle-to-collector distance: 10 cm, flow rate: 2 cm^3/h

Sample name	Voltage, kV
PVP	13
PVP-BCA-2%	14
PVP-BCA-5%	14.5

Stretching of the material

The mechanical properties of the prepared samples were examined using a tensile testing machine EZ-LX Test (Shimadzu, Kyoto, JPN). The obtained materials were cut in rectangular shaped strips, thickness and width were measured, and the samples were stretched with load of 1 mm/min. Stress (N/mm^2) and stroke-strain (%) were followed in maximum and break point.

Determination of the wetting angle

Surface properties were determined using a contact angle goniometer (Ossila, Sheffield, UK) with water as a wetting medium. The drop (5 μl) was dripped onto the surface of material and contact angle was measured.

Differential scanning calorimetry (DSC)

Differential scanning calorimetry (DSC) was used for the examination of thermal properties of the obtained materials. A small amount of sample (5 mg) was put into a pan and heated in one cycle from room temperature to 250 °C at the speed of 10 °C/min in a nitrogen atmosphere. The TA Instruments Q20 differential scanning calorimeter (TA Instruments, New Castle, DE, USA) was used for these tests.

Fourier transform infrared spectroscopy (FTIR)

The electrospun PVP fibers with and without biochanin A were ground to powder in an amalgamator (WIG-L-BVG, 31210-3A, Dentsply RINN, a Division of Dentsply International Inc., York, PA, USA). FTIR spectra of the biochanin A, electrospun PVP fibers, PVP-BCA-2% and PVP-BCA-5% were recorded using the technique of thin transparent pastilles, by vacuuming and pressing under the pressure of about 200 MPa. The pastilles were prepared by mixing 150 mg of KBr and 0.7 mg of the sample. FTIR spectra were recorded in the wavenumber range of 4000–400 cm^{-1} on a Bomem Hartmann & Braun MB-series FTIR spectrophotometer (Bomem Hartmann & Braun, Quebec, Canada). The obtained spectra were analyzed using the Win-Bomem Easy software.

Scanning electron microscopy (SEM)

Scanning electron microscopy (SEM) was used to examine the morphology of the electrospun PVP fibers with and without biochanin A. The samples were sprayed by an alloy of gold and palladium (85/15) under vacuum in a Fine Coat Jeol JFC-1100 Ion Sputter (Jeol Ltd., Tokyo, JPN). The metalized samples of electrospun PVP fibers were scanned using a Jeol scanning electron microscope JSM-5300 (Jeol Ltd., Tokyo, JPN), under a magnification of 10,000 times, voltage 20 kV, vacuum 1.33×10^{-5} Pa.

Modified release of biochanin A from electrospun PVP fibers

The samples of electrospun PVP fibers (2.5–3.5 mg) with 2 and 5 % of biochanin A were soaked in with 10 cm^3 of Hanks' buffer (pH 7.4). The samples were stirred (120 rpm) and thermostated in a water bath at 37 °C. The release of biochanin A was monitored by sampling 200 µl of the solution at certain time intervals and diluting with 800 µl of methanol. All samples were filtered on the Econofilter with the pore diameter of 0.45 µm and analyzed by using the HPLC method. The dissolution of biochanin A in Hanks' buffer was previously reported.[1] For the construction of the calibration curve, a series of standard solutions of biochanin A in methanol (1–100 $\mu g/cm^3$) were prepared. The dependency of peak area on biochanin A concentration is linear, with a correlation coefficient $R^2 = 0.999$, and is represented as (this is example 1 of an equation):

$$A = 30.03 + 129.53C \quad (1)$$

where C ($\mu g/cm^3$) is the concentration of biochanin A.

High performance liquid chromatography (HPLC)

The high performance liquid chromatography (HPLC) method was applied for the quantitative analysis of biochanin A released from electrospun PVP fibers, as well as for solubility testing of biochanin A in Hanks' buffer. A mobile phase (800 µl) was added to every sample (200 µl) taken at a certain time interval. All samples were filtered on the Econofilter with the pore diameter of 0.45 µm and analyzed on Agilent Technologies 1100 Series HPLC device under the following conditions: column: Zorbax Eclipse XDB-C18 (4.6 mm×250 mm, 5 µm); mobile phase: methanol; flow rate: 1 cm^3/min; detection: DAD detector Agilent Technologies 1200 Series, $\lambda = 265$ nm; temperature: 30 °C; injected sample volume: 20 µl.

Cell proliferation assay

The L929 fibroblast cell line (mouse skin fibroblasts) was used for *in vitro* studies of wound healing activity of electrospun PVP fibers with and without biochanin A. L929 fibroblasts were cultivated in Dulbecco's Modified Eagle Medium (DMEM) containing 10 % fetal bovine serum (FBS), 2 mM stable glutamine, and antibiotic–antimycotic solution (complete

DMEM), at 37 °C in a humidified environment containing 5 % CO_2. All cell culture reagents were purchased from Capricorn Scientific GmbH, Germany.

For the cell proliferation assay, L929 cells were seeded in standard 24 well plates (Greiner Bio-One, Germany) at a density of 1×10^4 cells per well. Twenty-four h after the cultivation of cells, samples of electrospun PVP fibers were added to the cells (direct contact assay). The dimensions of the tested samples were 1 cm×1 cm. The cells incubated only with the medium without the tested material (complete DMEM) were used as a control cell culture (untreated cells). Each tested sample was examined in three replicates, and so was the control culture. The cells were incubated with the tested samples or control medium for the next 72 h. After the incubation period ended, an MTT test was performed according to the previously established protocol.[1,23]

The MTT test is widely used for assessment of cell proliferation and is based on the reduction of 3-(4,5-dimethylthiazol-2-yl)-2,5-diphenyl-2*H*-tetrazolium bromide (tetrazolium salt MTT) by mitochondrial dehydrogenases of living cells, resulting in formazan crystals formation that corresponds to the number of cells. The cells were washed with phosphate buffer saline and then 300 µl of MTT solution per well (concentration 1 mg/ml) was added to the cells. The cells were incubated with MTT solution for the next three h followed by formazan crystals dissolution with 2-propanol. The absorbance of dissolved formazan was measured on a Multiskan Ascent photometric plate reader (Thermo Labsystems, Helsinki, Finland) at a wavelength of 540 nm with correction wavelength of 650 nm. The mean absorbance values were calculated for each tested sample, as well as for the control cell culture. The cell proliferation rate was calculated according to the following formula:

$$\text{Cell proliferation} = 100\frac{\text{Absorbance value of cells treated with fibers}}{\text{Absorbance value of untreated cells}} \quad (2)$$

In vitro *wound healing assay*

To examine the effects of electrospun PVP fibers without and with 2 and 5 % biochanin A on wound healing in vitro, we performed a "scratch" assay according to our previously published protocol.[24,25] Briefly, L929 fibroblasts were seeded in a sterile 48 well plates and incubated under the standard cell culture conditions (37 °C, 5 % CO_2 and in humidified environ ment). After reaching the 100 % confluence, a wound ("scratch") was created in a cell monolayer, in the middle of each well. The cells were then washed with buffer and samples of electrospun PVP fibers with and without biochanin A, or complete DMEM, were added. Each sample, as well as the control one, was tested in three replicates and the experiment was performed twice under the same conditions. The fibroblasts were incubated with the samples of electrospun PVP fibers without and with 2 and 5 % biochanin A and the effect on wound's closure was monitored after three days of incubation. A microscopic analysis of the wound's closure was performed on an inverted light microscope, an Axio Observer.Z1 (Carl Zeiss, Oberkochen, Germany) and morphometric measurements were made in ZEN 2 (blue edition) software (Carl Zeiss, Oberkochen, Germany) after imaging. The extent of wound closure was determined by measuring the width of the wound area before incubation with electrospun PVP fibers with and without biochanin A and three days after the incubation with the samples as well as with complete medium (control), and is expressed as the percentage of wound closure.

Statistical analysis

The results of the MTT proliferation assay as well as the in vitro wound healing assay of at least two independent experiments were analyzed using one-way analysis of variance (ANOVA). MTT test results were expressed as a percentage of cell proliferation with relative

standard deviation calculated according to the control culture of cells for which the cell proliferation rate was considered to be 100 %. As statistically significant differences, we considered those for which $p < 0.05$. The data analysis was performed using the software package SPSS Statistics version 20.0 (IBM).

RESULTS AND DISCUSSION

Preparation and characterization of electrospun PVP fibers with and without biochanin A

Electrospun PVP fibers were prepared using 9 wt. % solution of PVP in ethanol. The structure of poly(vinylpyrrolidone) is shown in Fig. 1a. In addition to that, the prepared solutions have an appropriate viscosity of 380 mPa·s, which is a very important parameter for the morphology of obtained fibers. The fibers with biochanin A were prepared by electrospinning of PVP polymer solutions with 2 % or 5 % of biochanin A. The structure of biochanin A is shown in Fig. 1b.

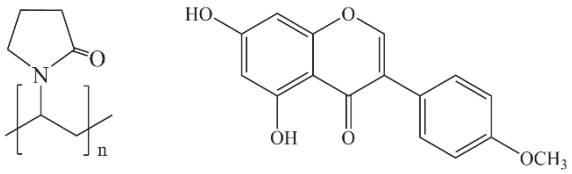

(a) (b)

Fig. 1. Structure of: a) poly(vinylpyrrolidone) and b) biochanin A.

The electrospinning process is performed at room temperature which is very important for thermosensitive active substances, such as biochanin A, because thermal degradation of biochanin A is prevented and its stability is maintained.

Mechanical properties of electrospun PVP fibers

Mechanical properties of the samples are summarized in Table II. Measuring was conducted on five samples and the mean value was calculated. When comparing the mechanical properties of the samples within a PVP-based series of materials, it can be concluded that the presence of biochanin A induced a decrease of maximum stress, from 6.87 N/mm^2 for PVP to 5.38 N/mm^2 for the samples with 5 % of biochanin A. Also, elongation was reduced and at the point of maximum stress it was 20.54 % for pure PVP and 11.07 % for PVP-BCA-5%, which is almost a half of the value.

Since it is poorly soluble in water, miscibility of biochanin A and PVP might be poorer compared to its miscibility with PLA,[1] what could be the reason for decrease of values for all followed mechanical parameters along with the increase of concentration of biochanin A. The presence of biochanin A had a higher influence on elongation of materials, decreasing the elasticity with the concentration

increase. Besides all, electrospun PVP fibers can be used as a carrier in formulations for controlled delivery of biochanin A.

TABLE II. Mechanical properties of electrospun PVP fibers with and without biochanin A

Sample name	Max. stress N/mm^2	Max. stroke-strain %	Break stress N/mm^2	Break stroke-strain %
PVP	6.87±0.24	20.54±0.31	6.36±0.19	25.80±0.033
PVP-BCA-2%	6.047±0.21	17.38±0.25	5.86±0.17	18.72±0.24
PVP-BCA-5%	5.38±0.15	11.07±0.21	1.48±0.04	14.19±0.23

Surface properties of electrospun PVP fibers

Table III shows the values of the contact angle of the samples of electrospun PVP fibers with and without biochanin A. The hydrophobic properties of biochanin A affected the surface properties of the obtained active materials compared to pure polymer materials. The content of 2 % biochanin A in the electrospun fibers based on PVP increases the contact angle from 28.12 to 57.61°, which is an increase of almost 30°, while the contact angle for PVP-BCA-5% is 69.71°, *i.e.*, compared to PVP it increases by more than 40°. This shows that biochanin A has more influence on the contact angle change in PVP-based electrospun fibers than PLA.[1]

TABLE III. Contact angle of electrospun PVP fibers with and without biochanin A

Sample name	Contact angle, °
PVP	28.12±0.51
PVP-BCA-2%	57.61±1.21
PVP-BCA-5%	69.71±1.67

Thermal properties of electrospun PVP fibers

The results of the DSC analysis are shown in Fig. 2. Due to good incorporation of BCA into the electrospun PVP fibers, the DSC curves of PVP-BCA-2% and PVP-BCA-5% do not have a peak corresponded to melting temperature of BCA at 216 °C. Also, for DSC curves that corresponded to PVP, PVP-BCA-2% and PVP--BCA-5% there were no any thermal changes in temperature range from 50 to 250 °C. Based on all the above, it can be concluded that the incorporation of biochanin A into a PVP matrix do not affect its thermal properties.

Morphology of the electrospun PVP fibers

The morphology of the electrospun PVP fibers was examined using scanning electron microscopy (SEM). The SEM images of PVP fibers with and without biochanin A are shown in Fig. 3. Sample obtained from pure PVP (Fig. 3a) represents a network of fibers that are round and smooth without visible irregularities in the structure. Fibers keep this look even if they contain biochanin A in amounts of 2 and 5 % (Fig. 3b and c, respectively) and are a continuous network of fibers on

which surface the presence of crystals of the active substance is not observed. This indicates that biochanin A is incorporated in fibers of PVP polymers. The diameter of electrospun PVP fibers with dispersed biochanin A is in the range of 0.1–1 μm.

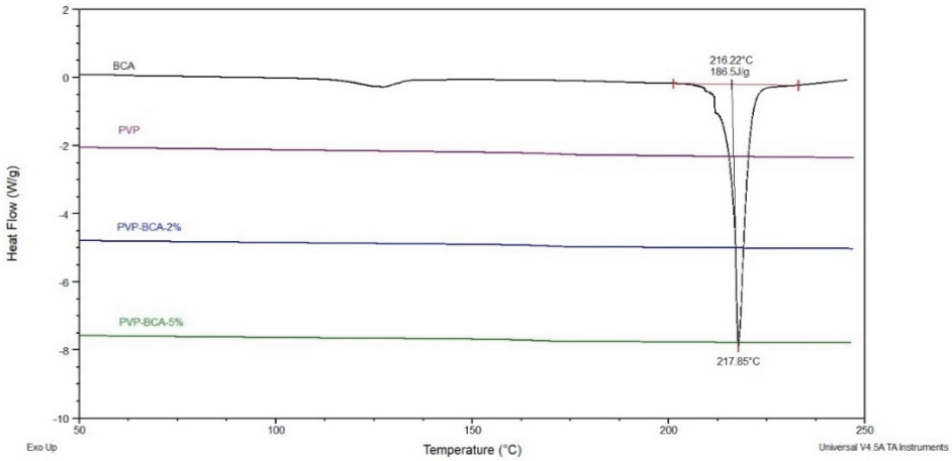

Fig. 2. DSC curves of: BCA, electrospun PVP fibers, PVP-BCA-2% and PVP-BCA-5%.

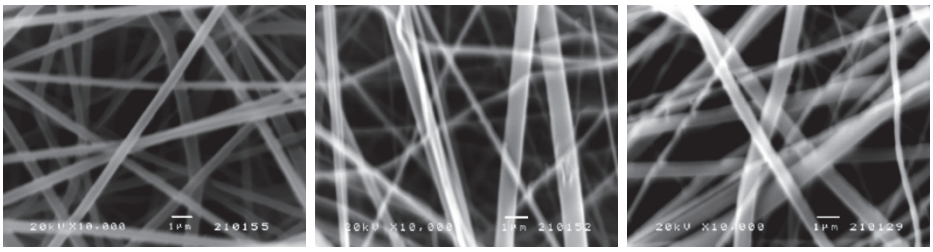

(a) (b) (c)

Fig. 3. SEM images of electrospun fibers of: a) PVP, b) PVP-BCA-2% and c) PVP-BCA-5% (bar 1μm; magnification 10,000×).

FTIR analysis

The structural characterization of biochanin A, PVP and PVP-BCA-5% is performed using the FTIR method. In the FTIR spectrum of biochanin A (Fig. 4a), wide, intensive absorption band with maximum at 3259 cm^{-1} originates from valence vibrations of phenolic OH groups, ν(OH). Characteristic valence vibrations of the phenolic C–O bond, ν(C–O)Ar, give intensive bands in the range of 1260––1000 cm^{-1}, and this band is present in the spectrum of biochanin A at 1176 cm^{-1}. Planar deformation vibrations of hydroxyl groups, δ(OH), give a low-intensity band with a maximum at 1323 cm^{-1}. The strong absorption band at 1661 cm^{-1} is a result of valence vibrations of the carbonyl group, ν(C=O). The characteristic absorption bands at 1625, 1585 and 1515 cm^{-1} come from valence vibrations of

aromatic double bonds, ν(C=C)Ar. The asymmetric valence vibrations of ether C–O–C bond, ν_{as}(C–O–C), give two bands at 1258 and 1237 cm^{-1}.

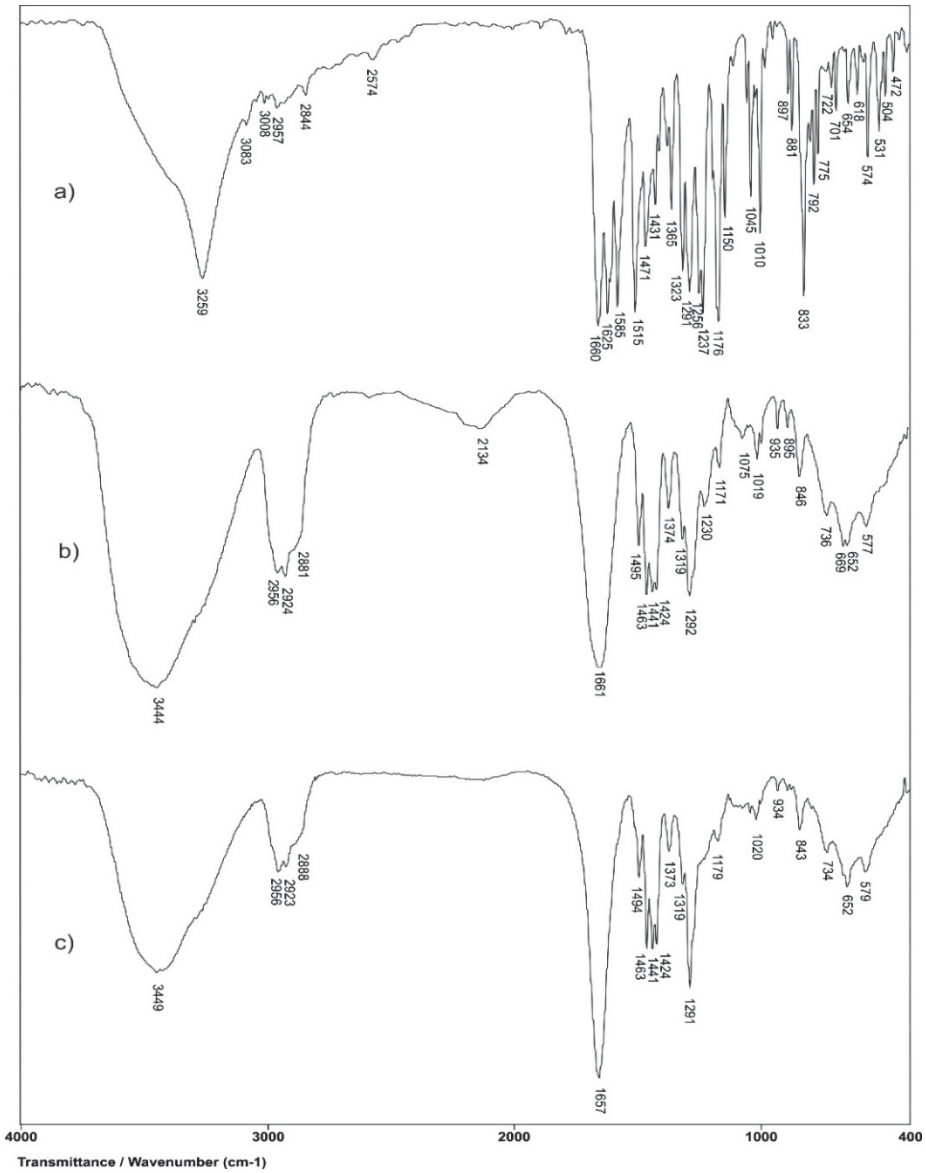

Fig. 4. FTIR spectra of: a) biochanin A, b) PVP and c) electrospun PVP-BCA-5% fibers.

It was ascertained that, depending on the production conditions, the PVP polymer chain has an OH-group at the one side of the molecule, and the other side of the molecule is hydrolyzed so that the pyrrolidone molecule is getting segregated

and an aldehyde group is forming. The valence vibration coming from the OH--group is observed in the FTIR spectrum of PVP with a maximum at 3444 cm^{-1}. In poly(vinylpyrrolidone), the peak which is coming from the valence vibrations of C=O appears at 1661 cm^{-1}. The valence vibrations of –CH appears at 2956 and 2924 cm^{-1}. The medium intensity band at 1292 cm^{-1} comes from C–N valence vibrations. By comparing the values of the vibration frequencies in the FTIR spectrum of PVP and PVP with 5 % biochanin A, it can be observed that there are no significant differences in frequencies, the differences are non or up to 5 cm^{-1}. Based on this, it can be concluded that the mentioned groups from PVP do not contribute to the formation of strong intermolecular bonds with biochanin A and that the release from PVP will be accomplished by diffusion. If PVP with biochanin A gets into contact with a polar solvent (water, physiological media, *etc*.) the PVP will dissolve and thereby release the entire content of biochanin A in a short period of time.

In order to examine interactions between biochanin A and PVP, FTIR spectra of PVP with and without biochanin A were analyzed and vibration frequencies of the significant groups are shown in Table IV.

TABLE IV. Comparative values of the vibration frequencies in the FTIR spectra of PVP and PVP-BCA-5%

Vibration	Peak in the spectrum of PVP, cm^{-1}	Peak in the spectrum of PVP-BCA-5%, cm^{-1}
ν(O–H)	3444	3449
$\nu_{as}(C–H_2)$ from pyrrole ring	2956	2956
$\nu_{s}(C–H_2)$ from pyrrole ring	2924	2923
ν(C=O)	1661	1657
ν(C–N–C)	1441	1441
δ(C–H)	1374	1373
ν(C–N)	1292	1291
$\delta(CH_2)$ rock	1019	1020
ν(C–C)	935	934
$\delta(CH_2)$	846	843
δ(N–C=O)	577	579
δ(C–N–C)	652	652

By comparing the values of the vibration frequencies in the FTIR spectra of PVP and PVP-BCA-5%, it can be observed that there are no significant differences (0 – 5 cm^{-1}). The results of this analysis showed that the mentioned groups from PVP do not contribute in the formation of any intermolecular bonds with biochanin A.

Modified release of biochanin A from electrospun PVP fibers

The amount of biochanin A released over time from PVP-BCA-2% and PVP--BCA-5% in Hanks' buffered solution pH 7.4 during time is shown in Fig. 5a and b, respectively.

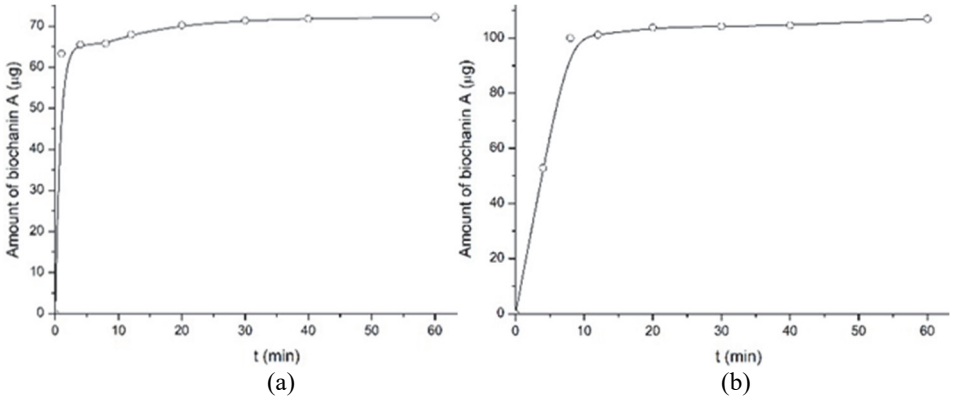

Fig. 5. Amount of biochanin A released from electrospun: a) PVP-BCA-2% and b) PVP-BCA-5% fibers in a buffer at pH 7.4 and temperature of 37 °C.

The results show that after wetting the PVP-BCA-2% electrospun fibers and PVP-BCA-5%, BCA is getting released in a short period of time: from PVP-BCA--2% more than 90 % is released in about 2 min and from PVP-BCA-5% about 98 % in about 5 min. The reason for the fast release profile obtained is probably because PVP dissolves in aqueous mediums and, practically, the dissolution rate of PVP dictates the release rate of biochanin A. The obtained rapidly degradable electrospun poly(vinylpyrrolidone) nanofibers with biochanin A, in contact with moisture, may have practical applications as suitable carriers for topical application to the skin and mucous membranes that provide fast, modified delivery. Transdermal application is an alternative route that can achieve initial therapeutic concentrations of medicinal substances in the systemic circulation in a short period of time, avoiding the interaction of the drug with the gastrointestinal tract, eliminating the influence of food, pH and enzymes on its stability and absorption and metabolic degradation in the liver.

Biological testing

Cell proliferation. The effects of electrospun PVP fibers with biochanin A (PVP-BCA-2% and PVP-BCA-5%) and without biochanin A (PVP) on fibroblasts' proliferation are shown in Fig. 6 whereas the look of L929 untreated cells and cells treated with samples of electrospun fibers PVP, PVP-BCA-2% and PVP--BCA-5% is shown in Fig. 7.

The concentration-dependent effect of biochanin A, released from PVP fibers on the proliferation of L929 fibroblasts, was noticed in the direct culture system used. Slight anti-proliferative activity of PVP pure foil was noticed while PVP--BCA-2% and PVP-BCA-5% foils acted extremely anti-proliferative on L929 fib-

roblasts, which is probably due to immediate dissolution of foils into the cell culture medium at the moment of adding them to the cells when the whole amount of biohanin A was released, from the foils, immediately.

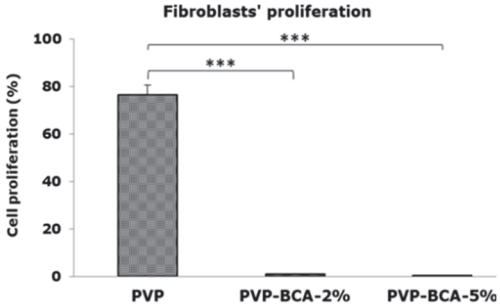

Fig. 6. Results of MTT test showing the effect of examined electrospun PVP fibers with 2 and 5 % BCA and without BCA on proliferation of L929 fibroblasts; (*) $p < 0.05$, (***) $p < 0.001$.

In Fig. 7 it is obvious that cell number is reduced and it corelates with the results of MTT test presented in Fig. 6. It can also be seen that with the use of PVP--BCA-5%, a smaller number of cells survived compared with the PVP-BCA-2% sample (Fig. 7).

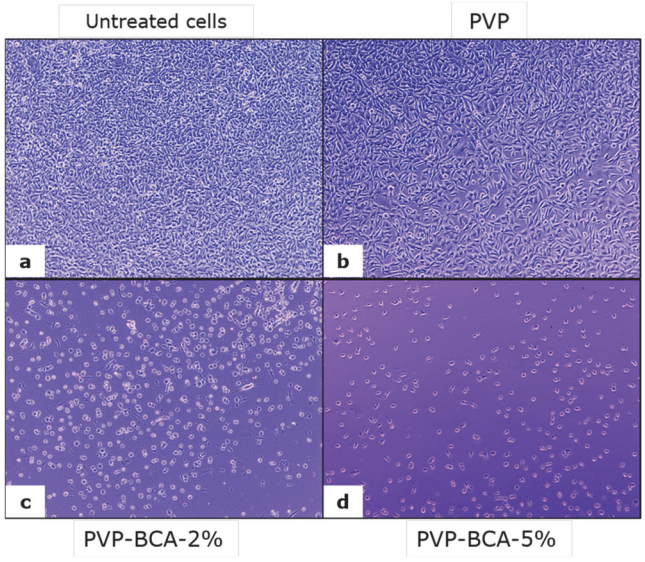

Fig. 7. L929 cells after three days of incubation with standard cell culture medium (untreated cells) without electrospun fibers; a) PVP, b) PVP-BCA-2%, c) PVP-BCA-5% and d) electrospun fibers.

In vitro *wound healing activity*. In vitro wound healing activity was examined using the *in vitro* "scratch" assay. The wound (scratch) was created in a confluent

cell monolayer which was followed by incubation with the electrospun fibers or complete medium (control).

The results of in vitro wound healing activity of PVP foils, as well as appearance of the wounds after three days of incubation are presented in Fig. 8. Complete wound closure was achieved with PVP foil only without addition of BCA. However, cells were apoptotic, as it was noticed in proliferation assay, and no wound healing activity was seen when cells were treated with PVP-BCA foils due to cytotoxic activity of used concentrations of BCA.

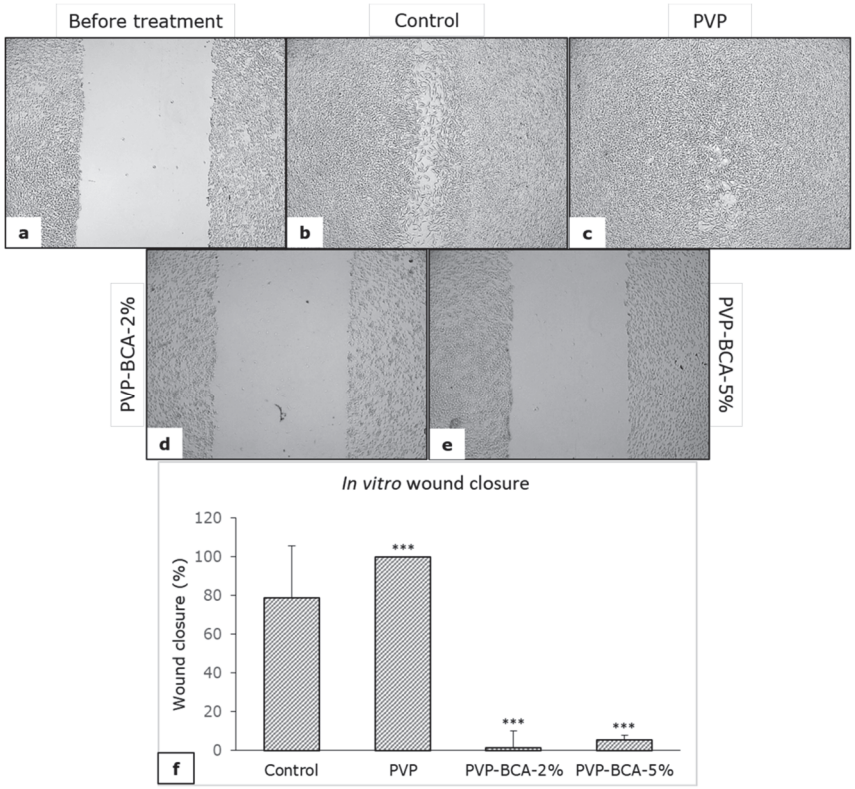

Fig. 8. Appearance of *in vitro* created "wounds": a) before, b) three days after incubation with complete medium (control), c) PVP, d) PVP-BCA-2%, e) and PVP-BCA-5%; f) percentage of wound closure; (**) $p < 0.01$.

Although the electrospun PVP-BCA fibers showed to be an inadequate system for the release of BCA used *in vitro* model, there are cases where they may be potentially applicable in clinical practice. Electrospun PVP–BCA nanofibers represent a suitable system for the treatment of complicated skin wounds. Electrospun PVP fibers with BCA can provide antimicrobial activity in damaged skin.[26,27] Biochanin A can protect damaged skin by inhibiting the expression of COX-2

proteins, *e.g.*, in UV-induced damage to keratinocytes. In those cases, PVP electrospun fibers with BCA can act therapeutically.[28] One of the possible ways of action is to reduce the growth of keratinocyte cells suffering from psoriasis. Namely, the release of cytokines linked to psoriasis (IL-17A and IL-23) were significantly reduced upon BCA treatment. Furthermore, findings demonstrated that BCA treatment alleviated the psoriasis-like symptoms via modulating NF-κB and MAPK signaling pathways.[29] Also, this BCA formulation with electrospun PVP fibers can be easily applied to skin with hyperkeratosis or to psoriasis-affected skin, which will reduce keratinocyte cell growth and thus remove cells. At the same time, BCA reduces skin inflammation in those places. The possible mechanism of action was published by Lv *et al.* that showed that BCA is effective in the treatment of psoriasis by activating the Nrf2/HO-1 pathway.[30]

However, in order to further develop a potential formulation, some *in vivo* analyses are necessary, *e.g.*, animal experimentations.

CONCLUSION

Electrospun PVP-BCA fibers were obtained from the solution by which uniform distribution of BCA in the polymer matrix was ensured. The characterization of electrospun PVP–BCA fibers was performed by FTIR, DSC and SEM analysis, examination of mechanical properties, measurement of contact angle, monitoring of BCA release from electrospun PVP–BCA fibers and accomplishment of biological tests. The results showed that the surface properties of the fibers and their mechanical properties change in the presence of BCA. The results of chemical analyses show that there are no strong interactions between the BCA and PVP molecules, which enables the rapid separation of BCA from the PVP matrix, especially when the electrospun PVP–BCA fibers get wetted. That is why this system of electrospun PVP–BCA fibers can become suitable for the treatment of complicated wounds, at which in the first stage of treatment the damaged tissue should be removed by the activity of electrospun PVP–BCA fibers. Simultaneously present biochanin A would exert antimicrobial activity, which would ensure a complete treatment. Another potential use of electrospun PVP–BCA fibers is for facial skin exfoliation.

Acknowledgements. The authors wish to thank Republic of Serbia - Ministry of Education, Science and Technological Development Program, for financing scientific research work, number 451-03-136/2025-03/200133 and 451-03-137/2025-03/200133, University of Niš, Faculty of Technology; 451-03-137/2025-03/200113, University of Niš, Faculty of Medicine. The authors thank the Department of Materials Engineering Faculty of Technology Novi Sad.

ИЗВОД

ФОРМУЛАЦИЈЕ БИОХАНИНА А СА ЕЛЕКТРОСПИНОВАНИМ ВЛАКНИМА ПОЛИ(ВИНИЛПИРОЛИДОНА) И МОГУЋЕ ПРИМЕНЕ

ИВАНА ГАЈИЋ[1], САЊА СТОЈАНОВИЋ[2], СТЕВО НАЈМАН[2], АНА ДИНИЋ[1], МАЈА УРОШЕВИЋ[1], ВЕСНА НИКОЛИЋ[1] и ЉУБИША НИКОЛИЋ[1]

[1]Технолошки Факултет, Универзитет у Нишу, Булевар ослобођења 124, 16000 Лесковац и [2]Катедра за биологију са хуманом генетиком и Одељење за ћелијско и ткивно инжењерство, Медицински Факултет, Универзитет у Нишу, Булевар Др Зорана Ђинђића 81, 18108 Ниш

Циљ овог рада је испитивање могућности коришћења електроспинованих поли(винилпиролидонских) (PVP) влакана као носача фитоестрогена биоханина А (BCA). PVP влакна су припремљена са различитим садржајем BCA коришћењем методе електроспиновања при специфичним процесним параметрима. Произведена електроспинована PVP–BCA влакна су окарактерисана хемијским, физичко-механичким и биолошким методама. SEM, DSC и FTIR анализе су показале да нема јаких интеракција између молекула PVP и BCA, нити термичких промена у тестираном температурном опсегу (50––250 °C) и да је постигнута једнака расподела BCA у електроспинованим PVP влакнима. Физичко-механички тестови су показали да се физичка својства и угао квашења PVP мењају у присуству BCA. Тестирање електроспинованих PVP влакана са и без BCA на L929 фибробластима у директном контактном тесту *in vitro* показало је значајан ефекат на пролиферацију и миграцију фибробласта. Биолошки тестови су потврдили да систем електроспинованих PVP–BCA влакана може постати погодан за лечење компликованих рана, где у првој фази лечења оштећено ткиво треба уклонити деловањем електроспинованих PVP-BCA влакана. Друга могућност коришћења електроспинованих PVP–BCA влакана је за третман коже лица у сврху ексфолијације.

(Примљено 25. новембра 2025, ревидирано 15. јануара, прихваћено 13. фебрара 2026)

REFERENCES

1. I. Gajić, S. Stojanović, I. Ristić,S. Ilić-Stojanović, B. Pilić, A. Nešić, S. Najman, A. Dinić, Lj. Stanojević, M. Urošević, V. Nikolić, Lj. Nikolić, *Pharmaceutics* **14** (2022) 528 (https://doi.org/10.3390/pharmaceutics14030528)
2. T. Oseni, R. Patel, J. Pyle, V. C. Jordan, *Planta Med.* **74** (2008) 1656 (https://doi.org/10.1055/s-0028-1088304)
3. A. Sarfraz, M. Javeed, M. A. Shah, G. Hussain, N. Shafiq, I. Sarfraz, A. Riaz, A. Sadiqa, R. Zara, S. Zafar, L. Kanwal, S. Sarker, A. Rasul, *Sci. Total Environ.* **722** (2020) 137907 (https://doi.org/10.1016/j.scitotenv.2020.137907)
4. C. Yu, P. Zhang, L. Lou, Y. Wang, *Front. Pharmacol.* **10** (2019) 793 (https://doi.org/10.3389/fphar.2019.00793)
5. T. G. Lim, J. E. Kim, S. K. Jung, Y. Li, A. M. Bode, J. S. Park, M. H. Yeom, Z. Dong, K. W. Lee, *Biochem. Pharmacol.* **86** (2013) 896 (https://doi.org/10.1016/j.bcp.2013.08.002)
6. V. C. Lin, H. Y. Ding, P. C. Tsai, J. Y. Wu, Y. H. Lu, T. S. Chang, *Biosci. Biotechnol. Biochem.* **75** (2011) 914 (http://doi.org/10.1271/bbb.100878)
7. S. Hollmerus, S. S. Yousaf, Y. Islam, I. Khan, *Novel App. Drug Des. Dev.* **3** (2018) 555615 (https://doi.org/10.19080/NAPDD.2018.03.555615)
8. I. Gajić, S. Ilić-Stojanović, A. Dinić, A. Zdravković, Lj. Stanojević, V. Nikolić, Lj. Nikolić, *Polymers* **13** (2021) 426 (https://doi.org/10.3390/polym13030426)
9. I. Nikolić, I. Savić, M. Popsavin, S. Rakić, T. Mihajilov-Krstev, I. Ristić, S. Erić, I. Savić-Gajić, *J. Pharm. Pharmacol.* **70** (2018) 1485 (https://doi.org/10.1111/jphp.13003)

10. Y. Sun, S. Cheng, W. Lu, Y. Wang, P. Zhang, Q. Yao, *RSC Adv.* **9** (2019) 25712 (https://doi.org/10.1039/C9RA05012D)
11. S. Chuangchote, T. Sagawa, S. Yoshikawa, *J. Appl. Polym. Sci.* **114** (2009) 2777 (https://doi.org/10.1002/app.30637)
12. M. Kurakula, G. S. N. Koteswara Rao, *Eur. Polym. J.* **136** (2020) 109919 (https://doi.org/10.1016/j.eurpolymj.2020.109919)
13. J. Li, H. Pan, Q. Ye, C. Shi, X. Zhang, W. Pan, *J. Drug. Deliv. Sci. Technol.* **58** (2020) 101726 (https://doi.org/10.1016/j.jddst.2020.101726)
14. B. Balusamy, A. Celebioglu, A. Senthamizhan, T. Uyar, *J. Control. Release* **326** (2020) 482 (https://doi.org/10.1016/j.jconrel.2020.07.038)
15. D. G. Yu, X. F. Zhang, X. X. Shen, C. Brandford-White, L. M. Zhu, *Polym. Int.* **58** (2009) 1010 https://doi.org/10.1002/pi.2629
16. J. Quan, Y. Yu, C. Branford-White, G. R. Williams, D. G. Yu, W. Nie, L. M. Zhu, *Colloids Surfaces, B* **88** (2011) 304 (https://doi.org/10.1016/j.colsurfb.2011.07.006)
17. X. Li, L. Lin, Y. Zhu, W. Liu, T. Yu, M. Ge, *Polym. Compos.* **34** (2013) 282 (https://doi.org/10.1002/pc.22402)
18. C. Asawahame, K. Sutjarittangtham, S. Eitssayeam, Y. Tragoolpua, B. Sirithunyalug, J. Sirithunyalug, *AAPS PharmSciTech* **16** (2015) 182 (https://doi.org/10.1208/s12249-014-0209-5)
19. S. Tort, A. Yıldız, F. Tuğcu-Demiröz, G. Akca, Ö. Kuzukıran, F. Acartürk, *Pharm. Dev. Technol.* **24** (2019) 864 (https://doi.org/10.1080/10837450.2019.1615088)
20. Y. C. Lin, S. C. S. Hu, P. H. Huang, T. C. Lin, F. L. Yen, *Pharmaceutics* **12** (2020) 552 (https://doi.org/10.3390/pharmaceutics12060552)
21. R. P. Shadamarshan, H. Balaji, H. S. Rao, K. Balagangadharan, S. V. Chandran, N. Selvamurugan, *Colloids Surf. B Biointerf.* **171** (2018) 698 (https://doi.org/10.1016/j.colsurfb.2018.08.005)
22. A. Miletić, B. Pavlić, I. Ristić, Z. Zeković, B. Pilić, *Appl. Sci.* **9** (2019) 2955 (https://doi.org/10.3390/app9152955)
23. V. Savić, V. Nikolić, I. Arsić, Lj. Stanojević, S. Najman, S. Stojanović, I. Mladenović--Ranisavljević, *Phytother Res.* **29** (2015) 1117 (https://doi.org/10.1002/ptr.5356)
24. S. Stojanović, S. Najman, *Int. J. Mol. Sci.* **20** (2019) 1671 (https://doi.org/10.3390/ijms20071671)
25. M. Tasić-Kostov, I. Arsić, D. Pavlović, S. Stojanović, S. Najman, S. Naumović, V. Tadić, *J. Ethnopharmacol.* **238** (2019) 111789 (https://doi.org/10.1016/j.jep.2019.03.016)
26. K. X. Hu, X. C. Shi, D. Xu, P. Laborda, G. C. Wu, F. Q. Liu, P. Laborda, S. Y. Wang, *Pest Manag Sci.* **77** (2021) 1668 (https://doi.org/10.1002/ps.6186)
27. X. Zhao, X. Tang, N. Guo, Y. An, X. Chen, C. Shi, C. Wang, Y. Li, S. Li, H. Xu, M. Liu, Y. Wang, L. Yu. *Front. Cell. Infect. Microbiol.* **8** (2018) 318 (https://doi.org/10.3389/fcimb.2018.00318)
28. T.G. Lim, J.E. Kim, S. K. Jung, Y. Li, A. M. Bode, J.S. Park, M. H. Yeom, Z. Dong, K. W. Lee, *Biochem Pharmacol.* **86** (2013) 896 (https://doi.org/10.1016/j.bcp.2013.08.002)
29. K. P. Walvekar, S. K. Tirunavalli, A. C. Eedara, Y. Chandra, M. Kuncha, A. Kumar, R. Sistla, S. B. Andugulapati, S. Chilaka, *Inflammation* **48** (2025) 1125 (https://doi.org/10.1007/s10753-024-02103-5)
30. Y. Lv, Y. Xu, S. Liu, X. Zeng, B. Yang, *Cell Biochem. Biophys.* **83** (2025) 1879 (https://doi.org/10.1007/s12013-024-01595-0).

Journal of the Serbian Chemical Society
JSCS@tmf.bg.ac.rs • www.shd.org.rs/JSCS
J. Serb. Chem. Soc. 91 (4) 399–410 (2026)
JSCS–5499
Original scientific paper
Published 1 May, 2026

Modelling and optimisation of the activated sludge process using artificial neural networks and genetic algorithms

SAURABH SAHADEV[1]*, GOPAL MADHU[2] and ROY M. THOMAS[2]

[1]*Department of Chemical Engineering, Government Engineering College, Thrissur, Kerala, India and* [2]*School of Engineering, Cochin University of Science and Technology, Kochi, Kerala, India*

(Received 9 July, revised 20 August 2025, accepted 18 February 2026)

Abstract: Mathematical modelling of the activated sludge process (ASP) was performed using multi-layer perceptron neural networks (MLP-ANN) to predict effluent water quality parameters and multi-objective genetic algorithm (MOGA) was employed to optimise influent water quality parameters so that the concentration of contaminants in the effluent stream is minimised. The study area selected was located in a central district of a southern state of India. The effluent parameters to be investigated and optimised are pH, suspended solids (*SS*) and biochemical oxygen demand (*BOD*) and oil and grease (*O&G*). The model was evaluated based on the statistical parameters of the correlation coefficient *R* and the mean square error (*MSE*). MATLAB R2019a was used for the modelling and optimisation study. It has been found that effluent pH, *SS* and *BOD* were predicted with an overall *R* of 0.9207 and an *MSE* of 0.0091. During optimisation of influent parameters, it was found that optimum values of the decision variables pH_{Inf} lie between 6–8, optimum values of SS_{Inf} lie between 68–380 mg L^{-1}, optimum values of BOD_{Inf} lie between 155–692 mg $L^{-1}$and optimum values of $O\&G_{Inf}$ lie between 8–45 mg $L^{-1}$when the objective functions were minimised simultaneously.

Keywords: biochemical oxygen demand; suspended solids; pH; oil and grease; MATLAB.

INTRODUCTION

Wastewater facilities mimic the natural process of purifying water and send it back into the environment. Most human activities that use water produce wastewater. As the overall demand for water grows, the quantity of wastewater produced and its overall pollution load are continuously increasing worldwide. To address this, environmental regulations are in force worldwide, which seek to control the quality of wastewater discharged to the environment.

* Corresponding author. E-mail: saurabhsdev@gmail.com
https://doi.org/10.2298/JSC250709008S

Treatment of wastewater through biological means has been found to be very promising and the activated sludge process (ASP) is one of the most preferred processes among them. It utilises microorganisms like bacteria to remove contaminants by digesting them. Mathematical models are required for better control of treatment plants so that treated effluent conforms to environmental standards. Additionally, the tuning of operating parameters can be studied more effectively, and alternate control strategies can be developed on computers without the need of actual systems.[1] Simulations of models using operating parameters lead to rapid responses in the event of unforeseen changes in processes.[2]

Artificial intelligence (AI) approaches mimic the human ability to learn and engage in rational problem-solving for better control of complex engineering systems. Artificial neural networks (ANNs) are employed to model the wastewater treatment process due to their high accuracy, the shorter time required for model development and the limited amount of data required.[3] Artificial neural networks require no explicit knowledge of the process or its parameters and develop knowledge through historical observations of input–output data. They learn from examples, and with suitable design, accurate predictions are obtained. However the limitation of an artificial neural network is that it does not extrapolate beyond the range of training data.[4]

In the activated sludge process, many variables are utilized to evaluate plant operation. These variables include biological oxygen demand (*BOD*), chemical oxygen demand (*COD*), total suspended solids (*SS*), pH, *etc*.[5,6] The literature surveyed in this study area has used these variables and found that modelling of sewage treatment plants using artificial neural networks is an effective tool for predicting effluent parameters.[7]

The outcome of this research was to find the best ANN model which represents the activated sludge process in terms of pH, *SS* and *BOD* prediction. The data fluctuated under different seasons and periods of the year. The study was conducted to model STP performance by using soft computing techniques of feed-forward multilayer perceptron artificial neural networks (FFMLP). The main aim was to find the best network structure of the artificial neural network for predicting effluent parameters. Finally, the optimisation of the influent parameters indicates in advance what control actions are necessary to conform to environmental discharge standards.

Artificial neural networks

Model of an artificial neuron. The human brain is a complex structure that is thought to consist of a densely interconnected network of processing units called neurons. It is depicted by the model in Fig. 1, which is referred to as an artificial neuron due to its resemblance to a biological neuron. Artificial neural networks are built on the foundation of this concept.

Hence, the total input I received by the artificial neuron is given as:

$$I = \sum_{1}^{n} w_i x_i + b_i \tag{1}$$

where w_1, w_2, *etc*. are the weights of the input connections, x_1, x_2, *etc*. are the inputs to the artificial neuron and b_i is the bias signal.

The sum is passed into a non-linear filter φ, also known as an activation function or transfer function, to produce the final output, which is given as:

$$Y = \varphi(I) \tag{2}$$

Non-linear statistical data modelling techniques, such as neural networks, are used to identify patterns in data or to represent intricate interactions between inputs and outputs. An ANN is often an adaptive system that modifies its architecture in response to internal or external data passing through the network while it is learning. Put another way, the network learns by experience, and the connections among its components record the knowledge that it gains.[8]

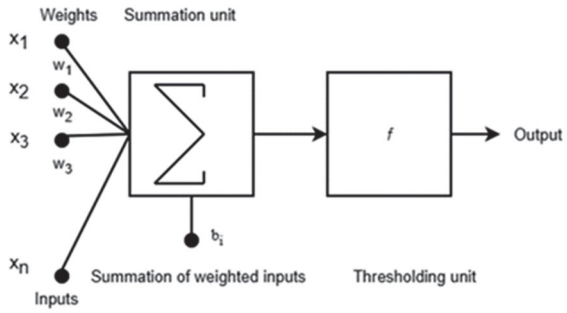

Fig. 1. Model of artificial neuron.

A neural network is made up of layers of neurons with connection weights between them. These layers are called the input layer, hidden layers and the output layer, and the weights between them are called the input-hidden layer weights and the hidden-output layer weights. The network's weights are changed throughout training until it responds within the necessary accuracy limits.[9]

Multi-objective genetic algorithm (MOGA). In single objective function optimisation, we find the best solution, which is usually the global minimum (or maximum). However, most real-world problems involve the simultaneous optimisation of multiple objective functions. In multiple objective function optimisation, there may not be a solution that is the best (global optimum) with respect to all objectives. Instead, there could exist a complete set of optimal solutions that are equally good, called pareto-optimal solutions. A pareto set, for example, for a two-objective function problem, is described by a set of points such that when one moves from one point to any other, one objective function improves, while the other worsens. Since none of the non-dominated solutions in the Pareto set is superior to any other,

any one of them is an acceptable solution. The Pareto front is a set of non-dominated solutions that are equally optimal.

A multi-objective genetic algorithm involves a system whereby an individual's rank corresponds to the number of individuals within the current population by which it is dominated. For the non-dominated solutions, it preserves diversity. Rank--based population sorting is the first phase in a multi-objective genetic algorithm, or MOGA. The individuals who have the highest level of fitness are ranked 1. A rank of 1 is given to every non-dominated individual. A linear function is used to determine an individual's fitness level. Srinivas and Deb (1994) proposed a modified version of the MOGA algorithm, called the non-dominated sorting genetic algorithm (NSGA).[10] All non-dominated individuals are classified into one category. Subsequently, the categorized individuals are eliminated from the population, and a new layer of non-dominated individuals are taken into account. This procedure keeps going until every member of the population has been classified. The people in the first front will receive more copies than the other people since they have the highest fitness value. This eventually leads to convergence and makes it possible to look for non-dominated regions. In this study, NSGA was used to find the pareto front.

EXPERIMENTAL

Description of the study area

The sewage treatment plant is located in a central district of Kerala, India. It commenced its operation in 1970 and has a capacity to treat 5 MLD of water.

The adjacent river receives the process's effluent discharge. The treatment plant uses the activated sludge process, as seen in Fig. 2. It consists of a screen and grit chamber where grit and large particles are removed. After that, the wastewater enters the primary sedimentation tank, which filters out oil, grease and other impurities and provides a uniform liquid for secondary treatment. The organic matter present in the sewage can be effectively removed by secondary treatment.

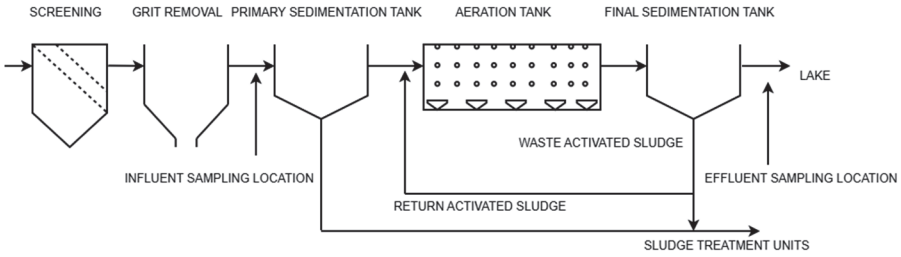

Fig. 2. Schematic of the sewage treatment plant.

An aeration tank and a final sedimentation tank make up the secondary treatment facility, to which the flow next proceeds. To aid waste digestion, diffusers supply oxygen to the mixture of primary wastewater and activated sludge in the aeration tank. After being separated from the treated water in the final settling tank, part of the sludge is transferred to sludge treatment and

disposal, while the remaining part is returned to the aeration tank. After treatment, the water is released into a neighbouring lake. Low *BOD*, low nutrients, low suspended particles and low turbidity are the outcomes of the treatment process.

Data collection and analytical methods

Data pertaining to the sewage treatment plant, collected over a 13-year period, from October 2008 to January 2022, were collected. There were sufficient variations in the influent parameters over the extended period of time. The location after the grit chamber was used to collect the influent parameter data, and the location after the final settling tank was used to collect the effluent data. The parameters were selected according to the rules and regulations in force in the sewage treatment plant. According to the regulations in force in India, it has been specified that for STPs, parameters considered are pH, *BOD*, *SS* and faecal coliform. Of these, effluent pH, *BOD* and *SS* were measured in the plant and were included in the modelling study.

The inputs were pH_{Inf}, oil and grease ($O\&G_{Inf}$) suspended solids (SS_{Inf}) and biochemical oxygen demand (BOD_{Inf}). The output parameters modelled and simulated in this study were pH_{Eff}, suspended solids (SS_{Eff}) and biochemical oxygen demand (BOD_{Inf}), Table I. All parameters were measured according to IS 3025, and a total of 113 data points were collected for this study.[11]

Further data normalising was done according to:

$$Y_{Norm} = (Y - Y_{Min}) / (Y_{Max} - Y_{Min}) \quad (3)$$

where Y is the variable studied, Y_{Max} is the maximum value of the variable, Y_{Min} is the minimum value of the variable and Y_{Norm} is the normalised value of the variable.

TABLE I. Statistical indices of the parameters; pH_{Inf} – pH influent; SS_{Inf} – suspended solids influent; BOD_{Inf} – biochemical oxygen demand influent; $O\&G_{Inf}$ – oil and grease influent; pH_{Eff} – pH effluent; SS_{Eff} – suspended solids effluent; BOD_{Eff} – biochemical oxygen demand effluent; $O\&G_{Eff}$ – oil and grease effluent; Y_{Max} – maximum value of the variable Y; Y_{Min} – minimum value of the variable Y; Y_{Mean} – mean value of the variable Y; C_V – variance; *Sd* – standard deviation; *Med* – median; *Z* – mode; *Sk* – skewness

Parameter	pH_{Inf}	SS_{Inf} mg L^{-1}	BOD_{Inf} mg L^{-1}	$O\&G_{Inf}$ mg L^{-1}	pH_{Eff}	SS_{Eff} mg L^{-1}	BOD_{Eff} mg L^{-1}	$O\&G_{Eff}$ mg L^{-1}
Y_{Max}	6.6	624	937	56	8.2	139	79	8.4
Y_{Min}	5.1	16	42.6	0.8	5.8	4	5.6	0
Sum	801.1	14757	38070	1330	803.9	4457	2344	216.3
Y_{Mean}	7.089	130.59	336.9	11.77	7.11	39.44	20.74	1.91
C_v	31.79	7586	1E+05	85.96	0.24	2067	437.9	360.5
Sd	5.63	87.1	317.1	9.27	0.49	45.46	20.93	18.98
Med	6.58	139	224	9.6	7.15	30	18	1.5
Z	5.9	68	80	6.4	7.2	16	22	0.8
Sk	–0.049	2.024	0.899	2.357	0.504	1.434	3.026	2.513

ANN Modelling strategy

ANN software. Neural network modelling and simulation were carried out using Matlab 9.6 software (version R2019a, MathWorks, Inc., USA). The data were split in the ratio 60:20:20, with 60 % going toward training, 20 % going toward validation and 20 % going toward testing. The application of multilayer perception ANNs (MLP-ANNs) was justified by their ease of coding and simplicity.

ANN training. The available data were divided into three parts. The training set is the first component, and it is used to update the network's weights and biases by calculating the difference between the expected and actual outputs. The validation set, which is the second component, determines when neural network training should end. During training, the training error and validation error are calculated, and it is typically seen that both errors first start to reduce. Nevertheless, training is halted when validation error increases and the network overfit. The network parameters corresponding to the minimum validation error are fixed, and the optimum number of neurons in the hidden layer are returned. The third part of the data is called the testing data tests how the model generalises to new data. Ideally the testing error should be minimal. Overfitting issues can be avoided when there are fewer hidden layer neurons and, thus, fewer network parameters than training data points.[12]

A multi-output model of effluent parameters was implemented for the optimisation study as the entire plant is to be optimised with the three effluent parameters pH, *SS* and *BOD* simultaneously. Also, one hidden layer has been shown to be to be a universal approximator.[13]

The Levenberg–Marquardt (LM) back-propagation algorithm was employed by the ANN network to train its single hidden layer.[13] The backpropagation algorithm adjusts the connection weights and biases by returning the error generated by the neural networks. The LM back-propagation training algorithm is employed in the current study since it is the fastest and converges most quickly.[14] The learning rate parameter, which keeps the network from being stuck in a local minimum instead of a global minimum, is set at 0.01. A trial-and-error procedure was employed to determine the optimal trained model.

ANN training for predicting *BOD*, *SS* and pH is shown in Fig. 3. Eq. (4) for the hyperbolic tangent function is utilised in the hidden layer, while Eq. (5) for the linear activation function is employed in the output layer:[15]

$$f(x) = \frac{2}{1+e^{-2x}} - 1 \tag{4}$$

$$f(x) = x \tag{5}$$

Multi objective optimisation

MOO Software. The Matlab 9.6 (version R2019a) program was utilised to carry out the multi objective optimisation using artificial neural networks, which were then utilised to simultaneously optimise pH, *SS* and *BOD* in the effluent stream.

Initialization. The first step in the algorithm was the creation of an initial population. The algorithm creates the population, or an initial of partial initial population can be provided using the Initial Population Matrix option. The number of individuals in the population was set according to the value of the PopulationSize option. The algorithm evaluates the objective function and constraints for the population, and uses those values to create scores for the population. A snapshot of the Rank histogram, which shows the distribution of individuals in each pareto tier is shown in Fig. 4.

Iterations. The main iteration of the gamultiobj algorithm proceeded as follows.

Select parents for the next generation using the selection function on the current population. The only built-in selection function available for gamultiobj is the binary tournament.

Create children by mutation and crossover from the selected parents.

By calculating their objective function values, children were scored.

The extended population was generated by combining the current population and the children into one matrix.

Rank and crowding distance were calculated for all individuals in the extended population.

By retaining the appropriate number of individuals of each rank, the extended population was reduced to have Population size individuals.

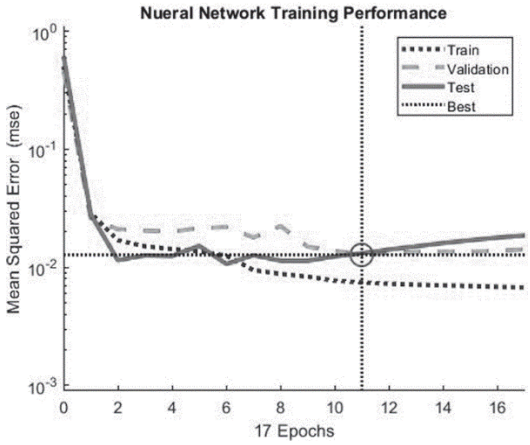

Fig. 3. ANN training.

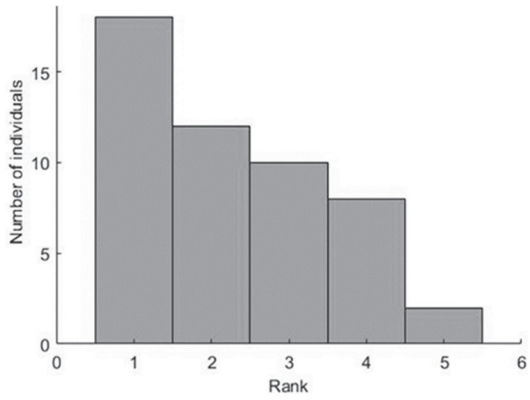

Fig. 4. Rank histogram.

Stopping conditions. The algorithm was terminated when any of the specified termination criteria were met, such as when the maximum number of generations was exceeded or time limit was exceeded.

Effluent regulations

In order to meet the regulatory standards for sewage treatment plants in India, the effluent stream's pH concentration should be between 6.5 and 9, its *SS* concentration should be less than 100 mg L^{-1}, and its *BOD* concentration should be less than 30 mg L^{-1}.

Decision variables for optimisation

The decision variables associated with the process are the influent variables pH, *SS*, *BOD* and *O&G* which were optimised. This study minimised the concentration of pH, *SS* and *BOD* in the effluent and satisfied the regulations on the effluent stream. All the three pollutants are simultaneously minimised.

MOO modelling strategy

The four-input model of pH, *SS*, *BOD* and *O&G* was used to predict the three outputs pH, *SS* and *BOD* simultaneously. The neural network structure is shown in Fig. 5.

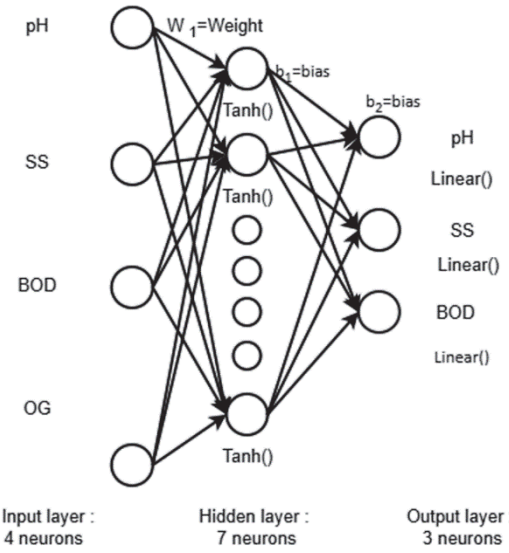

Fig. 5. Neural network for predicting pH, *SS* and *BOD*.

Optimisation strategy

This study's goal was to minimize the effluent stream's pH, *SS*, and *BOD* concentrations while meeting all applicable regulations. The pH, *SS*, *BOD* and *O&G* of the influent stream were the process's decision variables.

The fitness function or objective function consisted of the optimised neural network outputs of pH, *SS* and *BOD*.[16] After entering the variable's upper and lower bounds from Table II, optimisation was initiated. The limits that the regulatory organisations have placed on the effluent quality are the constraints to be fulfilled. To comply with the regulations, the concentration of pH in the effluent stream should be between 6.5 and 9, the concentration of *SS* in the effluent stream should be below 100 mg L^{-1}, the concentration of *BOD* in the effluent stream should be below 30 mg L^{-1} and the concentration of the pollutants should not be negative. Therefore, the concentration of all four pollutants should be greater than zero.

TABLE II. Bounds of the variables; pH_{Inf} – pH influent; SS_{Inf} – suspended solids influent; BOD_{Inf} – biochemical oxygen demand influent; $O\&G_{Inf}$ – oil and grease influent

Decision variable	Lower bound	Upper bound
pH_{Inf}	5.1	8.3
SS_{Inf} / mg L^{-1}	16	624
BOD_{Inf} / mg L^{-1}	42.6	977
$O\&G_{Inf}$ / mg L^{-1}	0.8	56

A penalty term of 134 was added to *SS* and 38 to *BOD* so that the effluent pH, *SS* and *BOD* (objective functions) are all greater than zero.[17] If this is not done objective function values

would yield negative values for *SS* and *BOD*. The output from the software was the optimum influent values of the decision variables pH, SS, *BOD* and *O&G* of the influent stream.

The lower and upper bound values of the decision variables are shown Table II.

RESULTS AND DISCUSSION

Analysis of ANN modelling results

ANN modelling performed well for predicting pH, *SS* and *BOD*. Therefore, the four input model of pH, *SS*, *BOD* and *O&G* was used to predict the three outputs pH, *SS* and *BOD*. The neural network was trained and the network with seven hidden-layer neurons was found to give a correlation coefficient of 0.9207 and an *MSE* of 0.0091, with a training regression of 0.9371, a validation regression of 0.8932, a testing regression of 0.8644 and training *MSE* of 0.0074, validation *MSE* of 0.0128 and testing *MSE* of 0.0131. The regression plots are shown in Fig. S-1 of the Supplementary material to this paper. Literature surveyed on the application of ANN for modelling WWTPs found that the ANN could predict the plant performance in terms of *BOD*, *COD* and *SS* together with a correlation coefficient of 0.903.[6]

MOO Results and siscussion

Pareto front. The three-objective pareto front of pH, *SS* and *BOD* effluents were plotted as shown in Fig. S-2 of the Supplementary material. Also, two-objective pareto fronts of pH_{Eff} and SS_{Eff}, SS_{Eff} and BOD_{Eff} and BOD_{Eff} and pH_{Eff} were plotted in Figs. S3–S5 of the Supplementary material, respectively. It was found that after the 102nd iteration, there was no further improvement in the front.

Plot of decision variables and pH_{Eff}, SS_{Eff} *and* BOD_{Eff}

The optimum values of the decision variables obtained are given in Table III. The optimum influent variables pH, *SS*, *BOD* and *O&G* were determined by employing genetic algorithms resulting in 18 (50×0.35) decision variables as the population size was 50 and the pareto front population fraction was 0.35. The optimum values of the four decision variables are plotted against pH_{Eff} SS_{Eff} and BOD_{Eff} to show the relationship between the variables.[16]

When the decision variables are plotted against pH_{Eff} it was observed that the optimum values of pH_{Inf} varied from 6–8 which were closer to the upper bound values, optimum values of SS_{Inf} varied from 68–380 mg L^{-1}, which were closer to the upper bound values. The optimum values of BOD_{Inf} varied from 155–692 mg L^{-1} and optimum values of $O\&G_{Inf}$ varied from 8–45 mg L^{-1}. Figs. S6–S9 of the Supplementary material show the variation of decision variables with pH_{Eff}.

When the decision variables are plotted against $SS_{Eff.}$, the optimised values of the influent parameters were predominantly concentrated near their respective upper bounds. Specifically, the optimal pH_{Inf} ranged between 6 and 8 and SS_{Inf} ranged from 68 to 380 mg L^{-1}, while BOD_{Inf} varied between 155 and 692 mg L^{-1},

and $O\&G_{Inf}$ ranged from 8 to 45 mg L^{-1}. Figs. S10–S13 of the Supplementary material show the variation of decision variables with SS_{Eff}.

TABLE III. Optimum values of the decision variables. pH_{Inf} – pH influent; SS_{Inf} – suspended solids influent; BOD_{Inf} – biochemical oxygen demand influent; $O\&G_{Inf}$ – oil and grease influent

pH_{Inf}	SS_{Inf} / mg L^{-1}	BOD_{Inf} / mg L^{-1}	$O\&G_{Inf}$ / mg L^{-1}
6.0109	73.5756	244.8432	16.6149
6.6443	265.7488	692.2355	7.9727
8.0089	379.6842	263.4342	18.3982
6.6822	256.6529	683.3599	9.2286
5.7030	158.3825	680.4012	10.4858
6.5795	167.5787	674.3457	10.2858
7.0111	81.5747	217.7412	15.9524
6.6225	185.6128	680.6632	9.9630
5.9477	252.6379	683.367	9.4305
6.7325	217.2645	209.909	13.6525
6.2953	77.8575	202.5866	18.8731
6.8540	334.2789	294.5785	18.0587
6.3737	67.4801	155.2362	45.4133
6.6313	205.9524	206.6183	16.0169
7.8411	353.9885	245.7956	17.1385
6.8289	285.1475	543.4304	10.0868
6.3881	67.5123	155.1961	45.3586
6.0075	173.3748	598.5686	11.3049

When the four-decision variables are plotted against BOD_{Eff}, the optimised influent parameter values were found to cluster predominantly near the upper limits of their respective ranges in the case of pH_{Inf} where it ranged between 6 and 8 and SS_{Inf} where it ranged from 68 to 380 mg L^{-1}. BOD_{Inf} lied between 155 and 692 mg L^{-1}, and $O\&G_{Inf}$ values varied from 8 to 45 mg L^{-1}. Figs. S14–S17 of the Supplementary material show the variation of decision variables with BOD_{Eff}.

From the literature surveyed, it was found that the optimal values of pH_{Inf} ranged between 7.8–8.1, the optimal values of BOD_{Inf} varied between 175–475 mg L^{-1}, the optimal values of SS_{Inf} lay close to 850 mg L^{-1} when *BOD*, *SS* and total phosphorous *TP* were minimised simultaneously.[16]

CONCLUSIONS

Artificial neural networks were found to model the complex nonlinear process occurring in sewage treatment plants. The model developed in the research work was found to predict effluent pH, *SS* and *BOD* with a correlation coefficient value of 0.9207.

Multi-objective optimisation was proposed to minimise the concentration of pollutants pH, *SS* and *BOD* in the effluent stream in the STP. A genetic algorithm was employed to minimise the concentration of pH, *SS* and *BOD* simultaneously in the effluent stream.

The goal of this research work was to find the optimum values of the decision variables that satisfy the objectives and constraints. The decision variables involved in this process are the pH, *SS*, *BOD* and *O&G* in the influent stream. The constraints imposed are in accordance with the regulatory requirements for the effluent quality of treated wastewater. It was observed that optimum values of the decision variables pH_{Inf} lay between 6–8, the optimum values of SS_{Inf} lay between 68–380 mg L^{-1}, the optimum values of BOD_{Inf} lay between 155–692 mg L^{-1} and the optimum values of $O\&G_{Inf}$ lay between 8–45 mg L^{-1}, when all the effluent concentrations are minimised simultaneously.

SUPPLEMENTARY MATERIAL

Additional data and information are available electronically at the pages of journal website: https://www.shd-pub.org.rs/index.php/JSCS/article/view/13454, or from the corresponding author on request.

ИЗВОД

МОДЕЛОВАЊЕ И ОПТИМИЗАЦИЈА ПРОЦЕСА АКТИВНОГ МУЉА ПРИМЕНОМ ВЕШТАЧКИХ НЕУРОНСКИХ МРЕЖА И ГЕНЕТСКИХ АЛГОРИТАМА

SAURABH SAHADEV[1], GUPTA MADHU[2] и ROY M. THOMAS[2]

[1]*Department of Chemical Engineering, Government Engineering College, Thrissur, Kerala, India и* [2]*School of Engineering, Cochin University of Science and Technology, Kochi, Kerala, India*

Математичко моделовање процеса активног муља спроведено је коришћењем вишеслојних перцептронских неуронских мрежа у циљу предвиђања параметара квалитета излазне воде, док је вишециљни генетски алгоритам примењен за оптимизацију параметара улазне воде како би се минимизовала концентрација загађујућих материја у излазном току. Математичко моделовање је извршено коришћењем података постројења за пречишћавање отпадних вода из централног округа јужне савезне државе Индије. Испитивани параметри излазне воде су pH вредност, концентрација суспендованих материја и биохемијска потрошња кисеоника, док су параметри улазне воде који се оптимизују pH вредност, концентрација суспендованих материја, биохемијска потрошња кисеоника и садржај уља и масти. Модел је евалуиран на основу статистичких параметара коефицијента корелације и средње квадратне грешке. За моделовање и оптимизацију коришћен је Matlab R2019a. Утврђено је да су pH, концентрација суспендованих материја и биохемијска потрошња кисеоника излазне воде предвиђени са укупним коефицијентом корелације од 0,9207 и средњом квадратном грешком од 0,0091. Током оптимизације параметара улазне воде установљено је да се оптималне вредности променљивих крећу у опсегу: pH 6–8, концентрација суспендованих материја 68–380 mg L^{-1}, биохемијска потрошња кисеоника 155–692 mg L^{-1}, садржај уља и масти 8–45 mg L^{-1}, у случају истовременог минимизовања функција циља.

(Примљено 9. јула, ревидирано 20. августа 2025, прихваћено 18. фебруара 2026)

REFERENCES

1. T. Y. Pai, P. Y. Yang, S. C. Wang, M. H. Lo, C. F. Chiang, J. L. Kuo, H. H. Chu, H. C. Su, L. F. Yu, H. C. Hu, Y. H. Chang, *Appl. Math. Model.* **35** (2011) 3674 (https://dx.doi.org/10.1016/j.apm.2011.01.019)

2. V. V. Nair, H. Dhar, S. Kumar, A. K. Thalla, S. Mukherjee, J. W. C. Wong, *Bioresour. Technol.* **217** (2016) 90 (https://dx.doi.org/10.1016/j.biortech.2016.03.046)
3. V. Pareek, M. P. Brungs, A. Adesina, R. Sharma, *J. Photochem. Photobiol., A* **149** (2002) 139 (https://dx.doi.org/10.1016/S1010-6030(01)00640-2)
4. N. J. De Vos, T. H. M. Rientjes, *Hydrol. Earth Syst. Sci.* **9** (2005) 111 (https://dx.doi.org/10.5194/HESS-9-111-2005)
5. M. M. Hamed, M. G. Khalafallah, E. A. Hassanien, *Environ. Model. Software* **19** (2004) 919 (https://dx.doi.org/10.1016/j.envsoft.2003.10.005)
6. M. S. Nasr, M. A. E. Moustafa, H. A. E. Seif, G. El Kobrosy, *Alexandria Eng. J.* **51** (2012) 37 (https://dx.doi.org/10.1016/j.aej.2012.07.005)
7. M. Hamada, H. A. Zaqoot, A. A. Jreiban, *J. Appl. Res. Water Wastewater* **9** (2018) 399 (https://dx.doi.org/10.22126/arww.2018.874)
8. M. Arbib, M. Bota, *Neural Networks* **16** (2003) 1237 (https://dx.doi.org/10.1016/j.neunet.2003.08.002)
9. D. Howard, B. Mark, *Neural Network Toolbox User's Guide*, 2004
10. N. Srinivas, K. Deb, *Evol. Comput.* **2** (1994) 221 (https://dx.doi.org/10.1162/evco.1994.2.3.221)
11. IS 3025-1: *Methods of sampling and test (physical and chemical) for water and wastewater Part 1*, 1987
12. R. Rustum, *Modelling Activated Sludge Wastewater Treatment Plants Using Artificial Intelligence Techniques (Fuzzy Logic and Neural Networks)*, Heriot-Watt University School, Edinburgh, 2009
13. K. Hornik, M. Stinchcombe, H. White, *Neural Networks* **2** (1989) 359 (https://doi.org/10.1016/0893-6080(89)90020-8)
14. F. S. Mjalli, S. Al-Asheh, H. E. Alfadala, *J. Environ. Manage.* **83** (2007) 329 (https://dx.doi.org/10.1016/j.jenvman.2006.03.004)
15. S. Haykin, *Neural Network-A Comprehensive Foundation*, 2nd ed., Pearson Education, New Delhi, 1999
16. N. Kaur, *Modeling and multi-objective optimization of wastewater treatment process*, University of Western Ontario, Electronic Thesis and Dissertation Repository, 2023, 9146 (https://ir.lib.uwo.ca/etd/9146)
17. Ö. Yeniay, *Math. Comput. Appl.* **10** (2005) 45 (https://dx.doi.org/10.3390/mca10010045).

Journal of the Serbian Chemical Society
JSCS@tmf.bg.ac.rs • www.shd.org.rs/JSCS
J. Serb. Chem. Soc. 91 (4) S131–S134 (2026) *Supplementary material*

SUPPLEMENTARY MATERIAL TO

Modelling and optimisation of activated sludge process using artificial neural networks and genetic algorithms

SAURABH SAHADEV[1]*, GOPAL MADHU[2] and ROY M. THOMAS[2]

[1]*Department of Chemical Engineering, Government Engineering College, Thrissur, Kerala, India and* [2]*School of Engineering, Cochin University of Science and Technology, Kochi, Kerala, India*

J. Serb. Chem. Soc. 91 (4) (2026) 399–410

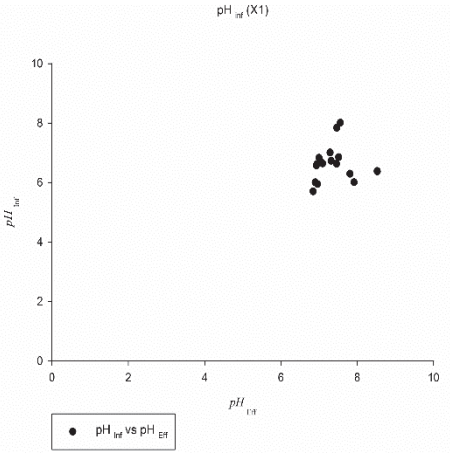

Fig. S-1. Relationship between pH_{Inf} and pH_{Eff}

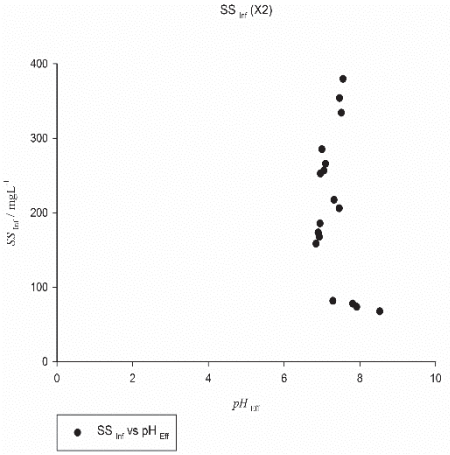

Fig. S-2. Relationship between SS_{Inf} and pH_{Eff}

* Corresponding author. E-mail: saurabhsdev@gmail.com

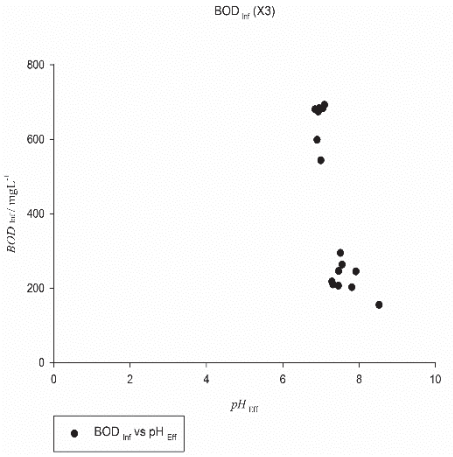

Fig. S-3. Relationship between BOD_{Inf} and pH_{Eff}

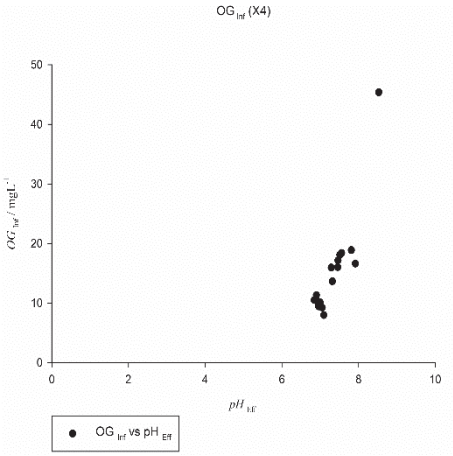

Fig. S-4. Relationship between $O\&G_{Inf}$ and pH_{Eff}

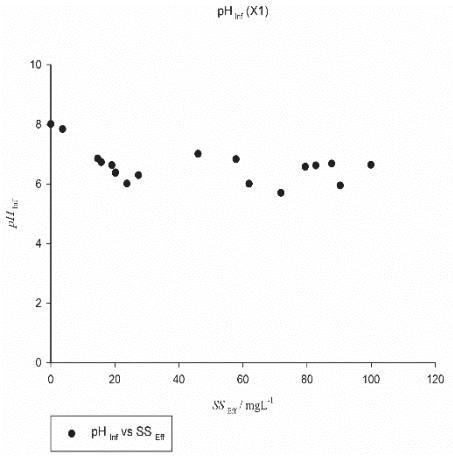

Fig. S-5. Relationship between pH_{Inf} and SS_{Eff}

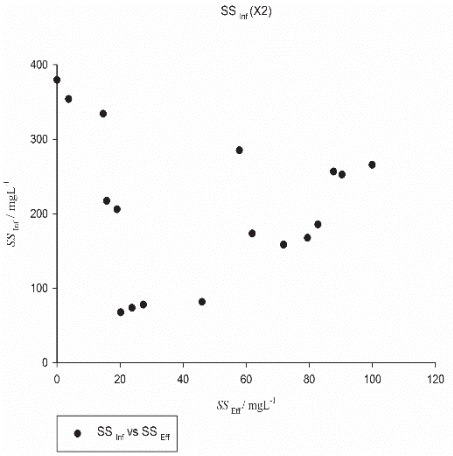

Fig. S-6. Relationship between SS_{Inf} and SS_{Eff}

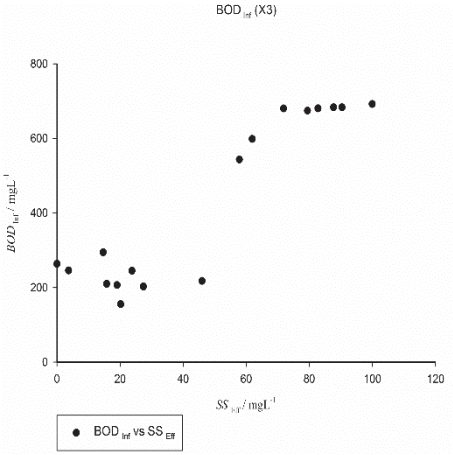

Fig. S-7. Relationship between BOD_{Inf} and SS_{Eff}

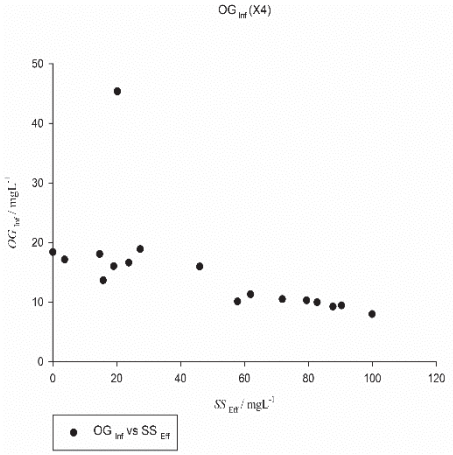

Fig. S-8. Relationship between $O\&G_{\text{Inf}}$ and SS_{Eff}

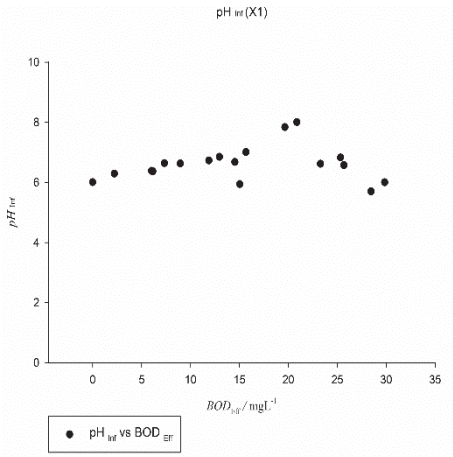

Fig. S-9. Relationship between pH_{Inf} and BOD_{Eff}

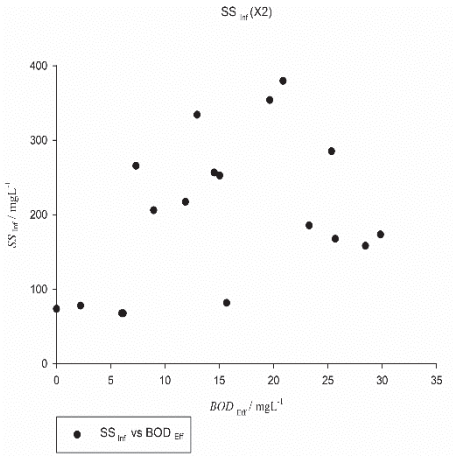

Fig. S-10. Relationship between SS_{Inf} and BOD_{Eff}

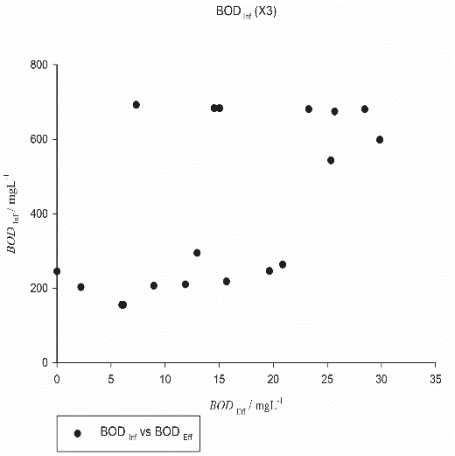

Fig. S-11. Relationship between BOD_{Inf} and BOD_{Eff}

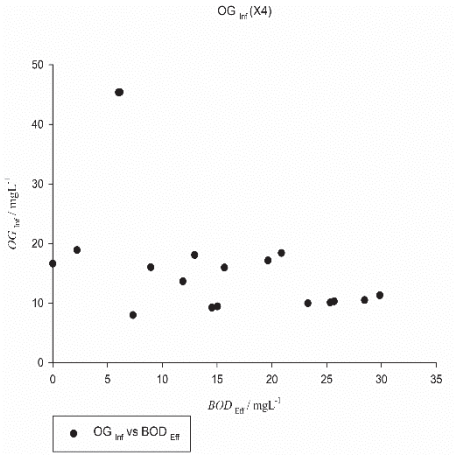

Fig. S-12. Relationship between $O\&G_{Inf}$ and BOD_{Eff}

Journal of the Serbian Chemical Society
JSCS-info@shd.org.rs • www.shd.org.rs/JSCS
J. Serb. Chem. Soc. 91 (4) 411–423 (2026)
JSCS–5500
Original scientific paper
Published 1 May, 2026

Seasonal influence on suitability of masquerade tree as a bioindicator of vehicular pollution along University of Ilorin Road, Nigeria

MOJEED O. BELLO[1]*, NASIRU ABDUS-SALAM[1], LATEEF A. IBRAHIM[1], TAOHEED O. BELLO[2], ABUBAKAR AREMU[3] and ABIDAH O. MUHAMMED[1]

[1]*Department of Chemistry, University of Ilorin, P.M.B. 1515, Ilorin, Nigeria,* [2]*Department of Natural Sciences and Mathematics, College of Arts and Sciences, William V. S. Tubman University, P. O. Box 3570, Harper City, Maryland County, Liberia and* [3]*National Oil Spill Detection and Response Agency, P.M.B. 145, Abuja, Nigeria*

(Received 2 January, revised 28 March 2025, Accepted 5 January 2026)

Abstract: This study focused on the seasonal impacts on the suitability of masquerade (*Polyalthia longifolia*) as a bioindicator of vehicular pollutants. Some leaves of the tree were plucked along the roadside and from a control site with no vehicular emissions. Biochemical parameters, including pH, ascorbic acid content, relative water content, total chlorophyll and air pollution tolerance index (*APTI*), were determined in both dry and wet seasons using standard methods. Potentially toxic elements (PTEs) commonly associated with automobile pollutants (Pb, Zn, Cr, Mn, Fe and Cu) were analyzed using atomic absorption spectroscopy, after acid digestion. The concentrations of PTEs were slightly higher in leaves from roadside masquerade tree than in those from the control site, except for Cr and Cu at some sampling points during the wet season. The biochemical properties in the roadside samples indicated the presence of pollutants compared to the control site in both seasons. *APTI* of the roadside samples showed higher sensitivity (mean value = 10.30) in the dry season, indicating a gradual loss in tolerance to pollution; however, a slight increase (mean value = 11.23) in tolerance was observed in the wet season. The masquerade tree demonstrated its sensitivity to vehicular pollution in both seasons. It is more sensitive in the dry season but tends to tolerate pollutants in the wet season by increasing *APTI* through improved defense mechanisms.

Keywords: bioindicator; vehicular pollution; masquerade tree; potentially toxic elements.

* Corresponding author. E-mail: bello.mo@unilorin.edu.ng
https://doi.org/10.2298/JSC250202009B

INTRODUCTION

High levels of vehicular pollution are a common problem in urban areas, which can harm public health and air quality.[1] This is a consequence of using low--quality fuel, old and poorly maintained cars on the road,[2] and some other processes as friction between tyres and the road surface.[3,4] Air pollution through vehicular activities generates a lot of pollutants such as oxides of carbon (CO and CO_2), nitrogen (NO_x), sulphur (SO_x), polyaromatic hydrocarbons (PAHs) and potentially toxic elements.[5] This menace of air pollution needs immediate and long-term monitoring and mitigation as it has both direct and indirect effects on human health and the environment.

One potential approach to monitoring and mitigating this pollution is the use of bioindicators or living organisms, that can serve as sensitive indicators of environmental conditions or sinks for pollutants. Two major sinks of pollutants are plants and soil.[5,6] Air pollution is among the many environmental challenges that plants, a lovely gift from nature, can help mitigate.[7] Most air pollutants are deposited on the plants' leaves and are removed through stomata on their surfaces.[8,9]

Several trees and plants have reportedly been used as bioindicators in many urban cities worldwide to monitor levels of air pollution caused by vehicular emissions and other activities, such as industrial discharges. Different plant species exhibit varying levels of sensitivity and tolerance to different forms of air pollution.[6] Bello *et al.*[10] reported the utilization of Mexican sunflower (*Tithonia diversifolia*) for monitoring air pollution around the iron smelting industry and the study concluded that there was an impact of the industry on the plant. For vehicular emission, *Polyalthia longifolia* (masquerade tree), *Caesalpinia pulcherrima* (peacock flower or barbados pride tree), *Delonix regia* (flamboyant tree), *Tamarindus indica* (tamarind tree), *Terminalia catappa* (tropical almond tree), *Mangifera indica* (mango tree), *Ficus platyphylla* (broad-leaved fig tree), *Ficus benghalensis* L. (banyan tree), *Azadirachta indica A. Juss* (neem tree), *Ficus religiosa* L. (bodhi tree), *Ficus benjamina* L. (as weeping fig tree) and *Bougainvillea glabra* (paper flower tree) that were exposed to roadside automobile pollution, stress was reported.[2,5,9] The air pollution tolerance index (*APTI*) is typically used to assess how sensitive and tolerant certain plants are to air pollution.[6,11] A measure of pH, ascorbic acid content (*AAC*), relative water content (*RWC*) and total chlorophyll in the leaves of a particular tree is used to determine how plants respond to pollution.[9] Plants that are sensitive to pollutants are used as indicators, while those that are tolerant consume the pollutant and reduce the level of pollution in the environment.[11,12]

Masquerade trees (*P. longifolia*), among others, have been widely studied as bioindicators of vehicular emissions. No wonder it is planted along the main road leading into the University of Ilorin's campus in Nigeria. This tall, evergreen tree native to tropical Asia is also known as the Indian mast tree.[13] Various positions have been taken on its application as a bioindicator. Kirthika and Vishnuprasad[14]

reported that it has an intermediate tolerance to vehicular pollution based on its *APTI* value. Its potential as a bioindicator of vehicular pollutants was also related to its ability to accumulate potentially toxic elements.[15] Similarly, Umar *et al.*[16] stated that *P. longifolia* has the highest dust-carrying capacity among the studied plant species, indicating its potential as a bioindicator of vehicular pollution. Also, Azam *et al.*[17] reported that it is less sensitive to vehicular pollution than the other trees used in their study, based on *APTI* values.

According to the existing research, the masquerade tree is a viable bioindicator for tracking air pollution and vehicle emissions in urban environments. However, there is little or no information on the effect of seasons on its efficiency in response to pollution. Therefore, this present study investigated the effect of seasonal conditions on its ability to serve as a bioindicator of vehicular pollutants.

EXPERIMENTAL

Description of study area

The University of Ilorin (Better by Far), also known as Unilorin, is a federal government-owned University located in Ilorin, Kwara State, Nigeria. The institution has a large landmass of approximately 15,000 ha and is situated in the southern part of the city. The University, with approximately 3,040 staff and 34,999 students, experiences a high number of vehicles plying the road from the gate to the campus, especially the University's main car park. The dry and wet seasons are the two main seasons in the region. The dry season covers November and April of the following year. The wet season lasts between April and October.

Sample collection

Leaf samples of masquerade tree (*P. longifolia*) were collected in January (dry season) and May (wet season), 2023. These sites were the University roadsides from the Fountain roundabout towards the gate and walkways (control site). Four samples were collected from the roadside at the following coordinates: 8.47650°N 4.67212°E (RS1), 8.47617°N 4.67182°E (RS2), 8.47556°N 4.67165°E (RS3) and 8.47499°N 4.67100°E (RS4). The control sample was taken at 8.48105°N, 4.67400°E. The samples were collected in a sealed, air-tight bags.

Determination of potentially toxic elements (PTEs) concentration

A 20 mL of an aqua regia solution (15 mL 37 % HCl and 5 mL 65 % HNO_3) was added to 1 g of the finely ground leaf samples in the digestion beaker. This solution was then heated using a hot plate until it became transparent. The heating process then continued for an additional 20 min, after which deionized water (50 mL) was added. The mixture was filtered into a 100 mL standard flask using a funnel and Whatman filter paper. The content was brought up to the 100 mL mark and stored in a sample bottle for PTEs analysis.[18] Concentrations of selected PTEs (Pb, Zn, Cr, Mn, Fe and Cu) were analyzed in the samples using a Buck Scientific Accusys 230 atomic absorption spectrophotometer.

pH measurement

The pH of the leaves was determined using a slightly modified method reported by Pandey *et al.*[19] Here, 5 g of the leaves were crushed and homogenized with a pestle and mortar. It was mixed thoroughly for 5 min with 10 mL of distilled water. Then, the mixture was separated by centrifugation and the supernatant obtained was subjected to pH estimation using a digital tabletop pH meter (Watson pH-2602).

*Relative water content (*RWC*)*

1 g of fresh masquerade tree leaves was accurately weighed and immersed in water for 12 h. The fully hydrated weights of the leaves were measured after they were saturated with water. The leaves were further dried in an oven (Gallenkamp OV-160) at 105 °C overnight, and their dry weight was subsequently measured. Then the *RWC* (%) was calculated as:

$$RWC(\%) = \frac{F - D}{T - D} \times 100 \quad (1)$$

where F is the weight (g) of the fresh leaves; T is the hydrated weight (g) and D is the dry weight (g) at 105 °C.[11,20]

*Ascorbic acid content (*AAC*)*

The *AAC* in each sample was quantified and expressed as mg per 100 g using a slightly modified method of Vahid.[21] 10 g of the leaves were blended with a 4 % oxalic acid solution, and the volume was made up to 100 mL using the same 4 % oxalic acid solution. The solution was then filtered as an extract using a 110 mm grade 1 Whatman filter paper. A 5 mL aliquot of the sample extract was titrated with a standardized solution of 2,6-dichlorophenolindophenol (dye). The *AAC* was then calculated as:

$$AAC(\text{mg } (100 \text{ g}^{-1})) = 100 \frac{\text{Dye factor} \times 100 V_2}{V_1 W} \quad (2)$$

where W is the weight (g) of a sample taken for extraction with oxalic acid; V_1 is the volume (mL) of sample extract taken for titration and V_2 is the volume (mL) of dye required (titer value). The dye factor was calculated from the standardization of the dye solution.

*Total chlorophyll (*TCh*)*

50 mg of the fresh leaves were crushed and added to a vial containing 7 mL of dimethyl sulfoxide (DMSO), and then incubated at 65 °C for 30 min. The mixture was centrifuged, separated into 10 mL standard and then made up to 10 mL with DMSO. The sample was analyzed using a spectrophotometer (VWR UV-6300PC) at wavelengths of 648 and 665 nm, with a blank as a reference. Then the *TCh* was calculated as:

$$TCh(\text{mg g}^{-1}) = \frac{20.34 A_{648} + 7.49 A_{665}}{1000 W} V \quad (3)$$

where V is the initial volume of extract; W is the weight of the sample taken; A_{648} and A_{665} are the optical density (*OD*) values measured at 648 and 665 nm, respectively. 20.34 and 7.49 are the absorption coefficients. [22]

*Air pollution tolerance index (*APTI*)*

APTI of the tree was calculated using the expression: [23]

$$APTI = \frac{AAC(TCh + \text{pH}) + RWC}{10} \quad (4)$$

Statistical analysis

For each sampling point and season, the mean values of each biochemical property, along with their standard deviations, are presented. Using Microsoft Excel 2016 Tool Packs for Data analysis, the relationship between biochemical properties and the *APTI* was analyzed using correlation analysis.

RESULTS AND DISCUSSION

Concentration of potentially toxic elements (PTEs)

The concentration of PTEs in the leaves of the masquerade tree from the four sampling points (RS1–RS4) and that of the control site (CS) are presented in Table I for dry and wet seasons.

TABLE I. Concentration of potentially toxic elements (mg L^{-1}) in the masquerade leaves during dry and wet season; ND means not detected

Site	Element					
	Pb	Zn	Cr	Mn	Fe	Cu
			Dry season			
RS1	0.086	0.278	0.054	0.469	1.533	0.116
RS2	0.036	0.371	0.052	0.505	1.615	0.121
RS3	0.055	0.341	0.052	0.512	1.445	0.105
RS4	0.099	0.210	0.048	0.287	1.747	0.107
Mean±*SD*	0.069±0.02	0.30±0.06	0.052±0.002	0.443±0.09	1.585±0.11	0.112±0.01
CS	0.023	0.108	0.047	0.163	0.866	0.062
			Wet season			
RS1	0.047	0.623	0.032	0.558	2.511	0.051
RS2	0.087	0.520	0.038	0.492	2.578	0.089
RS3	0.048	1.221	0.040	0.409	1.604	0.058
RS4	0.046	1.832	0.084	0.297	1.836	0.012
Mean±*SD*	0.057±0.02	1.049±0.53	0.0489±0.02	0.439±0.10	2.132±0.42	0.053±0.03
CS	ND	0.301	0.044	0.272	0.384	0.109

It is observed that all selected PTEs, which are usually associated with vehicular emissions, are present in roadside samples. Their presence in the control sample is lower, except for chromium, which showed a slightly higher concentration in the CS than in the three RS (RS1, RS2 and RS3) and copper, which had a higher concentration in the CS than in all the RS samples during the wet season. This exception may be due to the high mobility of the metal ions during the wet season. Similarly, stormwater containing PTEs from various sources can be readily deposited and may affect the control sample.[24,25] Interestingly, a major PTE (Pb) attributed to vehicular emissions was not detected in the CS during the wet season. Additionally, the leaves of the plant from RS1 to RS4 recorded significantly higher values of potentially toxic elements than those of the CS in the dry season. The observation is justified by the plant's proximity to the road and the long accumulation of dust containing these potentially toxic elements on its leaves, which prevents rainwater from washing it away.

The mean concentrations of the potentially toxic elements from the roadside sampling points RS1–RS4 are more than the control site (CS) except copper in the wet season. The presence of potentially toxic elements in such amounts (higher

than those at the control site) is likely due to contamination of the ambient environment by vehicular emissions. The presence of PTEs in uncontaminated environmental media (air, soil and water) is not unlikely, but vehicular emissions are a significant source in urban environments. These metallic elements originate from various car parts and operations, including fuel combustion, tyre friction, brake wear and road surface abrasion.[3,4]

*Biochemical properties and air pollution tolerance index (*APTI*)*

This section presents the results on biochemical properties and the computed *APTI*. These biochemical parameters include ascorbic acid content, pH, relative water content and total chlorophyll content of the tree's leaves. The results for each roadside sample point RS1–RS4 are compared with those of the control site (CS).

pH. The pH value of the leaves of the masquerade tree from the four roadside sampling points RS1–RS4 along the road with the University of Ilorin, and that of the control site (CS) are presented in Table II.

TABLE II. pH of the leaves from the masquerade tree at the roadside (RS) and control site (CS) samples

Season	Sampling point					
	RS1	RS2	RS3	RS4	Mean±*SD*	CS
Dry	6.47	6.44	6.45	6.49	6.46±0.02	6.53
Wet	7.05	6.75	6.78	6.97	6.89±0.13	7.14

It is observed that all the samples, including the control, are slightly acidic in the dry season. Although the control site (CS) is less acidic (pH 6.53) compared to the individual roadside samples and their mean value (pH 6.46). The tree recorded higher pH levels during the wet season than in the dry season, with the highest value of 7.14 at the control site and the lowest value of 6.75 at RS2, which can be approximated to 7.0. An acidic pH indicates that NO_x and SO_x are present in the air, and their presence can be attributed to vehicular emissions from the burning of fossil fuels.[26,27] Plant health and soil composition are greatly impacted by acid rain, which is brought on by SO_x and NO_x emissions in the atmosphere.[28] It lowers the pH of rainwater below 5.6 and consequently affects the photosynthetic processes, influencing plant development, productivity, and yield.[28,29] It induces oxidative stress by generating reactive nitrogen species (RNS) when it reacts with reactive oxygen species (ROS) and damages lipids, proteins and nucleic acids.[30] Plants with a pH of around 7.0 are tolerant.[27] In this study, the pH level of the masquerade tree's leaves from a less polluted control site (CS) is 7.14, indicating that the tree is naturally (without pollution) air pollution-tolerant plant.

*Relative water content (*RWC*)*

The results of the *RWC* are presented in Table III. The highest value was observed in the control sample, at 97.88 and 98.21 % in the dry and wet seasons, respectively.

TABLE III. Relative water content (%) of the leaves from the masquerade tree at the roadside (RS) and control site (CS) samples

Season	Sampling point					
	RS1	RS2	RS3	RS4	Mean±*SD*	CS
Dry	94.39	94.89	96.13	91.24	94.16±1.80	97.88
Wet	96.26	96.48	97.84	94.31	96.22±1.26	98.21

However, all selected locations showed a significant *RWC* value. *RWC* of a leaf represents the water it retains compared to its fully turgid state and serves as a crucial indicator of plant response to pollution. Although the wet season affects the plant, the *RWC* of the roadside sample is still lower than that of the control site in the dry season. The result indicates roadside pollution, as plant *RWC* is reduced in contaminated environments. In stressful situations, such as exposure to air pollution, when transpiration rates are often high, a plant's high water content aids in maintaining its physiological equilibrium. [31] Plants with high relative water content under polluted conditions may be tolerant to pollutants.

*Ascorbic acid content (*AAC*)*

The *AAC* of tree leaves is a major biochemical property that is strongly affected by vehicular pollution, along with other factors such as chlorophyll content. The results of the ascorbic acid content in the leaves of the masquerade tree, in this study, are presented in Table IV.

TABLE IV. Ascorbic acid content (mg g^{-1}) of the leaves from the masquerade tree at the roadside (RS) and control site (CS) samples

Season	Sampling point					
	RS1	RS2	RS3	RS4	Mean±*SD*	CS
Dry	1.056	1.036	1.023	1.234	1.087±0.08	0.99
Wet	1.538	1.386	1.564	1.736	1.556±1.02	1.367

The results of the study revealed that the masquerade tree recorded its lowest ascorbic acid content at the control site compared to the individual roadside sampling points RS1–RS4 and their mean values in both the dry and wet seasons. The higher *AAC* observed at the roadside sampling point is likely due to their biochemical response to stress caused by pollution.[32,33] The tree maintains higher ascorbic acid levels under polluted conditions, indicating its tolerance to air pollutants.

However, the *AAC* was higher at all sampling points, including the control site, during the wet season compared to the dry season.

*Total chlorophyll content (*TCh*)*

The highest *TCh* was observed at one of the roadside sampling sites, RS1, at 2.839 and 3.448 mg g^{-1} for the dry and wet seasons, respectively (Table V). However, the mean values in both seasons are lower than those at the control site. The lower total chlorophyll value in the roadside samples (mean value) compared with the control site indicates the impact of automobile pollutants on the plant.

Iqbal *et al.*[32] reported that elevated levels of automobile pollution reduce chlorophyll content in plants growing near roadways. However, chlorophyll content in plants varies based on species, leaf age, pollution levels and various biotic and abiotic factors.[35] Vehicular pollutants like SO_2, NO_x and O_3 react with the leaf's chloroplast and consequently decrease the chlorophyll content.[36]

TABLE V. Chlorophyll content (mg g^{-1}) of the leaves from the masquerade tree at the roadside (RS) and control site (CS) samples

Season	Sampling point					
	RS1	RS2	RS3	RS4	Mean±*SD*	CS
Dry	2.839	1.387	1.024	1.643	1.723±0.68	2.396
Wet	3.448	1.749	2.153	2.538	2.472±0.62	3.232

*Air pollution tolerance index (*APTI*)*

The *APTI* of the masquerade tree from the roadside (RS) and control site (CS) are presented in Table VI. The results obtained from all the roadside sampling points RS1–RS4 and control site (CS) compared with the *APTI* categories (Table VII) reported by Lakshmi *et al.*[12] suggested that the plant is sensitive to air pollutants. It is observed that the masquerade tree is sensitive to air pollution levels along the University's roadside.

TABLE VI. The *APTI* of the masquerade tree from the roadside sampling points (RS) and the control site (CS)

Sampling point	Season	
	Dry	Wet
RS1	10.42	11.24
RS2	10.29	10.83
RS3	10.38	11.18
RS4	10.13	11.08
CS	10.67	11.24

The seasonal effect showed that its sensitivity is marginally higher during the dry season compared to the wet season. A plant's ability to mitigate air pollution is indicated by its *APTI*, where higher index values signify greater tolerance.[37] It

is an index for determining how plants react biochemically and physiologically to environmental conditions. Pollution-sensitive plants aid in detecting pollution, whereas tolerant plants serve as sinks in polluted areas to help reduce pollution.[11,12]

TABLE VII. *APTI* categories

Category	*APTI* value range
Tolerant species	30–100
Intermediate-tolerant species	17–20
Sensitive species	1–16
Very sensitive species	< 1

The correlations between biochemical properties and *APTI* for the dry and wet seasons are presented in Table VIII. A significant positive correlation (r = 0.8450) was observed between the plant's *RWC* and *APTI* during the dry season. During the wet season, the relationship is weak, although positive (r = 0.1322). A positive correlation between *APTI* and *RWC* was reported by Punit and Rai.[36] Other factors, such as leaf thickness and soil moisture, also affect the relative water content, even in the presence of pollutants. The total chlorophyll of the leaves also showed a weak but positive correlation (r = 0.3132) in the dry season, but a strong positive correlation (r = 0.7776) in the wet season. The amount of chlorophyll in plants' leaves varies depending on the species, age, season, drought stress and pollution level.[8,38] Other parameters, pH (r = –0.5556) and *AAC* (r = –0.88722), indicated a negative relationship with *APTI* in the dry season. This result implies that the lower pH and *AAC* observed in the tree leaves correlated with higher sensitivity (lower *APTI*). The result is likely due to higher levels of vehicular pollutant dust during the season. Reports have shown that *APTI* values generally decrease (with higher sensitivity) in polluted areas with lower pH and *AAC* compared to control sites.[7,39] However, moderate positive correlations were found between the pH and *APTI*

TABLE VIII. Correlation between biochemical properties and APTI during dry and wet season

Parameter	pH	*RWC* / %	*AAC* / mg g^{-1}	*TCh* / mg g^{-1}	*APTI*
Dry season					
pH	1				
RWC / %	–0.86411	1			
AAC / mg g^{-1}	0.876296	–0.97247	1		
TCh / mg g^{-1}	0.429714	–0.23069	0.06662	1	
APTI	–0.5556	0.845035	–0.88722	0.313231	1
Wet season					
pH	1				
RWC / %	–0.56025	1			
AAC / mg g^{-1}	0.549513	–0.60149	1		
TCh / mg g^{-1}	0.938304	–0.24072	0.367135	1	
APTI	0.631617	0.132173	0.522431	0.776754	1

(r = 0.6316) and between *AAC* and *APTI* (r = 0.5224) in the wet season. Consequently, the increase in pH and *AAC* with increasing *APTI* value tends to reduce sensitivity and improve tolerance, suggesting a defence mechanism against air pollutants.

CONCLUSION

This study focused on the seasonal impact on the suitability of the masquerade (*P. longifolia*) as a bioindicator of vehicular pollutants along the University of Ilorin Road. The results of potentially toxic elements and biochemical properties at the roadside sampling points (RS1–RS4) compared with the control site (CS) indicated the presence of air pollution during both dry and wet seasons. The seasonal effect on the plant is not significant since the values are much closer to 7 in both seasons. The roadside masquerade trees can be considered pollution-tolerant due to their high ascorbic acid content, especially during the wet season. The relative water content was high in both seasons, but higher at the control site and in the wet season than at the roadsides and in the dry season. The plant's leaves showed the highest total chlorophyll content during the wet season. The *APTI* values in both seasons suggest that the plant is sensitive to air pollutants. Consequently, the overall conclusion is that the masquerade tree is sensitive to vehicular pollutants in both seasons, making it a suitable bioindicator. However, there was a reduction in sensitivity, resulting in improved tolerance during the wet season.

ИЗВОД

СЕЗОНСКИ УТИЦАЈ НА УПОТРЕБЉИВОСТ ДРВЕТА *Polyalthia longifolia* КАО БИОИНДИКАТОРА САОБРАЋАЈНОГ ЗАГАЂЕЊА НА ПОДРУЧЈУ УНИВЕРЗИТЕТА У ИЛОРИНУ, НИГЕРИЈА

MOJEED O. BELLO[1], NASIRU ABDUS-SALAM[1], LATEEF A. IBRAHIM[1], TAOHEED O. BELLO[2], ABUBAKAR AREMU[3] и ABIDAH O. MUHAMMED[1]

[1]Department of Chemistry, University of Ilorin, P.M.B. 1515, Ilorin, Nigeria, [2]Department of Natural Sciences and Mathematics, College of Arts and Sciences, William V. S. Tubman University, P. O. Box 3570, Harper City, Maryland County, Liberia и [3]National Oil Spill Detection and Response Agency, P.M.B. 145, Abuja, Nigeria

Ова студија имала је за циљ испитивање сезонског утицаја на погодност дрвета *Polyalthia longifolia* као биоиндикатора загађења ваздуха, пореклом од саобраћаја. Листови су прикупљени дуж саобраћајнице изложене интензивним саобраћајним емисијама, као и са контролне локације без присуства саобраћаја. Током сушне и кишне сезоне анализирани су биохемијски параметри, укључујући pH вредност листа, садржај аскорбинске киселине, релативни садржај воде, укупни хлорофил и индекс толеранције на загађење ваздуха (*APTI*), применом стандардних аналитичких метода. Концентрације потенцијално токсичних елемената повезаних са аутомобилским загађивачима (Pb, Zn, Cr, Mn, Fe и Cu) одређене су методом атомске апсорпционе спектроскопије, након киселе дигестије узорака. Добијени резултати указују на то да су концентрације потенцијално токсичних елемената у већини случајева биле више у листовима прикупљеним дуж саобраћај-

нице у поређењу са контролном локацијом, изузев Cr и Cu на појединим местима узорковања, током кишне сезоне. Разлике у биохемијским параметрима између узорака са саобраћајнице и контролне локације потврђују утицај саобраћајног загађења у обе испитиване сезоне. Вредности *APTI* указале су на већу осетљивост биљке током сушне сезоне (средња вредност = 10,30), што сугерише смањену толеранцију на загађење, док је током кишне сезоне забележено благо повећање толеранције (средња вредност = 11,23). Резултати потврђују да *P. longifolia* показује изражену осетљивост на саобраћајно загађење током обе сезоне, која је виша у сушном периоду, док је способност толеранције повећана у кишној сезони, вероватно услед активирања ефикаснијих физиолошких одбрамбених механизама.

(Примљено 2. јануара, ревидирано 28. марта 2025, прихваћено 5. јануара 2026)

REFERENCES

1. A. Charron, L. Polo-Rehn, J.-L. Besombes, B. Golly, C. Buisson, H. Chanut, N. Marchand, G. Guillaud, J.-L. Jaffrezo, *Atmos. Chem. Phys.* **19** (2019) 5187 (https://doi.org/10.5194/acp-19-5187-2019)
2. U. N. Uka, E. J. D. Belford, J. N. Hogarh, *Bull. Natl. Res. Cent.* **43** (2019) 90 (https://doi.org/10.1186/s42269-019-0117-7)
3. N. Agrawal, A. Verma, *J. Emerg. Technol. Innov. Res*. **7** (2021) c1 (ISSN-2349-5162)
4. G. C. Lough, J. J. Schauer, J.-S. Park, M. M. Shafer, J. T. DeMinter, J. P. Weinstein, *Environ. Sci. Technol.* **39** (2005) 826 (https://doi.org/10.1021/es048715f)
5. D. P. Tripathi, A. K. Nema, *Atmos. Environ.* **309** (2023) 119862 (https://doi.org/10.1016/j.atmosenv.2023.119862)
6. E. Simon, V. É. Molnár, D. Lajtos, D. Bibi, B. Tóthmérész, S. Szabó, *Plants* **10** (2021) 2797 (https://doi.org/10.3390/plants10122797)
7. S. Punit, A. Rai, *Int. J. Energy Environ. Sci.* **6** (2021) 11 (https://doi.org/10.11648/j.ijees.20210601.12)
8. M. L. Kumar, A. Nag, B. Sinha, H. Gupta, *Plant Arch*. **20** (2020) 8183 (https://www.plantarchives.org/SPL%20ISSUE%2020-2/8183-8188%20(6935).pdf)
9. P. U. Singare, M. S. Talpade, *Int. J. Plant Res.* **3** (2013) 9 (https://doi.org/10.5923/j.plant.20130302.01)
10. M. O. Bello, N. Abdus-Salam, N. A. Odebunmi, A. A. Jimoh, *Fudma J. Sci.* **4** (2021) 302 (https://doi.org/10.33003/fjs-2020-0404-486)
11. J. S. Berame, J. E. Josue, M. L. Bulay, J. J. Delizo, M. L. A. Acantilado, J. B. Arradaza, D. W. M. G. Dohinog, *Nat. Environ. Pollut. Technol.* **22** (2023) 1331 (https://doi.org/10.46488/NEPT.2023.v22i03.020)
12. S. Das, S. N. Mallick, S. K. Padhi, S. S. Dehury, B. C. Acharya, P. Prasad, *Indian J. Environ. Prot.* **30** (2010) 563
13. B. G. Rao, B. S. Rekha, D. Ramadevi, B. Heera, *J. Glob. Trends Pharm. Sci.* **9** (2018) 4978 (https://www.jgtps.com/admin/uploads/5U48hm.pdf)
14. S. Kirthika, V. Vishnuprasad, *Int. J. Sci. Res. Arch.* **2** (2021) 257 (https://doi.org/10.30574/ijsra.2021.2.2.0085)
15. U. N. Uka, E. J. D. Belford, F. A. Elebe, *SN Appl. Sci.* **3** (2021) 131 (https://doi.org/10.1007/s42452-020-04027-9)
16. A. K. Umar, P. Singh, U. Garu, H. A. Ibrahim, R. Dhakar, *Int. J. Innov. Sci. Res. Technol.* **9** (2024) 1549 (https://doi.org/10.38124/ijisrt/IJISRT24AUG1079)

17. K. Azam, S. Zaman, M. Islam, M. Uddin, A. Salam, *J. Biodivers. Conserv. Bioresour. Manag.* **9** (2023) 1 (https://doi.org/10.3329/jbcbm.v9i2.70030)
18. B. S. Sagagi, A. M. Bello, H. A. Danyaya, *Environ. Monit. Assess.* **194** (2022) 699 (https://doi.org/10.1007/s10661-022-10360-w)
19. A. K. Pandey, M. Pandey, B. D. Tripathi, *Ecotoxicol. Environ. Saf.* **134** (2016) 358 (https://doi.org/10.1016/j.ecoenv.2015.08.028)
20. S. K. Dash, A. K. Dash, *Asian J. Chem.* **30** (2018) 219 (https://doi.org/10.14233/ajchem.2018.20991)
21. B. Vahid, *J.- Chem. Soc. Pakistan* **34** (2012) 1510 (https://jcsp.org.pk/PublishedVersion/5d749a38-2e9f-4693-8e46-8c2ab5667ac9Manuscript%20no%2028,%201st%20Gally%20proof%20of9179%20_Behrouz%20Vahid_.pdf)
22. S. Ter, M. K. Chettri, K. Shakya, *Amrit Res. J.* **1** (2020) 20 (https://doi.org/10.3126/arj.v1i1.32449)
23. T. Shakeel, M. Hussain, G. M. Shah, I. Gul, *Chemosphere* **287** (2022) 131937 (https://doi.org/10.1016/j.chemosphere.2021.131937)
24. S. Bolan, L. P. Padhye, T. Jasemizad, M. Govarthanan, N. Karmegam, H. Wijesekara, D. Amarasiri, D. Hou, P. Zhou, B. K. Biswal, R. Balasubramanian, H. Wang, K. H. M. Siddique, J. Rinklebe, M. B. Kirkham, N. Bolan, *Sci. Total Environ.* **909** (2024) (https://doi.org/10.1016/j.scitotenv.2023.168388)
25. N. A. Alrabie, F. Mohamat-Yusuff, R. Hashim, Z. Zulkeflee, M. N. A. Amal, A. Arshad, S. Z. Zulkifli, A. R. Wijaya, N. Masood, M. S. A. Sani, *Sustain.* **13** (2021) (https://doi.org/10.3390/su13169020)
26. A. El Din, M. M. Ibrahim, *World Appl. Sci. J.* **31** (2014) 1422 (https://www.idosi.org/wasj/wasj31(8)14/4.pdf)
27. H.-E. Sadia, F. Jeba, M. Z. Uddin, A. Salam, *SN Appl. Sci.* **1** (2019) 1377 (https://doi.org/10.1007/s42452-019-1421-4)
28. J. Prakash, S. B. Agrawal, M. Agrawal, *J. Soil Sci. Plant Nutr.* **23** (2023) 398 (https://doi.org/10.1007/s42729-022-01051-z)
29. M. K. Chini, *Int. J. Food Nutr. Sci.* **11** (2022) 566
30. R. Xalxo, K. Sahu, *Biologia (Bratisl).* **72** (2017) 1387 (https://doi.org/10.1515/biolog-2017-0171)
31. A. Gholami, A. Mojiri, H. Amini, *J. Anim. Plant Sci.* **26** (2016) 475 (http://www.thejaps.org.pk/docs/v-26-02/24.pdf)
32. A. J. Ogagaoghene, *CSJ-ChemSearch J.* **8** (2017) 41 (https://www.ajol.info/index.php/csj/article/view/166247)
33. 33 S. K. Prajapati, B. D. Tripathi, *J. Environ. Qual.* **37** (2008) 865 (https://doi.org/10.2134/jeq2006.0511)
34. M. Iqbal, M. Shafiq, S. Zaidi, M. Athar, *Glob. J. Environ. Sci. Manage.* **1** (2015) 283 (https://doi.org/10.7508/gjesm.2015.04.003)
35. S. Malathy, K. M. Dhanraj, M. Fathima, Utthukkattan, *Int. J. Life Sci. Res.* **6** (2018) 236 (https://www.researchpublish.com/upload/book/Air%20Pollution%20Tolerance-5999.pdf)
36. A. P. Deepalakshmi, H. Ramakrishnaiah, Y. L. Ramachandra, R. N. Radhika, *J. Environ. Sci. Toxicol. Food Technol.* **3** (2013) 10 (https://doi.org/10.9790/2402-0331014)

37. N. Kaler, P. Kashyap, H. Prasad, T. J. Singh, *Int. J. Chem. Stud.* **5** (2017) 716 (https://www.chemijournal.com/archives/2017/vol5issue4/PartK/5-4-64-779.pdf)
38. V. K. Vinita Katiyar, P. S. Dubey, *Ind. J. Environ. Toxicol*.**11** (2001) 78 (https://www.cabidigitallibrary.org/doi/full/10.5555/20023078001)
39. B. Abdu, M. Bature, D. H. Lamutanni, S. B. Sadiq, *Int. J. Sci. Res. Sci. Technol.* **11** (2024) 679 (https://doi.org/10.32628/IJSRST24113238).

Journal of the Serbian Chemical Society
JSCS@tmf.bg.ac.rs • www.shd.org.rs/JSCS
J. Serb. Chem. Soc. *91* (4) 425–439 (2026)
JSCS–5501
Original scientific paper
Published 1 May, 2026

Comparative assessment of adsorbents performances of plant biomasses grown on different sites: Case study of invasive *Acer negundo* L.

TATJANA ŠOŠTARIĆ[1]*, ZORICA LOPIČIĆ[1], DRAGANA RANĐELOVIĆ[1], TAMARA RAKIĆ[2], ANJA ANTANASKOVIĆ[1], IVANA MIKAVICA[1] and SNEŽANA ZILDŽOVIĆ[1]

[1]*Institute for Technology of Nuclear and Other Mineral Raw Materials, Boulevard Franchet d'Esperey 86, 11000 Belgrade, Serbia and* [2]*University of Belgrade, Faculty of Biology, Studentski trg 16, 11000 Belgrade, Serbia*

(Received 8 May, revised 11 June, accepted 12 August 2025)

Abstract: With the increasing global spread of invasive species, collecting their biomass could be a promising source for adsorbent development and water remediation. Therefore, the ability of adsorbent based on biomass of invasive plant *Acer negundo* L. originating from different habitat types was investigated for the lead removal from aqueous solution, in order to observe if different growing sites have effect on adsorbent performances. Three sites were selected for sampling: forest edges on Mt. Avala, riparian forests at Great War Island and banks of coal separation pond in Piskanja, Serbia. Characterisation was performed *via* pH_{pzc}, zeta potential, cation exchange capacity, SEM-EDS and FTIR analysis. Optimization of sorption parameters was done and the best performance was at pH 5.0, adsorbent dosage 2.0 g/dm^3 at 298 K for 60 min. Fitting of isothermal experiment data showed best correlation with Sips model (q_{max} is 94.92–131.52 mg/g, according to growing site). Among three reaction kinetic models, pseudo-second-order kinetics model showed best results. Since sample taken from the most anthropogenic influenced area have almost 30 % lower adsorption capacity than others, it can be concluded that growing site characteristics reflect on biomass performances, which is important factor for any further biomass usage.

Keywords: adsorption; invasive plants; *Acer negundo* L.; lead; kinetics.

INTRODUCTION

Acer negundo L., which originates from North America, was introduced to Europe as a cultivated woody species in the 17th century and was planted in the cities due to its rapid growth and resistance to weather extremes. It is still one of the most common species in parks, street tree lines and spontaneously occurs along roads and in other disturbed habitats. However, it has become invasive in both

* Corresponding author. E-mail: t.sostaric@itnms.ac.rs
https://doi.org/10.2298/JSC250508065S

natural and urban habitats.[1] *A. negundo* has broad ecological amplitude: it tolerates air pollution, soils with wide range of pH values, extreme cold and drought.[2] In Serbia, *A. negundo* is considered as one of the most aggressive invasive tree species in forest ecosystems and its presence has also been detected in many areas with preserved natural values.[3]

Abundant biomass of invasive plant species is nowadays recognized for its potential benefits in providing various environmental services. Adsorption, as one of the sustainable and efficient remediation technique could be potential field for its application. Moreover, adsorption is considered as a cost-effective and reliable method for purification of contaminated water, especially in the case of common water metal pollutants.[4] Plant-derived materials such as wood, leaves, fruits, or seeds have been studied for this purpose, where adsorbents based on leaf biomass showed the best adsorption performance.[5] Biomass of *Acer* species have been tested as adsorbents for metal removal from aqueous solutions,[6] but no such studies have been conducted on invasive *A. negundo*. Also, so far there has been lack of investigations concerning sorption performance of biomasses of the same species collected from different habitats. Therefore, the research questions aimed to answer were: a) is invasive *A. negundo* leaf biomass suitable adsorbent for metal aqueous pollution? b) Does the *A. negundo* leaves originated from sites with contrasting ecological, edaphic and anthropogenic differ in their composition? And c) does the leaf composition variability impact metal adsorption capacity?

EXPERIMENTAL

Three different growing sites were selected for sampling *A. negundo* leaves. First sampling site, Mt. Avala, represents protected area in the vicinity of Belgrade, with environment that supports a large diversity of species. It is recognized as Emerald Network site and as a Serbian ecological network site.[7] Seven allochthonous invasive tree species were recorded on Mt. Avala, including *A. negundo*.[8] Area of the natural landscape Great War Island, the second sampling site, represents unique example of protected area located in the urban environment of Belgrade. The island is habitat for many species and it is being annually flooded by the Danube River. It is recognized as one of the central areas of Serbia's ecological network and the ecological Network within the Danube ecological corridor.[7,9] However, research of Kašanin *et al.*[10] showed increased pollution of Great War Island sediments with Cu and Cd, as well as with oil pollutants. In the area of Great War Island 17 invasive tree species, among which is *A. negundo*, are registered.[11] Third sampling point is placed on the banks of former coal separation pond in Piskanja, which is a part of industrial setting at Ibar coal mining basin in South–Central Serbia. This area is nowadays sporadically colonized by various plant species, including invasive ones.[12] Sampling points are presented in Fig. S-1 of the Supplementary material to this paper.

Composite soil samples were taken at each sampling site from the upper layer (0–20 cm) of the rhizosphere zone. Soils were air-dried and sieved through 2 mm sieve. Pseudo-total content of elements was determined by using aqua region digestion following ISO 11466:1995 standard[13] and measured by atomic absorption spectroscopy (AAS). The content of soil organic carbon (SOC) was determined by oxidation with a solution of $KMnO_4$ according to the Kotzman method.[14]

Up to 100 fully developed leaves from mature *A. negundo* trees were collected during June from middle canopy section and each side of the crown of 3–5 individuals of approximately similar age, in order to make representative composite samples for each sampling site. Leaves were collected by pruning following methodology described elsewhere.[15] They were rinsed with distilled water and air-dried. Leaves were then grinded in blade grinder (20.000–30.000 rpm) and powdered prior to analysis (particle size < 0.2 mm). Samples from Mt. Avala, Great War Island and coal separation pond Piskanja were labelled as ANA, ANV and ANS, respecttively, as presented in Fig. S-1. In order to determine the content of elements, the samples were dissolved using standardized microwave-assisted acid dissolution procedure for this type of material in high-performance microwave digestion system Ethos UP, Milestone and the concentrations of elements were determined by AAS, while K, Ca and Na were determined by atomic emission spectrometry using PerkinElmer PinAAcle 900T, USA, directly from the prepared solution. Bioconcentration factor (*BCF*) was used to determine the efficiency of metal accumulation in leaves, and it was calculated as a ratio between metal concentration in leaves and pseudo-total concentration of the same element in the soil.[16] Cation exchange capacity (*CEC*) was determined by method that involves saturation of the cation exchange sites by ammonium acetate.[17] Determination of pH value of suspensions (pH_{sus}) was performed according to standard ASTM D6851-02. Determination of the point of zero charge (pH_{pzc}) was done in accordance to methodology described elsewhere.[18] In order to determine zeta potential of samples Zetasizer Nano Z (Malvern, UK) was used in the pH range from 2.0 to 10. In order to observe surface morphology and elemental composition of leaf powder, scanning electron microscopy combined with the energy dispersive spectroscopy (Jeol JSM 6460, Jeol Ltd., Japan) was used. The dried samples were coated with thin layer of gold under vacuum conditions. Attenuated total fourier transform infrared spectroscopy was used for determination of samples surface functional groups by using Thermo Nicolet 6700 FTIR (Thermo Fisher Scientific, USA). The spectra were recorded in range from 4000 to 400 cm^{-1}. The region between 1900 and 2200 cm^{-1} is interrupted due to strong diamond IR absorption.

Batch sorption experiments were performed through the sets of the experiments where one parameter was varied, while the others remained constant. Experiments were performed by mixing sample with metal solution and stirring it on orbital thermostatic shaker (HeidolphUnimax 1010, USA) at 200 rpm. Lead stock solution (1.0 mmol/dm^3) was prepared from $Pb(NO_3)_2{\cdot}3H_2O$ (analytical grade). After investigated period of time suspension was filtrated and the filtrate was analysed using AAS. The effects of following parameters on sorption capacity were analysed: a) effect of initial pH in the range from 2.0 to 5.0; b) effect of contact time in range from 2 to 180 min; c) effect of sorbent concentration in range from 1 to 20 g/dm^3; d) effect of initial lead concentration in range from 5 to 600 mg/ dm^3; e) effect of temperature in range from 288 to 328 K. The sorption capacity was calculated using the following equation:

$$q_e = \frac{(C_0 - C_e)V}{m} \tag{1}$$

where q_e is the amount of lead absorbed (mg/g); C_0 and C_e are the initial and equilibrium lead concentrations (mg/dm^3); V – the sorbate solution volume (dm^3); m – the sorbent mass (g). The involvement of ion-exchange mechanism during the sorption process was investigated by following the release of cations (Ca^{2+}, Mg^{2+}, Na^+, K^+ and H^+) from sorbents after process of lead sorption. The ratio was calculated by using the following equation:

$$R_{b/r} = \frac{\left[Pb^{2+}\right]}{\left[Ca^{2+}\right]+\left[Mg^{2+}\right]+\left[Na^{+}\right]/2+\left[K^{+}\right]/2+\left[H^{+}\right]/2} \quad (2)$$

where $R_{b/r}$ is the ratio of the bonded lead ions and released cations, while in brackets are amount of bonded lead ions and amounts of specific cations released from sorbents.

Kinetic and isotherm investigations were performed in order to analyse the sorption process, fitting the experimental sorption data by various isotherm and kinetic models, which might elucidate the nature of sorption process. Kinetic and isothermal experimental data were obtained from the experiments performed under optimised operational parameters ($C_{Pb^{2+}}$ = 200 mg/dm^3, m/V = 2.0 g/dm^3, pH 5.0, T = 298 K and t = 180 min). Isothermal sorption experiments were conducted under the same operational parameters, varying initial lead concentration from 5.0 up to 600 mg/dm^3. Models/equations which have been used in this paper are presented in Table S-I of the Supplementary material. All sorption experiments were performed in triplicate and results were reported as arithmetic mean values. The statistical analysis was performed and nonlinear correlation coefficient (R^2) and the reduced chi square test (χ^2) were applied to measure the appropriateness of applied kinetic and isotherm models.

Soil and plant analysis were carried out in triplicates, and the results are presented as arithmetic means ± standard deviations. Statistical differences between sites and concentration of elements in plant leaves were determined by using one-way analysis of variance (ANOVA) in Statistica 8.0 (StatSoft 2007).

RESULTS AND DISCUSSION

Characterization of samples

Invasive plant species exhibit broad ecological amplitude that allows them to colonize ecologically diverse habitats. Due to developmental plasticity, the same plant species grown on ecologically different habitats might show significant variation in structural and physiological traits.[19] Plant leaves are considered to be among most sensitive organs to the influence of environmental factors, showing differences in chemical components and presence of functional groups.[20] In relation to that, characterization of collected samples of soil and leaf biomass was conducted. The measurements of the soil pH, content of soil organic carbon (SOC), concentration of potentially toxic elements (PTE) and macroelements in topsoil layers (0–20 cm), together with concentrations of PTE in leaves are presented in Table S-II (Supplementary material). Soil pH ranges from neutral (ANA_S) and slightly acid (ANV_S), to acidic (ANS_S), while content of SOC shows higher values on ANA_S. On this site, value of Pb content is high, which is in line with results of Stanković *et al.*[21] for the same site. Highest concentration of Fe and Ni due to the present technogenic pollution is recorded for soils of separation pond (ANS_S), which is in accordance with investigation of Ranđelović *et al.*[12] Content of macroelements varies significantly between the sites, whereas all of them, except Na, show the lowest concentration at ANS_S. The content of measured elements in plant leaves remains in the range of normal[22] except in the case of Ni that shows excess

values for all sites. As expected, the highest concentration of Ni and Cd are recorded on *A. negundo* leaves from coal separation pond (ANS_L). Content of Ca and Mg significantly differs in leaves originating from different sites, showing the lowest concentration in ANS_L, while concentration of K exhibited highest values on the same site. Similarly, Liu *et al.*[23] compared leaf mineral content in healthy and declining *Acer saccharum* stand and find out significantly lower concentration of leaf Ca and Mg in declining stand in comparison to healthy and higher concentration of leaf K in declining in comparison to healthy stand. Role of K is recognized in the synthesis of protein and carbohydrate metabolism for alleviation of increased abiotic stresses[24] and Drzewiecka *et al.*[25] have found that K was mainly transported and accumulated in the aerial organs of *Acer platanoides* cultivated on polluted mine sludge, accompanied by ROS scavenging and accumulation of secondary metabolites in plant leaves.

Metal uptake from the soil by plant, expressed as *BCF* factor is presented in Table S-III of the Supplementary material. A value of *BCF* below 1 refers to the low accumulation of element in plant organs which is the case for all investigated elements, except Mn, on sites ANA and ANV.

In order to determine capability of leaf samples (future adsorbents) to exchange cations under chemically neutral conditions, *CEC* was detected. It is evident from Table I that ANS, originating from most antrhropogenically influenced area, has the lowest total *CEC* despite the fact that it has 40 and 15 % higher amount of K ions in comparison to ANA and ANV, respectively.

TABLE I. The values of *CEC* (meq/100 g), pH_{pzc}, pH_{sus} for ANA, ANV and ANS

Site	K	Na	Ca	Mg	Total ∑	pH_{pzc}	pH_{sus}
ANA	36.57	7.35	52.40	73.84	170.16	4.14	3.95
ANV	45.91	7.44	49.90	62.11	165.36	4.12	4.07
ANS	52.62	7.33	37.43	47.72	145.09	4.08	3.72

According to Kashyap *et al.*[27] excess K may induce deficiency of other nutrients like Mg and Ca, which is in accordance with results from Table S-II (amount of Ca and Mg is noticeably lower in ANS). Lower value of Ca and Mg content in leaves was noted by Liu *et al.*,[23] in declining *Acer saccharum* stands developing on acidic soil, too. It is recognized that Ca and Mg deficiencies are commonly distributed on acid soils, as such environment promotes leaching of these cations[28] which is in accordance with obtained result of ANS soil pH value (4.76). The results of point of zero charge (pH_{pzc}) were explained elsewhere.[29] The results of zeta potential values (Fig. S-2 of the Supplementary material) indicate that in all samples the negatively charged surface functional groups are predominant.

In order to observe and analyse surface morphology and chemical composition of investigated samples, SEM micrographs and corresponding EDS spectra of

samples are presented in Fig. 1. Heterogeneous structures of samples (cracks, irregular pores and rough surface with parts of tracheid) have been described elsewhere.[30] Such morphology promotes metal ions diffusion into internal layers where numerous active sites become more available for ions, and thus increase adsorption performances of sorbent.

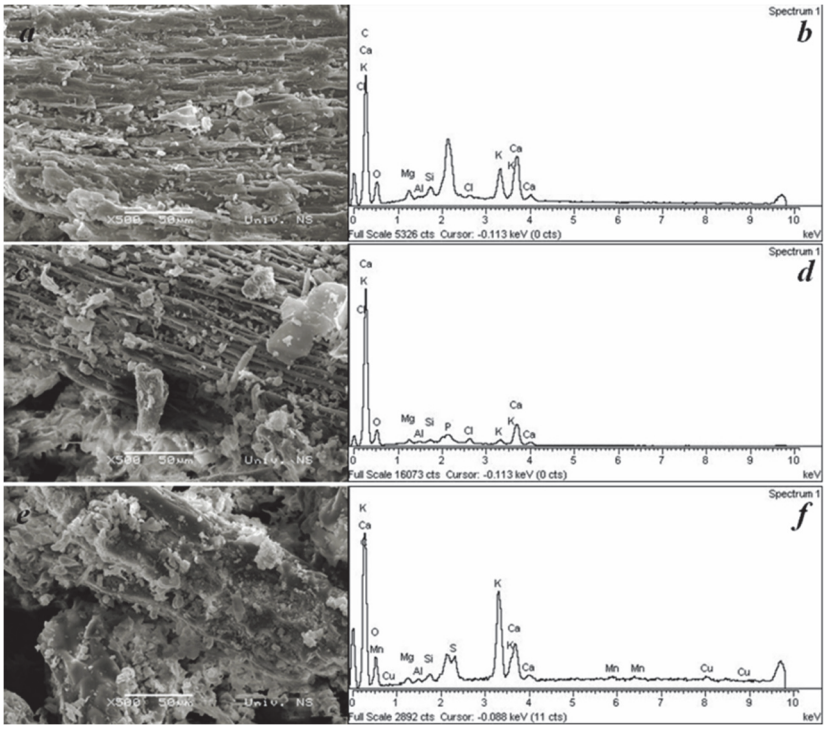

Fig. 1. SEM micrographs and EDS spectrums of: ANA (a/b), ANV (c/d) and ANS (e/f).

ATR-FTIR characterization (Fig. S-2) was carried out, in order to understand changes that occurred in surface functional groups from populations from different habitats. Despite ATR-FTIR spectra of ANV and ANA samples appear to be very similar, certain differences in spectra of ANS sample can be noticed: *i*) higher relative intensity of 1731 cm^{-1} bend (that refers to the C=O stretching vibration of esters from lipid and protein components of cell walls, according to Deng *et al.*[31]), *ii*) the appearance of the shoulder on 1645 cm^{-1} (also C=O stretching of amide I proteins, according to Azuma *et al.*[32]), *iii*) absence of 1548 cm^{-1} peak related to N–H or C–N stretching of amide II[33]), *iv*) presence of 1516 cm^{-1} peak related C=C stretching of proteins (amide II), *v*) lower intensity of the band 1317 cm^{-1} related to the C–H of the methyl functional groups and *vi*) appearance of the new band at 1205 cm^{-1}, due to C–O bending vibration of carbohydrate functional groups.[31]

This result points out to the involvement of different mechanisms of leaves in coping with metal stress common to various plant species, such as impact on protein synthesis and their modification, as well as change in carbohydrate metabolism and signalling to oxidative stress regulation.[34]

Sorption studies

Investigation of the effect of pH onto sorption capacity (Fig. 2a) showed the same trend for all three samples: low sorption capacity of sorbents at pH 2.0, which slowly rises with increase of pH value of the solution. It is well known that solution pH affects the dissociation of functional groups present on the sorbent surface: as the pH value increases, de-protonation of functional groups occurs and the negative charge density increases, increasing the removal of cations from the solution. Since the sorption process is the most efficient at pH 5.0 and in order to avoid formation of hydroxides which may occur at higher pH values, all further experiments were carried out at that pH value. The effect of contact time was examined in order to define required time for equilibrium to be reached. As can be seen from Fig. 2b, the initial sorption of Pb^{2+} occurs very rapidly due to available and abundant active sites present on sorbents surface, sorption of lead ions increases over time and reaches equilibrium after 60 min. The effect of sorbent concentration on sorption capacity and removal percentage was also investigated and results are presented in Fig. 2c. At sorbent concentration of 1.0 g/dm^3, lead removal percentage was 58, 53 and 49 % for ANA, ANV and ANS, respectively. However, when sorbent concentration was raised to 2.0 g/dm^3 the percentage of lead removal increased up to 87, 84 and 73 %, respectively. With further increase of sorbent concentration (up to 20 g/dm^3), the percentage of lead removal went up to 93, 93 and 84 %, while the sorption uptake decreased drastically (from 90, 87 and 70 mg/g to 8.3, 7.5 and 8.9 mg/g, respectively). In relation to that, sorbent concentration of 2.0 g/dm^3 was used in all further experiments. Rise of sorbent concentration induces particle aggregation and stirring difficulties, consequently reducing effective surface area and number of available active sites and slowing down the mass transfer.[15] The results of effect of initial lead concentration on sorption capacity are presented in Fig. 2d. Noticeably, the sorption capacity increased, at initial concentration 2.0 mg/dm^3, from 2.3, 2.4 and 1.8 mg/g to 90.5, 86.25 and 73.75 mg/g at initial concentration 200 mg/dm^3, for ANA, ANV and ANS, respectively. It is well known that increase of initial metal concentration is a driving force for overcoming mass transfer resistance of cations in solid/liquid phase.[15] Effect of temperature on lead sorption capacity of tested sorbents was investigated and the obtained results are presented at Fig. S-4 of the Supplementary material. As the temperature increases, the biosorption capacity decreases from 89.5, 87.7 and 75.7 mg/g at 288 K to 84.1, 81.7 and 69.25 mg/g at 328 K for ANA, ANV and ANS, respectively. Sorption process of lead ions onto investigated sorbents is an exothermic process:

an increase in temperature lead to decrease in ions removal and temperature rise weakens attractive forces between active sites on the sorbent surface and lead ions in solution.

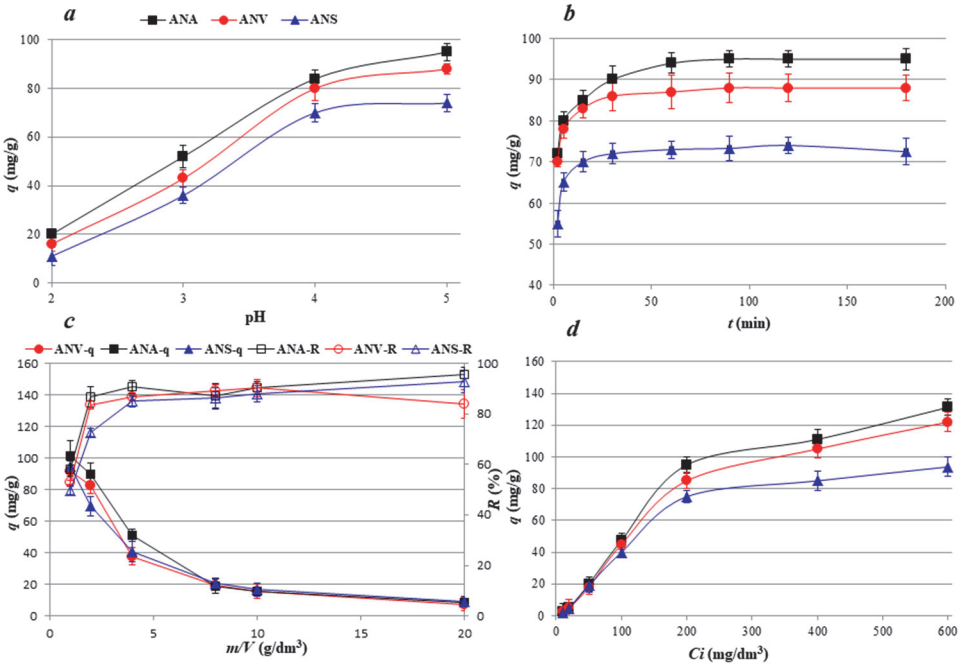

Fig. 2. Effect of operative parameters onto sorbent capacity: effect of pH (a), contact time (b), sorbent concentration (c) and initial Pb^{2+} concentration (d).

Investigation of ion exchange mechanism

Since analyses of the *CEC* showed that all samples have cations in exchangeable positions, the participation of the ion-exchange mechanism in sorption process is expected. Consequently, releases of the exchangeable cations from all materials, together with solution pH value before and after the sorption process, were investigated and the data are presented in the Table S-IV of the Supplementary material. Fig. 3 revealed that the sum of cations, released from ANA and ANV samples, was almost equal to the amount of Pb^{2+} bound on the same sorbents, except at lowest metal concentration, suggesting that ion-exchange mechanism is dominant during the lead sorption process in both samples. However, the sum of the released cations from sorbent ANS is higher than concentration of bonded lead ions. ANS bonds reduce lead ions which are in correlation with lower amount of exchangeable cations on its surface (Table I). These results are in accordance with Table S-IV. Also, the measured final pH value of the solution after sorption process was 3.77 (lower than initial pH value – pH 5.0) indicating that ANS releases a significant

amount of competitive hydrogen (hydronium) ions, which reduces binding of lead. This phenomenon might reflect differences in composition of functional groups and active binding sites of sorbents originating from different growing sites, as supported by FTIR analysis.

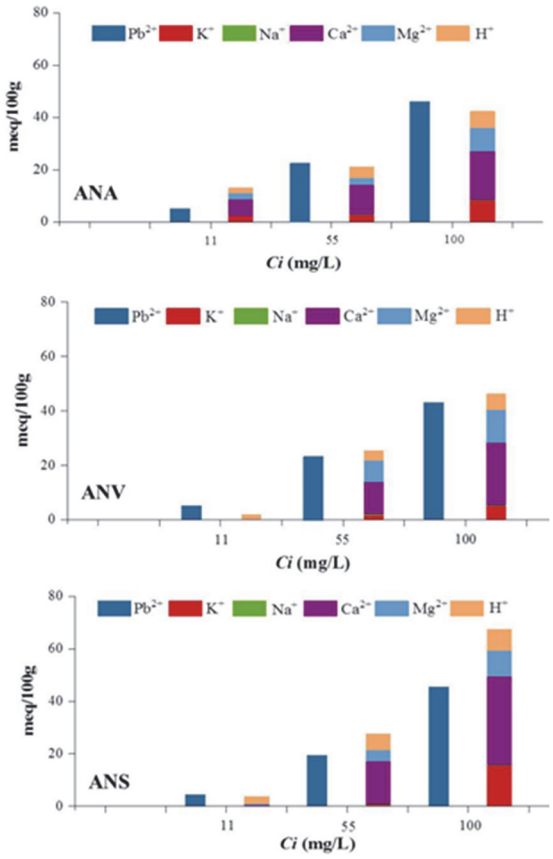

Fig. 3. The amount of sorbed lead ions and released cations from ANA, ANV and ANS at different initial metal concentrations.

Kinetic, sorption isotherm and thermodynamic studies

Table II summarizes data for experimental sorption capacity at maximum time investigated (q_e), together with the kinetic and isotherm model parameters and corresponding determination coefficients (R^2) and χ^2 values. The results of fitting experimental data showed that the best fit was obtained by using the pseudo second order kinetic model, with the highest values of correlation coefficient (R^2) and the lowest chi-factor (χ^2) among the all models applied. This indicates that the sorption mechanism is limited by bonding forces through sharing electrons between the sorbate and the sorbents. As can be seen from Table II, Lagergren pseudo-first order equation, as well as Elovich model, cannot be used to predict the sorption kinetic of lead by any sorbent investigated; the application of these models resulted

in the lower values of R^2 and the higher χ^2 values, but also calculated q_m values differ from experimental q_e values. The graphs of kinetics models are presented in Figs. S-5 to S-7 of the Supplementary material.

TABLE II. Kinetic and isotherm parameters calculated for lead sorption by different sorbents

Kinetic model	ANA	ANV	ANS	Isotherm model	ANA	ANV	ANS
Exp. q_e / mg g^{-1}	86.62	83.81	73.25				
Pseudo-first-order				Langmuir			
q_m / mg g^{-1}	84.76	83.10	71.86	q_m / mg g^{-1}	138.99	129.42	105.28
k_1 / min^{-1}	0.9584	1.410	0.6893	K_L / dm^3 mg^{-1}	0.0295	0.0360	0.0224
R^2	0.8320	0.7205	0.8035	R^2	0.995	0.991	0.988
χ^2	3.5754	1.1044	8.4628	χ^2	12.42	19.20	17.14
Pseudo-second-order				Freundlich			
q_m / mg g^{-1}	86.04	83.66	73.67	K_F / mg g^{-1} (dm^3/g)^n	14.53	15.96	5.472
k_2 / g mg^{-1} min^{-1}	0.0323	0.0830	0.0198	$1/n$	2.597	2.770	2.570
R^2	0.9744	0.9449	0.9706	R^2	0.920	0.904	0.895
χ^2	0.5446	0.3380	1.2682	χ^2	210.18	221.78	149.18
Elovich				Sips			
q_m / mg g^{-1}	89.93	84.60	76.31	q_m / mg g^{-1}	131.52	120.18	94.92
a / mg g^{-1} min^{-1}	4.00E12	1.66E29	8.99E6	K_s / dm^3 g^{-1}	0.0205	0.0181	0.0090
b / g mg^{-1}	0.3780	0.8548	0.2601	s	1.159	1.297	1.345
R^2	0.8108	0.8623	0.8531	R^2	0.997	0.998	0.985
χ^2	4.0270	0.5442	6.3276	χ^2	8.610	4.914	6.912

The applicability of pseudo-second order kinetics model suggested that the lead removal by *A. negundo* sorbents is based on chemical reaction, involving the exchange of electrons between the sorbents and the metal ions present in sorbate solution. The highest value of the pseudo-second reaction rate constant, k_2, is obtained for ANV sorbent (0.0830 g/(mg min)), indicating the fastest removal for this sorbent. This can also be seen from the Fig. S-4, where the fitting of the experimental data by pseudo-second order model is presented. Although the highest rate is observed for ANV, the ANA sorbent has higher overall maximum sorption capacity under applied operational parameters, 86.04 mg/g, while the lowest one is found to be the capacity of ANS (73.67 mg/g). Previous reports on sorption kinetics by the similar biomasses suggest that pseudo-second order kinetics govern most of the sorption processes. For example, Qaiser *et al.*[35] have investigated the potential of *Ficus religiosa* leaves in lead sorption, and find out that the sorption process is well described by the pseudo-second order model, with maximum removal capacity of 19.76 mg/g at 20 °C. Sangi *et al.*[36] have investigated the potentials of *Ulmus* sp. and *Fraxinus* sp. tree leaves for lead removal and obtained the kinetic results which indicated that second-order kinetics best describe the experimental data, relying on the assumption that the rate limiting step involves valence forces through sharing or exchange of electrons between the sorbent surface sorbent and sorbate ions.

Additional, two-parameter model were used to correlate isotherm data: the Langmuir[37] equation which is valid for monolayer sorption onto a surface with a finite number of identical sites and the empirical Freundlich[38] isotherm based on sorption on a heterogeneous surface. Beside them one three-parameter model, named Sips[39] isotherm was used. This model represents combination of Langmuir and Freundlich expressions: at low metal concentration it approaches Freundlich isotherm, while at high concentrations it predicts a monolayer adsorption capacity characteristic for the Langmuir isotherm. Graph of all isotherm models are presented in Figs. S-7 and S-8. Looking at the data (Table II), on the basis of the R^2 closest to 1 and the lowest values of χ^2, the following order of fitting equations is found to be: Sips>Langmuir>Freundlich. The equilibrium parameters, R_L, calculated as $R_L = 1/(1+K_L C_0)$, are falling in the range from 0.047 up to 0.889 in the investigated concentration range. These values indicate that the removal of lead ions onto *A. negundo* sorbents is favourable for all sorbents applied. The best fitting model (Sips) of the sorption equilibrium is presented at Fig. S-7. ANA has maximum sorption capacity of 131.52 mg/g at 298 K while the lowest removal was achieved by ANS application, 94.92 mg/g. Sips model implies that, in the same time, monolayer sorption and heterogeneous energetic distribution of active sites on the surface of the sorbent is possible.[40] Moreover, Sips model has been proven to be applicable in cases of pH dependent sorption, such is the case of lead removal by *A. negundo* sorbents.[41] Table III contains comparative data of investigated materials sorption capacity with other similar lead sorbents found in the literature. As can be seen, among three sorbents investigated in this study, the highest sorption capacity is detected in ANA which is grown in uncontaminated habitat. This indicates that the majority of the presented functional groups are available for adsorption of Pb^{2+}. The lowest sorption capacity is detected in ANS, which indicates lower availability of functional groups for Pb^{2+} adsorption due to their current involvement in metal immobilization and/or different chemical composition of leaves and different proportion of functional groups to which Pb^{2+} show high binding affinity.

TABLE III. Comparison of lead sorption on various leaves sorbents

Sorbent (leaf powder)	q_m / mg g^{-1}	pH	C_i / mg dm^{-3}	Model
Bael tree[42]	4.065	5.0	25–100	Langmuir
Cocos nucifera[43]	8.475	5.0	10–150	Langmuir
Ficus religosia[44]	37.45	4.0	10–1000	Langmuir
Cinnamomum camphora[45]	73.15	5.0	50–400	Langmuir
Broussonetia papyrifera[46]	84.74	5.5	10–500	Langmuir
Aegle marmelos[47]	104.0	5.1	8.7–180.2	Langmuir
Citrus grandis[48]	207.2	4.1	0–1000	Sips
Acer negundo (this study)				
ANA	131.5	5.0	5–600	Sips
ANV	120.2	5.0	5–600	Sips
ANS	94.92	5.0	5–600	Sips

Although this study showed that the sorption capacity of *A. negundo* leaf powder in comparison to other sorbents with similar structure found in literature is very high, it primarily emphasizes the importance of growing site on plant material properties and its sorbent capacity. As found in this investigation, the variability in sorption capacity may be significantly different among different samples and it even reached 30 %.

CONCLUSIONS

The presented investigation has shown that sorbents based on *A. negundo* L. leaves are the promising sorbents for the removal of lead ions from contaminated waters, but has also highlighted the importance of growing site as a factor affecting the sorption performance of the future sorbent. Prior to the sorption experiments, characterization of soils and leaves revealed differences between samples from selected growing sites, particularly with respect to the content of PTE and *CEC*, as well as differences in the presence of certain functional groups in *A. negundo* leaves, responsible for sorption. The adsorption process was pH dependent and the optimum pH for lead removal was 5.0, after 60 min of contact time, at optimized sorbent dose of 2.0 g/dm^3. The results of fitting experimental data showed that the best fit was obtained by using the pseudo second order kinetic model, indicating that the sorption mechanism is limited by binding forces through electrons sharing between the lead ions and the sorbents. It was show that lead ions were removed with a maximum lead loading capacity of the samples of 131.52, 120.18 and 94.92 mg/g for ANA, ANV and ANS, respectively, which is either comparable to or better than the lead loading capacities of other reported similar sorbents. This research indicated that the differences in growing sites should be taken into account when studying the sorption process, as they affect the adsorption performance of the chosen biomass. Future studies could reveal the extent of this influence on different sorbents and uncover the most influential site factors and physiological mechanisms responsible for such outcome.

SUPPLEMENTARY MATERIAL

Additional data and information are available electronically at the pages of journal website: https://www.shd-pub.org.rs/index.php/JSCS/article/view/13367, or from the corresponding author on request.

ИЗВОД

ПОРЕЂЕЊЕ АДСОРПЦИОНИХ СВОЈСТВА БИЉНЕ БИОМАСЕ ПОРЕКЛОМ СА РАЗЛИЧИТИХ СТАНИШТА – СТУДИЈА СЛУЧАЈА ИНВАЗИВНЕ ВРСТЕ *ACER NEGUNDO*

ТАТЈАНА ШОШТАРИЋ[1], ЗОРИЦА ЛОПИЧИЋ[1], ДРАГАНА РАНЂЕЛОВИЋ[1], ТАМАРА РАКИЋ[2], АЊА АНТАНАСКОВИЋ[1], ИВАНА МИКАВИЦА[1] и СНЕЖАНА ЗИЛЦОВИЋ[1]

[1]Институт за технологију нуклеарних и других минералних сировина, Франше д'Епереа 86, 11000 Београд и [2]Универзитет у Београду, Биолошки Факултет, Студентски трг 16, 11000 Београд

На природним стаништима инвазивне биљне врсте имају снажан утицај на биодиверзитет, примарну продуктивност екосистема, мрежу исхране, кружење хранљивих материја. Услед њиховог глобалног ширења, њихова употреба се намеће као атрактивно решење. Развој адсорбента за пречишћавање вода, је једно од могућих решења. У складу са тим, у овом раду, испитана су својства адсорбената на бази биомасе инвазивне биљке *A. negundo,* са три различита станишта, у сврху уклањања олова из воденог раствора, како би се показало да ли карактеристике станишта утичу на својства адсорбента. За узорковање су одабране три локације: ободне шуме на Авали, приобалне шуме на Великом ратном острву и обод базена за сепарацију угља у Пискањи. Карактеризација материјала је извршена коришћењем pH_{pzc}, зета потенцијала, капацитета за измену катјона, SEM-EDS и FTIR анализа. Оптимизацијом параметара сорпције утврђено је да је најбољи учинак при pH 5,0, дози адсорбента 2,0 g/dm^3 на 298 K током 60 min. Применом изотермних модела на податке добијене у сорпционим експериментима, утврђена је најбоља корелација са Сипсовим изотермним моделом (q_{max} је 94,92–131,52 mg/g, у односу на станишта). Такође, међу три коришћена кинетичка модела, најбоље резултате показао је модел кинетике псеудо-другог реда. Резултати ове студије су показали да узорак који је узет са подручја које је под највећим антропогеним утицајем, има скоро 30 % нижи капацитет адсорпције у односу на друга два узорка. Можемо се закључити да се утицај станишта огледа на физичко–хемијска својства биомасе, а са тим у вези и на сорпционе одлике биомасе, што је важан фактор за даљу употребу у сврху развоја сорбената.

(Примљено 8. маја, ревидирано 11. јуна, прихваћено 12. августа 2025)

REFERENCES

1. D. Sikorska, P. Sikorski, P. Archiciński, J. Chormański, R. J. Hopkins, *Sustainability* **11** (2019) 5838 (https://doi.org/10.3390/su11205838)
2. S. Dineva, *Dendrobiology* **53** (2005) 11 (https://bibliotekanauki.pl/articles/41089.pdf)
3. V. Stojanović, I. Bjedov, I. Jovanović, I. Jelić, D. Obratov Petković, M. Nešić, D. Nedeljković, *Selected Invasive Alien Species in the Flora of Serbia – Material for the Development of National Regulations on the Prevention of Introduction and Spread of Invasive Alien Species and Their Management*, Institute for Nature Conservation of Serbia, Belgrade, 2021 (in Serbian)
4. M. Akram, B. Khan, M. Imran, I. Ahmad, H. Ajaz, M .Tahir, F. Rabbani, I. Kaleem, M. Akhtar, N. Ahmad, N. Samad Shah, *Int. J. Phytoremediat.* **21** (2019) 138 (https://doi.org/10.1080/15226514.2018.1488810)
5. I. Anastopoulos, A. Robalds, H. N. Tran, D. Mitrogiannis, D. A. Giannakoudakis, A. Hosseini-Bandegharaei, G. L. Dotto. *Environ. Chem. Lett.* **17** (2019) 755 (https://doi.org/10.1007/s10311-018-00829-x)
6. R. H. Krishna, W. B. Gilbert, *Int. J. Adv. Chem*. **2** (2014) 1 (https://doi.org/10.14419/ijac.v2i1.1531)
7. Official Gazette of RS, No. 102/2010: *Decree on the Ecological Network*

8. M. Glišić, D. Lakušić, J. Šinžar-Sekulić, S. Jovanović, *Bot. Ser*. **38** (2014) 131 (https://botanicaserbica.bio.bg.ac.rs/arhiva/pdf/2014_38_1_604_full.pdf)
9. D. Filipović, Lj. Petrović, *Glas. Srp. geogr. druš.* **95** (2015) 109 (https://doi.org/10.2298/GSGD1502109F)
10. M. Kašanin-Grubin, S. Štrbac, S. Antonijević, S. Đogo Mračević, D. Ranđelović, I. Orlić, A. Šajnović, *J. Environ. Manage.* **251** (2019) 109574 (https://doi.org/10.1016/j.jenvman.2019.109574)
11. S. Jarić, Z. Mataruga, D. Sekulić, M. Pavlović, D. Pavlović, M. Mitrović, P. Pavlović, *Acta Herbologica* **29** (2020) 111 (https://doi.org/10.5937/ActaHerb2002111J)
12. D. Ranđelović, K. Jakovljević, T. Mišljenović, J. Savović, M. Kuzmanović, N. Mihailović, S. Jovanović, *Water Air Soil Poll.* **231** (2020) 272 (https://doi.org/10.1007/s11270-020-04655-2)
13. ISO 11466 (1995), *Soil quality-extraction of trace elements solublein* aqua regia, International Organization for Standardization, Geneva
14. JDPZ, *Chemical methods for soil analysis*, Beograd, 1966
15. J. Liang, H. L. Fang, T. L. Zhang, X. X. Wang, Y. D. Liu, *Urban For. Urban Green*. **27** (2017) 390 (https://doi.org/10.1016/j.ufug.2017.03.006)
16. A. Sahay, A. Inam, A. Iqbal, *Int. J. Environ. Sci. Tech.* **17** (2019) 2889 (https://doi.org/10.1007/s13762-019-02580-4)
17. S. Stanković, T. Šoštarić, M. Bugarčić, A. Janićijević, K. Pantović-Spajić, Z. Lopičić, *Acta Period. Technol.* **50** (2019) 268 (https://doi.org/10.2298/APT1950268S)
18. T. Šoštarić, M. Simić, Z. Lopičić, S. Zlatanović, F. Pastor, A. Antanasković, S. Gorjanović, *Processes* **11** (2023) 1343 (https://doi.org/10.3390/pr11051343)
19. S. Sultan, *Trends Plant Sci.* **5** (2000) 537 (https://doi.org/10.1016/S1360-1385(00)01797-0)
20. X. Ye. M. Wang, X. Zhang, R. Xu, D. Xu, *Environ. Pollut. Bioavail.* **31** (2019) 240 (https://doi.org/10.1080/26395940.2019.1630321)
21. D. Stanković, M. Krstić, M. Knežević, M. Šijačić-Nikolić, I. Bjelanović, *Fresenius Environ. Bull.* **21** (2012) 495
22. A. Kabata-Pendias, *Trace elements in soils and plants*, CRC Press, Taylor & Francis Group, Boca Raton, FL, 2011 (https://doi.org/10.1201/b10158)
23. X. Liu, D. S. Ellsworth, M. T. Tyree, *Tree Physiol.* **17** (1997) 169 (https://doi.org/10.1093/treephys/17.3.169)
24. M. Hasanuzzaman, M. H. M. B. Bhuyan, K. Nahar, M. S. Hossain, J. A. Mahmud, M. S. Hossen, A. A. C. Masud, M. Moumita Fujita, *Agronomy* **8** (2018) 31 (https://doi.org/10.3390/agronomy8030031)
25. K. Drzewiecka, A. Piechalak, P. Goliński, M. Gąsecka, Z. Magdziak, M. Szostek, S. Budzyńska, P. Niedzielski, M. Mleczek, *Chemosphere* **229** (2019) 589 (https://doi.org/10.1016/j.chemosphere.2019.05.051)
26. I .Van Dyck, N. Vanhoudt, J. Vives i Batlle, N. Horemans, A. Van Gompel, R. Nauts, J. Wannijn, A. Wijgaerts, A. Vassilev, J. Vangronsveld, *Environ. Exp. Bot.* **213** (2023) 105440 (https://doi.org/10.1016/j.envexpbot.2023.105440)
27. R. Kashyap, R. Bajaj, S. Sajen, A. Raj, A. V. Jose, *Poll. Res.* **35** (2016) 403
28. R. Guderian, K. H. Becker, W. Fricke, R. Guderian, J. L. Löbeö, R. Rabe, U. Schurath, D. T. Tingey, *Air Pollution by Photochemical Oxidants: Formation, Transport, Control, and Effects on Plants*, Springer Science and Business Media, Berlin, 2012 (ISBN 3642701183)
29. T. Šoštarić, Z. Lopičić, D. Ranđelović, T. Rakić, A. Antanasković, I. Mikavica, J. Milojković, in *Proceeding of 17th International Conference on Fundamental and Applied*

Aspects of Physical Chemistry, 2024, Belgrade, 2024, p. 459 (https://doi.org/10.46793/Phys.Chem24II.459S)
30. I. Mikavica, T. Šoštarić, A. Antanasković, D. Ranđelović, J. Petrović, G. Jovanović, Z. Lopičić, in *Proceeding of VII International Congress "Engineering, Environment and Materials in Process Industry"*, 2021, Jahorina, 2021, p. 268
31. P. Y. Deng, W. Liu, B. Q. Zeng, Y. K. Qiu, L. S. Li, *Int. J. Environ. Sci. Tech*. **10** (2013) 559 (https://doi.org/10.1007/s13762-013-0186-3)
32. W. Azuma, S. Nakashima, E. Yamakita, H. R. Ishii, K. Kuroda, *Tree Physiol.* **37** (2017) 1367 (https://doi.org/10.1093/treephys/tpx085)
33. J. Ord, H. J. Butler, M. R. McAinsh, F. L. Martin, *Analyst* **141** (2016) 2896 (https://doi.org/10.1039/C6AN00392C)
34. K. Hasan, Y. Cheng, M. K. Kanwar, X. Y. Chu, G. J. Ahammed, Z. Y. Qi, *Front. Plant. Sci.* **8** (2017) 1492 (https://doi.org/10.3389/fpls.2017.01492)
35. S. Qaiser, A. R. Saleemi, M. Umar, *J. Hazard. Mater.* **166** (2009) 998 (https://doi.org/10.1016/j.jhazmat.2008.12.003)
36. M. R. Sangi, A. Shahmoradi, J. Zolgharnein, G. H. Azimi, M. Ghorbandoost, *J. Hazard. Mater.* **155** (2008) 513 (https://doi.org/10.1016/j.jhazmat.2007.11.110)
37. I. Langmuir, *J. Am. Chem. Soc.* **40** (1918) 1361 (https://doi.org/10.1021/ja02242a004)
38. H. M. F. Freundlich, *J. Phys. Chem.* **57** (1906) 385 (https://doi.org/10.1515/zpch-1907-5723)
39. R. Sips, *J. Chem. Phys.* **16** (1948) 490 (https://doi.org/10.1063/1.1746922)
40. S. Chowdhury, P. D. Saha, *Colloids Surfaces, B* **88** (2011) 697 (https://doi.org/10.1016/j.colsurfb.2011.08.003)
41. V. J. Inglezakis, S. G. Poulopoulos H. Kazemian, *Micropor. Mesopor. Mat.* **272** (2018) 166 (https://doi.org/10.1016/j.micromeso.2018.06.026)
42. P. S. Kumar, R. Gayathri, *J. Eng. Sci. Technol.* **4** (2009) 381 (https://jestec.taylors.edu.my/Vol%204%20Issue%204%20December%2009/Vol_4_4_381_399_P.%20Senthil%20Kumar.pdf)
43. H. Darla, P. Garimella, *Environ. Prog. Sustain. Energy* **38** (2019) S118 (https://doi.org/10.1002/ep.12945)
44. S. Qaiser, A. R. Saleemi, M. Umar, *J. Hazard. Mater.* **166** (2009) 998 (https://doi.org/10.1016/j.jhazmat.2008.12.003)
45. H. Chen, J. Zhao, G. Dai, J. Wu, H. Yan, *Desalination* **262** (2010) 174 (https://doi.org/10.1016/j.desal.2010.06.006)
46. U. M. K. Nagpal, A. V. Bankar, N. J. Pawar, B. P. Kapadnis, S. S. Zinjarde, *Water Air Soil Pollut*. **215** (2011) 177 (https://doi.org/10.1007/s11270-010-0468-z)
47. S. Chakravarty, A. Mohanty, T. Nag Sudha, A. K. Upadhyay, J. Konar, J. K. Sircar, A. Madhukar, K. K. Gupta, *J. Hazard. Mater.* **173** (2010) 502 (https://doi.org/10.1016/j.jhazmat.2009.08.113)
48. L. B. L. Lim, N. Priyantha, Y. Lu, N. A. H. M. Zaidi, *Desalin. Water Treat.* **166** (2019) 44 (https://doi.org/10.5004/dwt.2019.24620).

Journal of the Serbian Chemical Society
JSCS@tmf.bg.ac.rs • www.shd.org.rs/JSCS
J. Serb. Chem. Soc. 91 (4) S135–S142 (2026) *Supplementary material*

SUPPLEMENTARY MATERIAL TO

Comparative assessment of adsorbents performances of plant biomasses grown on different sites: Case study of invasive *Acer negundo* L.

TATJANA ŠOŠTARIĆ[1]*, ZORICA LOPIČIĆ[1], DRAGANA RANĐELOVIĆ[1], TAMARA RAKIĆ[2], ANJA ANTANASKOVIĆ[1], IVANA MIKAVICA[1] and SNEŽANA ZILDŽOVIĆ[1]

[1]*Institute for Technology of Nuclear and Other Mineral Raw Materials, Boulevard Franchet d'Esperey 86, 11000 Belgrade, Serbia and* [2]*University of Belgrade, Faculty of Biology, Studentski trg 16, 11000 Belgrade, Serbia*

J. Serb. Chem. Soc. 91 (4) (2026) 425–439

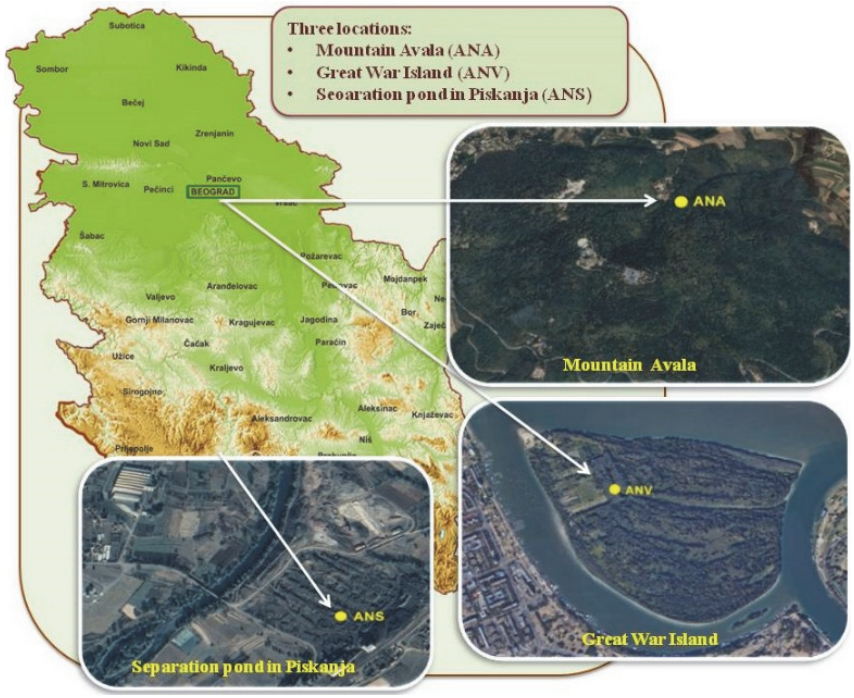

Fig. S-1. Sample points: forest edges on Mt. Avala (a), riparian forests at Great War Island (b) and banks of former coal separation pond in Piskanja (c).

* Corresponding author. E-mail: t.sostaric@itnms.ac.rs

Table S-I. Models used for evaluation of lead sorption onto investigated *A. negundo* sorbents

Model	Equation	Parameter
Kinetic model		
Pseudo-first order[1]	$\ln(q_e - q_t) = \ln q_e - k_1 t$	q_e (mg/g): sorption capacity at equilibrium q_t (mg/g): sorption capacity at any time t k_1 (g/mg/min): the pseudo first order rate constant
Pseudo-second order[2]	$q_t = \frac{t}{\left(\frac{1}{k_2 q_e^2}\right) + \left(\frac{t}{q_e}\right)}$	q_e (mg/g): sorption capacity at equilibrium q_t (mg/g): sorption capacity at any time t k_2 (g/mg/min): the pseudo second order rate constant
Elovich[3]	$q_t = \frac{1}{b}\ln(ab) + \frac{1}{b} lnt$	a(mg/g/min): initial Cu(II) sorption rate b (g/mg): extent of surface coverage
Isotherm model		
Langmuir[4]	$q_e = \frac{q_m K_L C_e}{1 + K_L C_e}$	q_m (mg/g): maximum sorption capacity K_L(dm^3/mg): Langmuir constant
Freundlich[5]	$q_e = K_f \ C_e^{1/n}$	K_f (mg/g) (L/g)$^{1/n}$: Freundlich constant n: heterogeneity factor
Sips[6]	$q_e = \frac{q_m K_S C_e^s}{1 + C_e {K_S}^s}$	K_s (dm^3/g): Sips constant related to sorption affinity s: heterogeneity factor

TABLE S-II. Soil pH, SOC, oxido-reduction potential (Eh) and pseudo-total content of PTE, and content of macroelements from the topsoil layer, together with mean values of PTE content in leaves of ANA, ANV and ANS. Statistically significant differences are marked with asterisk ($p<0.05$ = *, $p<0.01$ = **, $P<0.001$=***)

Ele. (ppm)	ANA_S	ANV_S	ANS_S		ANA_L	ANV_L	ANS_L	
Cu	58.0 ± 0.1	31.9 ± 0.1	46.9 ± 1.0	***	19.9 ± 0.4	18.5 ± 0.5	15.7 ± 0.2	***
Fe	26,294 ± 182	28,994 ± 2044	41,817 ± 570	***	265 ± 32	222 ± 30	200 ± 13.7	
Ni	64.8 ± 5.0	63.2 ± 2.9	116 ± 6	***	34.9 ± 0.0	34.9 ± 0.2	44.9 ± 0.0	***
Mn	31.1 ± 0.1	34.2 ± 2.3	152 ± 7	***	45.9 ± 6.5	48.4 ± 0.0	12.2 ± 0.2	***
Cd	1.74 ± 0.24	1.5 ± 0.5	2.49 ± 0.00	**	n.d.	n.d.	1.24±0.25	***
Pb	82.2 ± 2.2	39.9 ± 5.1	65.0 ± 4.8	***	n.d.	n.d.	n.d	
Zn	234 ± 7	85.1 ± 6.9	95 ± 1	***	46.9 ± 1.4	48.8 ± 3.5	43.1 ± 2.7	
Ca	80,919 ± 991	11,354 ± 20	6,175 ± 59	***	51,413 ± 1,028	39,914 ± 473	26,430 ± 503	***
Na	226 ± 1	225 ± 16	406 ± 2	***	91.4 ± 18.3	88.8 ± 6	87.7 ± 19.9	
K	4,563 ± 132	5,514 ± 28	3,649 ± 4	***	14,334 ± 107	15,300 ± 276	17,417 ± 1,586	
Mg	16,308 ± 372	6,986 ± 487	6,038 ± 202		4,690 ± 540	4,415 ± 22	3,329 ± 38	***
pH	6.85 - 7.15	5.90 - 6.27	4.64 - 4.76					
Eh (mV)	271.0	212.2	370.2					
SOC (%)	4.0	3.4	2.6					

S – soil; L - leaf

TABLE S-III. BCF_L (soil to leaf) of PTE in ANA, ANV and ANS

Elements	**ANA**	**ANV**	**ANS**
Cu	0.34 ± 0.01	0.58 ± 0.01	0.34 ± 0.01
Fe	0.01 ± 0.001	0.01 ± 0.001	0.005 ± 0.0003
Ni	0.54 ± 0.04	0.55 ± 0.03	0.39 ± 0.02
Mn	1.48 ± 0.22	1.42 ± 0.09	0.08 ± 0.01
Cd	N/A	N/A	0.50 ± 0.10
Zn	0.20 ± 0.0004	0.58 ± 0.09	0.46 ± 0.03

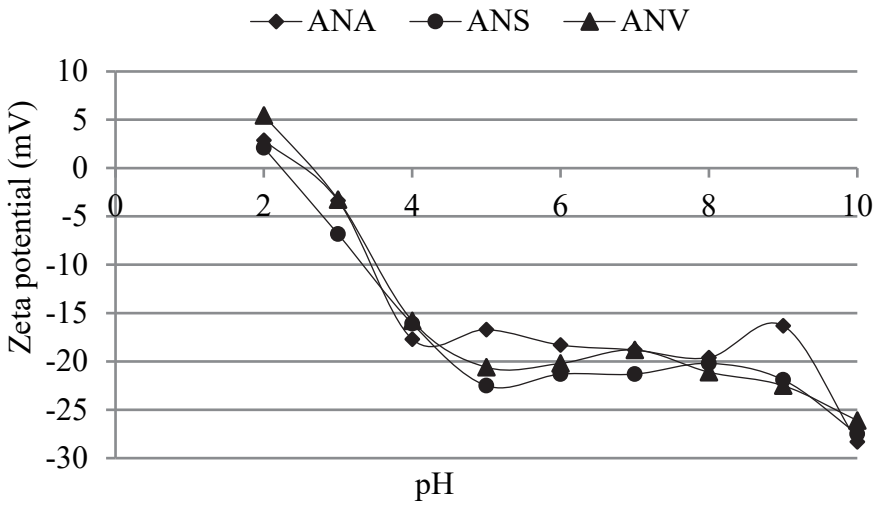

Fig. S-2. The zeta potential values of ANA, ANS and ANV under various pH values range

TABLE S-IV. Release of K^+, Mg^{2+}, Na^+, Ca^{2+} and H^+ due to biosorption of Pb^{2+}

Total metal bound	Net amount of cation released (meq/g)								
	Pb^{2+}	K^+	Na^+	Mg^{2+}	Ca^{2+}	H^+	$R_{b/r}$	pHi	pHf
ANA	43.45	5.0	0.4	12.2	23.0	5.0	0.95	5.0	3.91
ANV	45.56	8.2	0.3	8.9	18.7	6.3	1.07	5.0	3.86
ANS	45.07	15.5	0.25	9.8	33.7	8.0	0.67	5.0	3.77

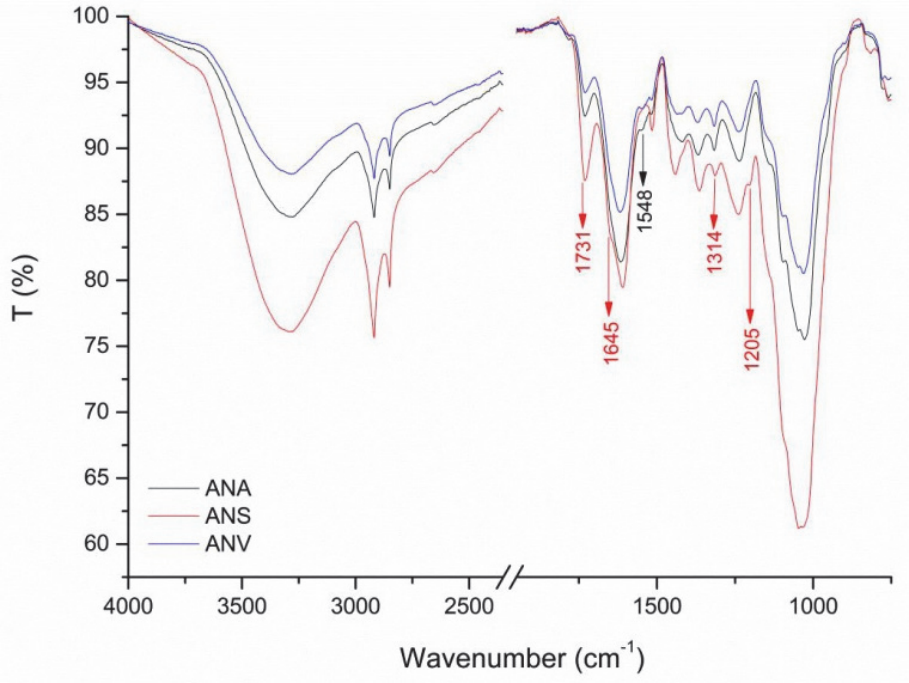

Fig. S-3. ATR-FTIR spectra of all samples

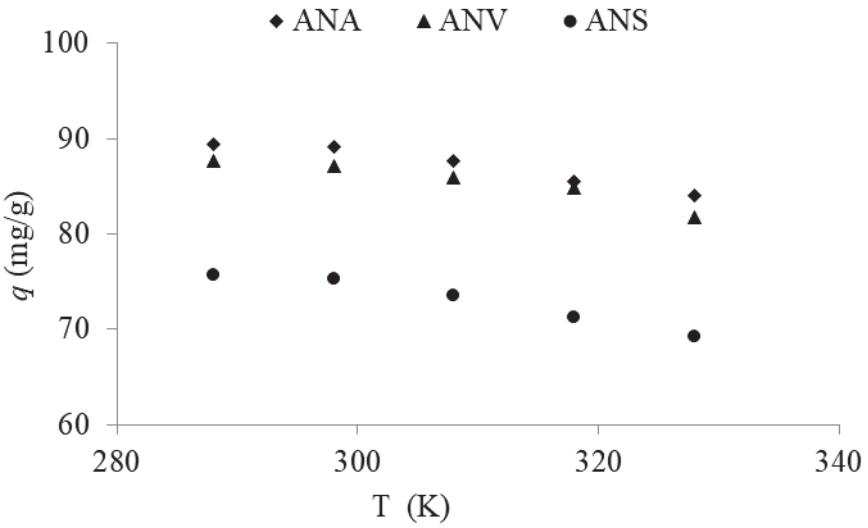

Fig. S-4. Effect of temperature on lead sorption capacity

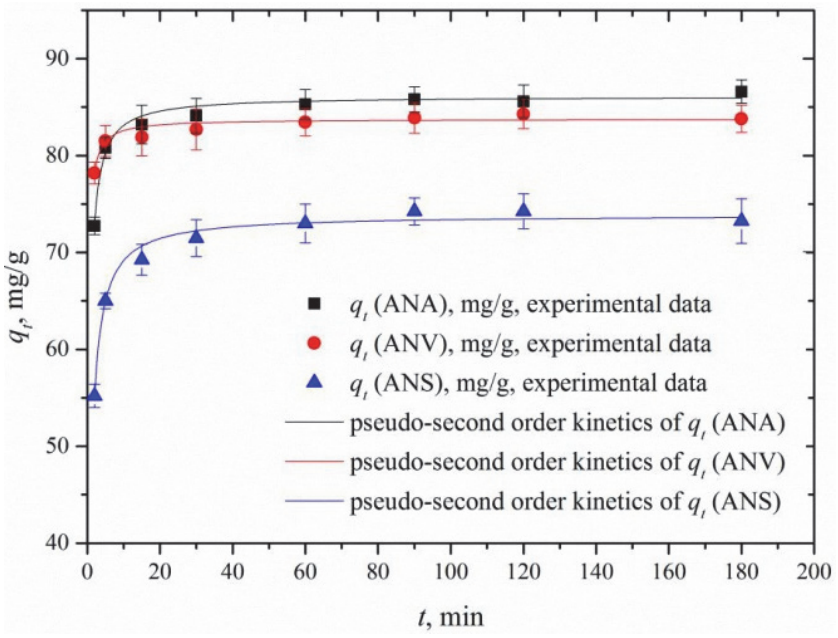

Fig. S-5. Sorption kinetics: sorbed amount of lead per mass of sorbents (q_t) as a function of time: experimental data (symbols) and the best fit predictions of the pseudo second order kinetics

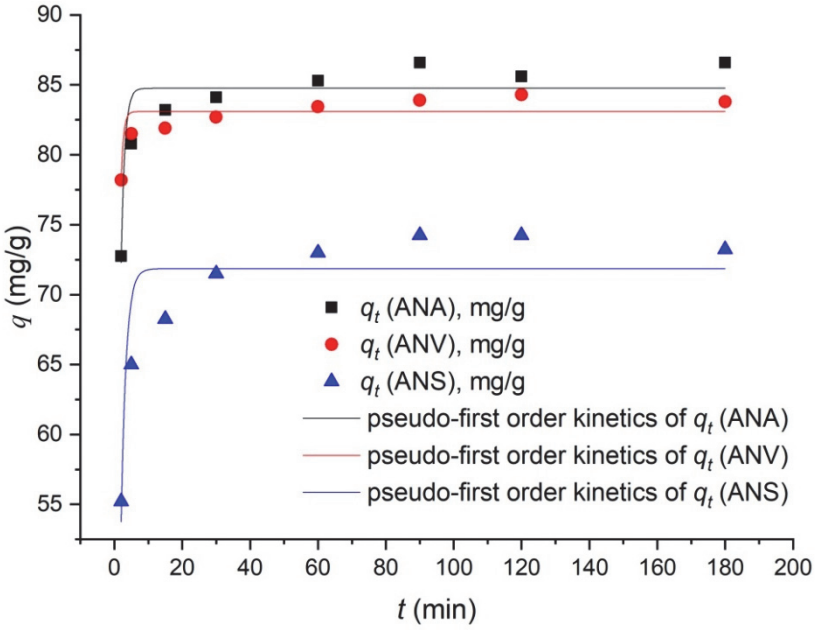

Fig. S-6. Sorption kinetics: the pseudo first order kinetics

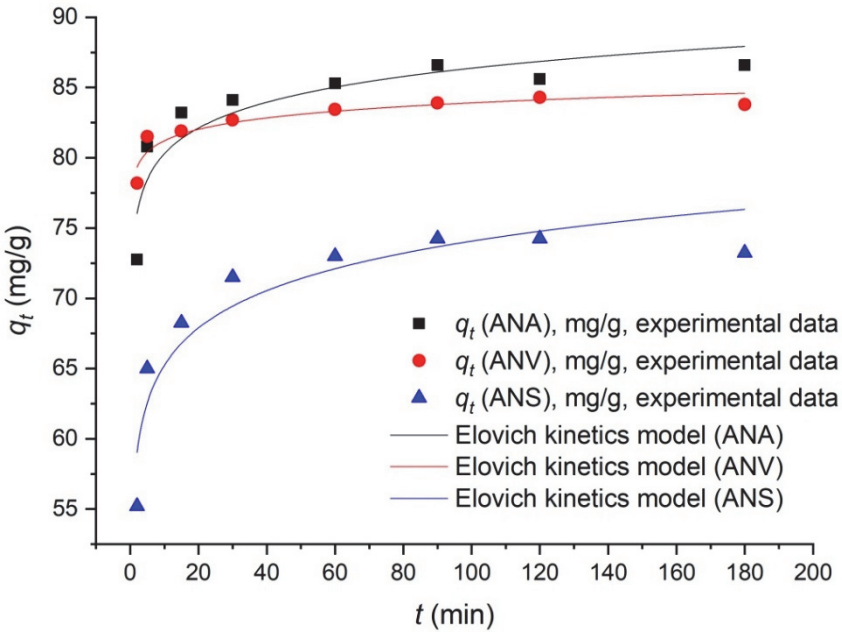

Fig. S-7. Sorption kinetics: the Elovich model

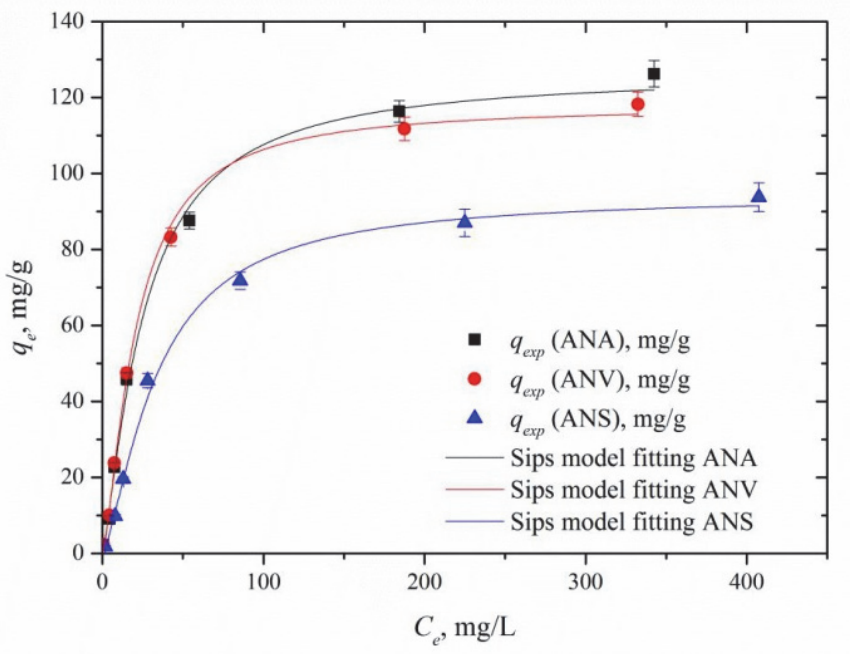

Fig. S-8. Experimental isotherm data and nonlinear Sips model fit of lead sorption onto ANA, ANV and ANS

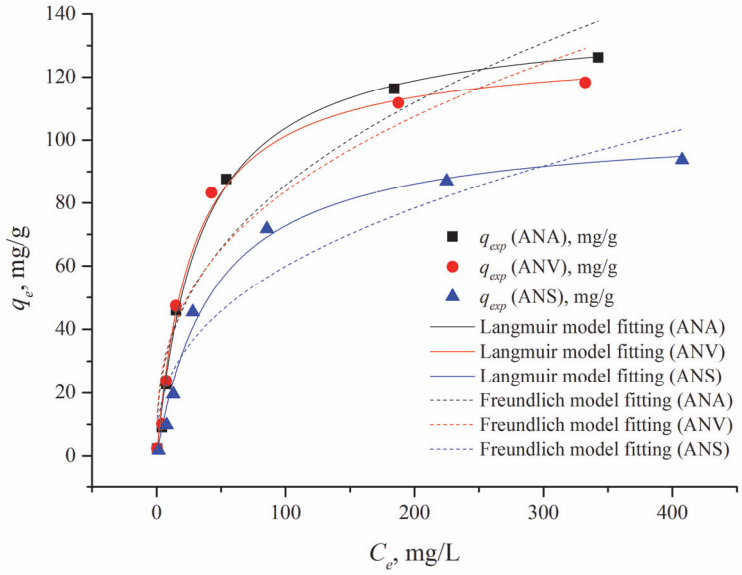

Fig. S-9**.** Experimental isotherm data and nonlinear Langmuir and Freundlich model fit of Pb(II) sorption onto ANA, ANV and ANS.

REFERENCES

1. S. Lagergren, *K. Sven. Veternskapsakad Handl.* **24** (1898) 1-39
2. Y. S. Ho, G. McKay, *Process Biochem.* **34** (1999) 451-465 (https://doi.org/10.1016/S0032-9592(98)00112-5)
3. M. J. D. Low, *Chem. Rev.* **60** (1960) 267-312 (https://doi.org/10.1021/cr60205a003)
4. I. Langmuir, *J. Am. Chem. Soc.* **40** (1918) 1361-1403 (https://doi.org/10.1021/ja02242a004)
5. H. M. F. Freundlich, *Zeitschrift für Physikalische Chemie* **57** (1907) 385-470 (https://doi.org/10.1515/zpch-1907-5723)
6. R. Sips, *J. Chem. Phys.* **16** (1948) 490-495 (https://doi.org/10.1063/1.1746922).